Determining Pavement Design Criteria for Recycled Aggregate Base and Large Stone Subbase

MnDOT Project TPF-5(341)

Task 4 – Laboratory Testing

October 2019

Prepared by:
Bora Cetin – Principal Investigator
Haluk Sinan Coban – Graduate Research Assistant

Reviewed by:
William J. Likos – Co-Principal Investigator
Tuncer B. Edil – Co-Principal Investigator
Askin Ozocak – Visiting Scholar

TABLE OF CONTENTS

LIST OF TABLES

LIST OF FIGURES

1. INTRODUCTION

About 1.33 billion tons of virgin aggregates (VAs) were produced in the U.S. in 2017, with approximately 76% used for pavement construction (Ober 2018). The price of VAs has increased due to increasing demand, loss of natural sources, and federal/local restrictions regarding their production (ACPA 2010). Reduced availability and cost-effectiveness of VAs has directed researchers' and contractors' attention to alternative materials (Westover et al. 2007). The use of recycled aggregates to construct recycled aggregate base (RAB) layers is a promising approach since such layers can perform similarly to VA base layers or even better. Several positive environmental consequences, such as reduced consumption of natural sources, improved waste utilization, and decreased greenhouse gas emissions and energy consumption can be achieved by using recycled aggregates (Lee et al. 2010). The use of recycled aggregates can also provide overall project savings by minimizing transportation costs for VAs (Gonzalez and Moo-Young 2004). Recycled concrete aggregate (RCA) and recycled asphalt pavement (RAP) are the two recycled aggregates that have been used in aggregate base layer construction. RCA materials are produced by crushing and processing hardened concrete recovered from rigid pavements or other structures (Edil et al. 2012; LRRB 2016). An RCA material consists of virgin aggregate and residual mortar. Residual mortar is the mortar that remains attached to the virgin aggregates after crushing and processing the existing hardened concrete. RAP materials are produced by milling and processing asphalt layers of old or failed flexible pavements (Edil 2011).

For improving pavement sustainability, the use of other alternative materials such as unconventionally large aggregates (i.e. large stones) is also gaining popularity. In general, conventional size aggregates are used to construct subbase layers. However, in recent years, the use of large stones for subbase layer construction has increased [subbase layers constructed with large stones are called large stone subbase (LSSB) layers hereinafter]. Large stones can perform equally as or even better than conventional size aggregates; therefore, they could be alternatives to conventional size aggregates (Kazmee et al. 2016). The amount of energy, which is used to break up rocks or stones to obtain conventional size aggregates, can be reduced with the direct use of large stones for LSSB layer construction (Kazmee et al. 2015). Decreased greenhouse gas emission and improved pavement sustainability can also be achieved with the use of large stones (Lee et al. 2010). The use of large stones for LSSB layer or working platform construction has been investigated by several departments of transportation (DOTs). These agencies include Illinois DOT and Wisconsin DOT (Tanyu et al. 2004; Kazmee et al. 2015, 2016). Crushed rock, breaker run, pit run, and rock cap materials were used as large stones for base and LSSB layer construction (Tanyu et al. 2004; Schuettpelz et al. 2010; Kazmee et al. 2015, 2016). Most of the fundamental laboratory tests cannot be conducted on large stones due to the limitations of the size of the existing test apparatus, e.g., sieve analysis may not be practical for testing large stones due to the size limitations of the existing test apparatus.

Material characteristics such as gradation, sphericity, angularity, texture, and durability are different for each VA or recycled aggregate, and these differences affect the engineering properties of aggregates significantly (Tutumluer 2013; Tan et al. 2014). The original structure from which the RCA material is produced or the gradation may affect the unhydrated cement content of the RCA material. The amount of unhydrated cement affects the engineering properties and the long-term performance of RAB layers constructed with RCA materials (Hiller et al. 2011). The stiffness

of RAB layers constructed with RAP materials is affected by the original aggregate type, asphalt content, and the gradation of RAP materials (Thakur and Han 2015). Metallic objects, crushed clay bricks, or pavement markings, which may be present in RCA and RAP materials, may affect the engineering properties of such materials. The amount of such deleterious materials is not constant and is affected by the original aggregate source and the crushing methods (Jayakody et al. 2012). Some specifications (AASHTO 2002; Greenbook 2009; ASTM 2016) restrict the content of the deleterious materials to 5% for aggregate base layer construction unless it is proven that the presence of the deleterious materials improves the engineering properties of the aggregate base layer (Edil et al. 2012). Some agencies generate RCA and RAP materials only from their own sources to minimize the presence of deleterious materials (West 2010, as cited in Hoppe et al. 2015). For others, who obtain the recycled aggregates from various sources, it is important to understand the components and the engineering properties of such aggregates for constructing high-quality and long-lasting pavements (Gonzalez and Moo-Young 2004).

A survey regarding the use of recycled aggregates in aggregate base layer construction was conducted by Minnesota DOT (MnDOT) in 2016 and the target participants were local transportation agencies (66 respondents) (LRRB 2016). Initially, it was concluded that about 11% of the respondents indicated that they had not used recycled aggregates due to lack of specification and guidance, lack of experience, and low amount of available recycled aggregates. Along with that, the rest of the respondents (about 89%) stated that they hesitated to use recycled aggregates for the first time because of some uncertainties of these materials related to gradation, durability, performance, and quality control. This survey demonstrates the importance of understanding the index and engineering properties of recycled aggregates.

In this task, a series of laboratory tests were performed to better understand the characteristics of recycled aggregates that were used to construct the test cells located on the Minnesota Road Research Project (MnROAD) Low Volume Road (LVR) test facility. Detailed information is provided regarding the test methods and data analyses. Test results are evaluated and summarized. After the detailed literature review and construction monitoring and reporting, this task is the fourth stage of a series of subsequent tasks which will include in-depth long-term performance analyses of the test cells constructed with RAB and LSSB layers.

2. TEST CELLS AND MATERIALS

2.1. Test Cells

The test cells were located on the Minnesota Road Research Project (MnROAD) Low Volume Road (LVR), a pavement test facility owned by the MnDOT (MnDOT 2017). The MnROAD LVR is a two-lane closed-loop located near westbound I-94, northwest of the Twin Cities, MN. Eleven test cells were constructed in three groups: (1) RAB group, (2) LSSB group, and (3) LSSB with geosynthetics group. The compositions of the test cells are provided in Figure 2.1.

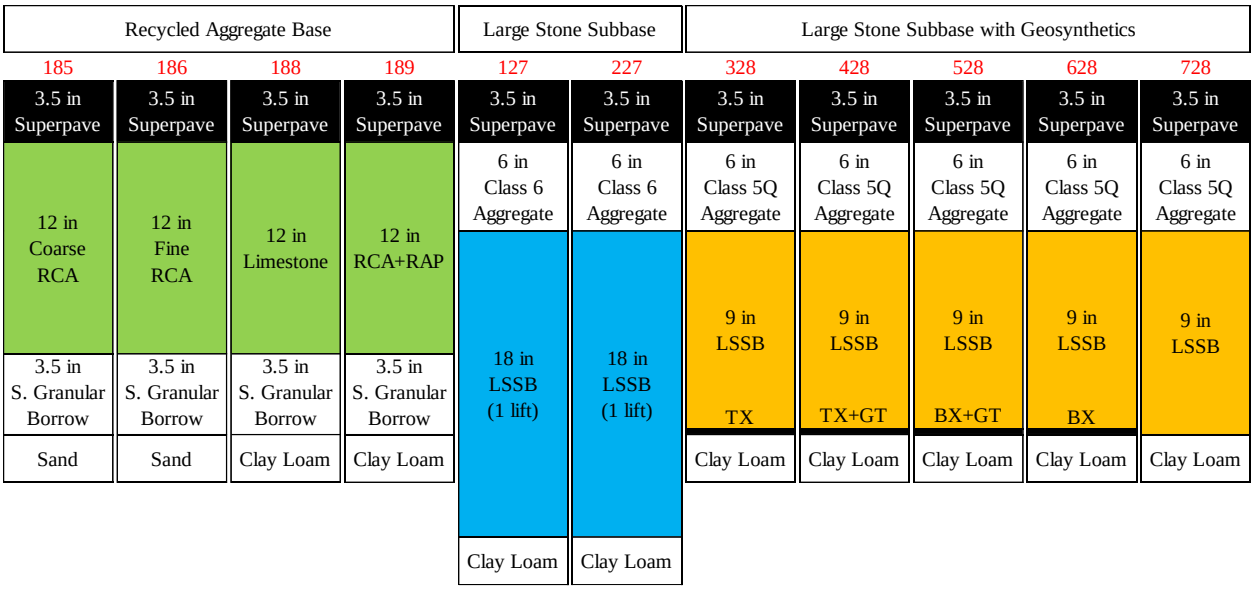

Figure 2.1. Compositions of the test cells (not to scale) (s. granular borrow = Select Granular Borrow, TX = triaxial geogrid, GT = geosynthetic, BX = biaxial geogrid)

2.2. Materials

Ten different materials (Figure 2.2) were used to construct the test cells (Figure 2.1). Two different subgrade soils were Sand Subgrade and Clay Loam [Figures 2.2(a) and 2.2(b), respectively]. Two different subbase materials were Select Granular Borrow (MnDOT 2018) and LSSB material (large crushed granite) [Figures 2.2(c) and 2.2(d), respectively]. Base layer aggregates were Coarse RCA, Fine RCA, Limestone, RCA+RAP, Class 6 Aggregate, and Class 5Q Aggregate (MnDOT 2018) [Figures 2.2(e), 2.2 (f), 2.2 (g), 2.2 (h), 2.2 (i), and 2.2 (j), respectively].

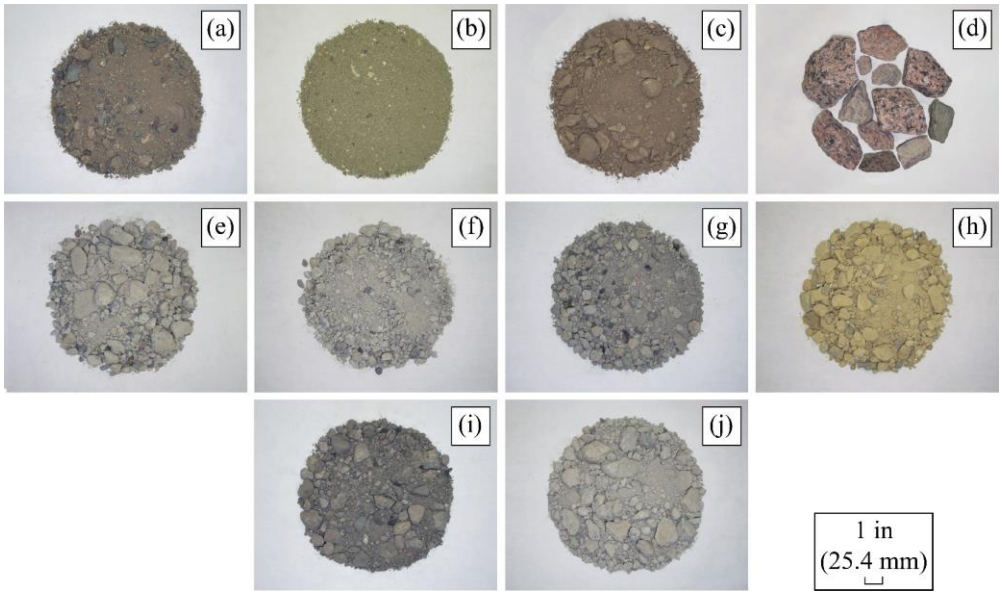

Figure 2.2. Materials used to construct the test cells: (a) Sand Subgrade, (b) Clay Loam, (c) Select Granular Borrow, (d) LSSB material, (e) Coarse RCA, (f) Fine RCA, (g) RCA+RAP, (h) Limestone, (i) Class 6 Aggregate, and (j) Class 5Q Aggregate

3. INDEX PROPERTIES

3.1. Deleterious Material Content

Each material was spread on a large pan and deleterious materials were identified visually. The deleterious materials that could be identified were plant roots, leaves, wood chips, plastic, and fabric. A magnet was used to remove metal, such as reinforcing steel, from the RCA materials' matrix. However, no steel pieces were observed. The collected deleterious materials were weighed. For each material, the weight of the deleterious materials was less than %0.1 of the dry weight of the material. Therefore, it was concluded that the materials satisfied the quality requirements determined by the MnDOT specification (MnDOT 2018). In addition, it was observed that the materials, other than RCA+RAP, also contained low amounts of RAP particles. However, those RAP particles were considered to be a part of those materials; therefore, they were not removed.

3.2. Classification of the Materials

Particle size distributions of the materials were determined in accordance with ASTM C136, D6913, and D7928 (Figure 3.1). Atterberg limits were determined per BS 1377-2 (fall cone penetrometer) and ASTM D4318 (plastic limit rolling device) (Table 3.1). Classifications were determined according to the Unified Soil Classification System (USCS) (ASTM D2487) and the American Association of State Highway and Transportation Officials (AASHTO) soil classification system (AASHTO M 145) (Table 3.1).

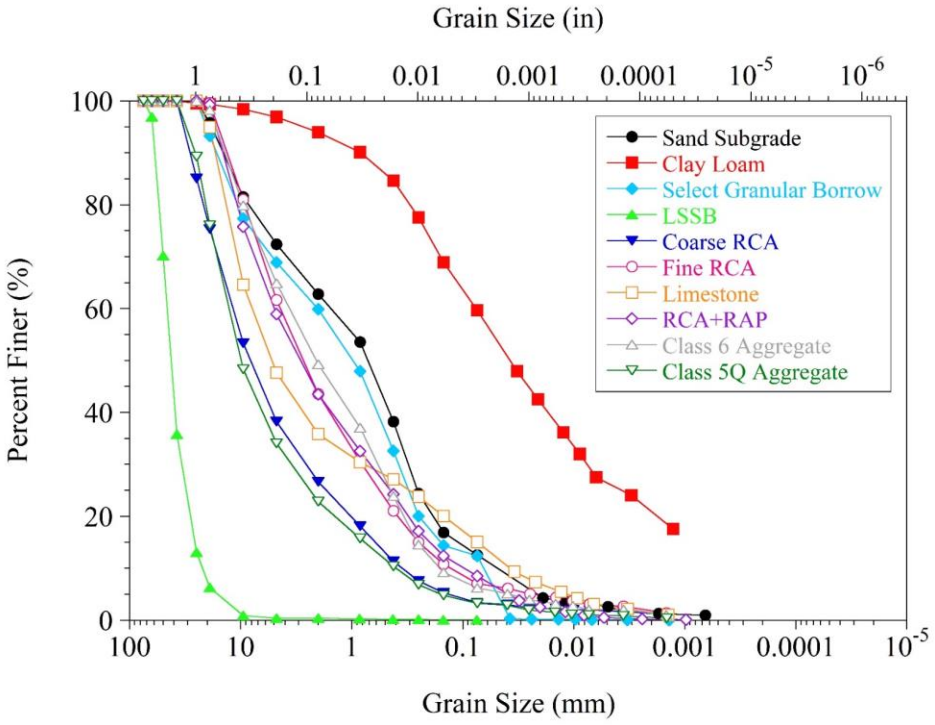

Figure 3.1. Particle size distributions of the materials

Sand Subgrade and Clay Loam were classified as SM (silty sand with gravel) and CL (sandy lean clay) according to the USCS, respectively. The AASHTO soil classifications were determined to

be A-1-b and A-6 for Sand Subgrade and Clay Loam, respectively. Select Granular Borrow and LSSB material were classified as SM (silty sand with gravel) and GP (poorly graded gravel) according to the USCS, respectively. The AASHTO soil classifications were determined to be A-1-b and A-1-a for Select Granular Borrow and LSSB material, respectively.

Coarse RCA, Fine RCA, Limestone, RCA+RAP, Class 6 Aggregate, and Class 5Q Aggregate were classified as GW (well-graded gravel with sand), SW-SM (well-graded sand with silt and gravel), GM (silty gravel with sand), SP-SM (poorly graded sand with silt and gravel), SP-SM (poorly-graded sand with silt and gravel), and GW (well-graded gravel with sand) according to the USCS, respectively. All base layer materials except Limestone were classified as A-1-a according to the AASHTO soil classification system. The AASHTO soil classification of Limestone was determined to be A-1-b.

Table 3.1. Index properties of the materials

Material	Gravel (%)	Sand (%)	Fines (%)	C_u	C_c	LL	PI	USCS	AASHTO
Sand Subgrade	27.6	59.8	12.6	33.12	1.24	19.9	NP	SM	A-1-b
Clay Loam	3.1	37.2	59.7	NA	NA	36.3	12.4	CL	A-6
Select Granular Borrow	31.1	56.5	12.4	30.30	1.10	18.9	NP	SM	A-1-b
LSSB	99.6	0.3	0.1	1.84	1.08	NA	NP	GP	A-1-a
Coarse RCA	61.7	34.9	3.4	34.49	1.75	NA	NP	GW	A-1-a
Fine RCA	38.3	54.6	7.1	33.93	1.12	32.7	NP	SW-SM	A-1-a
Limestone	52.3	32.6	15.1	211.3	1.91	17.9	NP	GM	A-1-b
RCA+RAP	41	50.4	8.6	49.41	0.98	27.4	NP	SP-SM	A-1-a
Class 6 Aggregate	35.1	58.6	6.3	23.82	0.60	27.4	NP	SP-SM	A-1-a
Class 5Q Aggregate	65.9	30.9	3.2	33.69	2.60	NA	NP	GW	A-1-a

Fines = silt and clay; C_u = uniformity coefficient; C_c = coefficient of curvature; LL = liquid limit; PI = plasticity index; USCS = Unified Soil Classification System; AASHTO = American Association of State Highway and Transportation Officials; NP = non-plastic; NA = not available.

3.3. Specific Gravity (G_s) and Absorption

Specific gravity (G_s) and absorption of all the materials except Clay Loam were determined based on ASTM C127 and C128. For Clay Loam, ASTM D854 was followed. G_s and absorption of each material (except Clay Loam) were determined by taking the weighted average of the coarse [> No. 4 sieve (4.75 mm)] and fine (< No. 4) fractions of the material (Table 3.2). Three different specific gravity terms are provided in Table 3.2: (1) oven-dry, (2) saturated-surface-dry, and (3) apparent G_s. However, only the oven-dry G_s, which is the most commonly used in Geotechnical Engineering, is discussed hereinafter.

Sand Subgrade and Clay Loam exhibited G_s values of 2.60 and 2.68, respectively. Sand Subgrade exhibited an absorption of 1.84%. Absorption could not be determined for Clay Loam because ASTM D854 does not include any testing procedure to determine absorption for clayey soils. G_s and absorption of Select Granular Borrow were determined to be 2.62 and 1.53%, respectively. LSSB material exhibited a G_s value of 2.60 and an absorption value of 0.36%.

Coarse RCA, Fine RCA, and RCA+RAP exhibited lower G_s (2.25, 2.17, and 2.28, respectively) and higher absorption (6.97, 8.65, and 4.34%, respectively) than Limestone (G_s and absorption were 2.66 and 1.72%, respectively). RCA materials tend to show lower G_s and higher absorption than VAs because of their residual mortar content and porous structure (Snyder et al. 1994; Abbas et al. 2007; Bhasya and Bharatkumar 2018). Low-density asphalt binder and trapped air between the asphalt and aggregate particles cause lower G_s for RAP (Cosentino et al. 2003; Okafor 2010). Fine RCA exhibited lower G_s (2.17) and higher absorption (8.65%) than Coarse RCA (G_s and absorption were 2.25 and 6.97%, respectively). RCA+RAP exhibited lower absorption (4.34%) than Coarse RCA (6.97%) and Fine RCA (8.65%) and this was attributed to RAP material's hydrophobicity (Rahardjo et al. 2010; Nokkaew et al. 2012).

Class 6 Aggregate and Class 5Q Aggregate also exhibited lower G_s (2.35 and 2.28, respectively) and higher absorption (3.86% and 6.32%, respectively) than Limestone (G_s and absorption were 2.66 and 1.72%, respectively). Based on these results and the visual-manual soil identification procedure (ASTM D2488), it was determined that Class 6 Aggregate and Class 5Q Aggregate contained considerable amounts of RCA. In addition, Class 6 Aggregate also contained RAP.

Table 3.2. G_s and absorption of the materials

Material	Oven-Dry G_s	Saturated-Surface-Dry G_s	Apparent G_s	Absorption (%)
Sand Subgrade	2.60	2.64	2.72	1.84
Clay Loam	2.68	NA	NA	NA
Select Granular Borrow	2.62	2.66	2.72	1.53
LSSB	2.60	2.61	2.63	0.36
Coarse RCA	2.25	2.40	2.64	6.97
Fine RCA	2.17	2.35	2.64	8.65
Limestone	2.66	2.71	2.79	1.72
RCA+RAP	2.28	2.38	2.52	4.34
Class 6 Aggregate	2.35	2.44	2.58	3.86
Class 5Q Aggregate	2.28	2.42	2.65	6.32

G_s = specific gravity; NA = not available.

3.4. Proctor Compaction

Maximum dry density (MDD) and optimum moisture content (OMC) values of the materials were determined per ASTM D1557. Method C was used for all the materials except Clay Loam and LSSB material. Method A was used for Clay Loam. Proctor compaction test could not be performed on LSSB material due to the size limitations of the compaction testing equipment.

Corrections for the materials containing oversize particles were applied per ASTM D4718. Figure 3.2 shows the compaction curves determined by the Proctor compaction test. Both Proctor compaction test results (ASTM D1557) and corrected unit weight and moisture content values (ASTM D4718) are summarized in Table 3.3. Only the corrected unit weight and moisture content values will be discussed hereinafter.

Sand Subgrade exhibited relatively higher MDD (137.7 pcf) and lower OMC (5.6%) compared to Clay Loam (MDD and OMC were 124.9 pcf and 10%, respectively) (Table 3.3). MDD and OMC of Select Granular Borrow were determined to be 140.3 pcf and 5.3%, respectively.

Coarse RCA, Fine RCA, and RCA+RAP exhibited lower MDD (128.6, 121.7, and 125.8 pcf, respectively) and higher OMC (9.5, 11.1, and 10%, respectively) than Limestone (MDD and OMC were 143.2 pcf and 6.3%, respectively). RCA materials are prone to exhibit higher OMC compared to VAs because of their higher absorption and hydrophilicity (Rahardjo et al. 2010). RCA materials also tend to exhibit lower MDD than VAs because of the presence of residual mortar, which lowers G_s. Cementation of unhydrated cement particles in the RCA matrix increases the resistance of particles against compaction efforts, and this can also reduce MDD (Hussain and Dash 2010, Chen and Brown 2012). Fine RCA exhibited lower MDD (121.7 pcf) and higher OMC (11.1%) than Coarse RCA (MDD and OMC were 128.6 pcf and 9.5%, respectively) and RCA+RAP (MDD and OMC were 125.8 pcf and 10%, respectively).

Class 6 Aggregate and Class 5Q Aggregate exhibited lower MDD (128.5 and 128 pcf, respectively) and higher OMC (8.3 and 9.6%, respectively) than Limestone (MDD and OMC were 143.2 pcf and 6.3%).

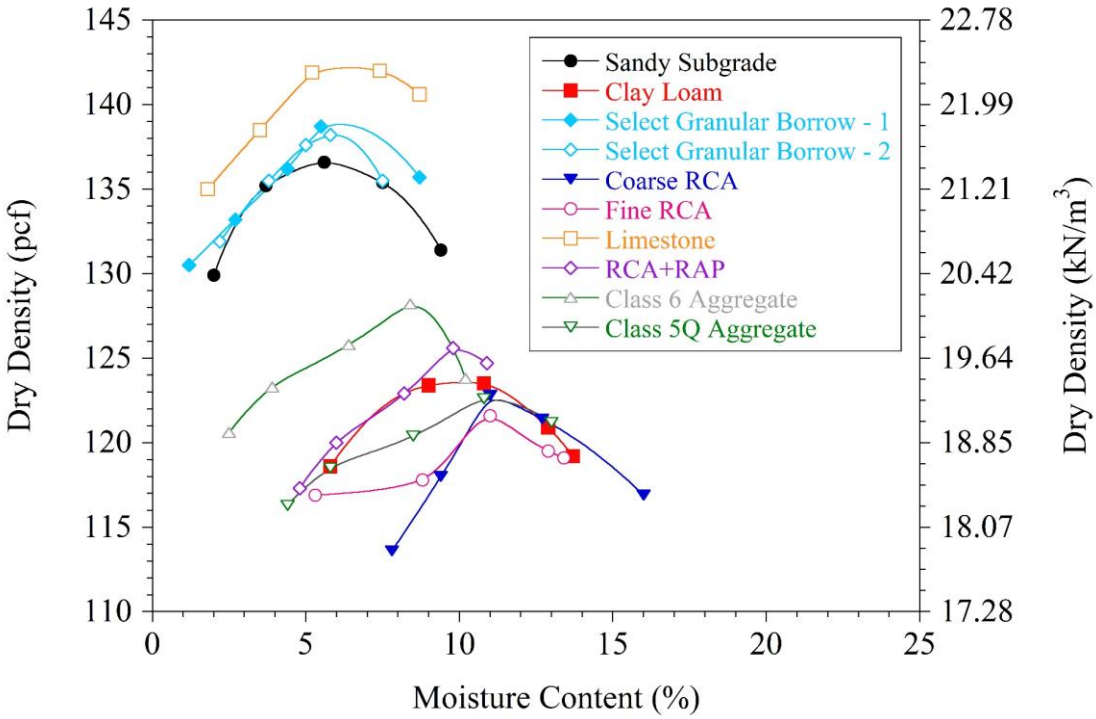

Figure 3.2. Proctor compaction curves of the materials

Table 3.3. Uncorrected (actual) and corrected Proctor compaction test results

Material	Proctor Compaction Test Results			Corrected for Oversize Particles		
	MDD		OMC (%)	Corrected MDD		Corrected OMC (%)
	(pcf)	(kN/m^3)		(pcf)	(kN/m^3)	
Sand Subgrade	136.6	21.46	5.7	137.7	21.63	5.6
Clay Loam	123.9	19.46	10	124.9	19.62	10.0
Select Granular Borrow	138.6	21.77	5.4	140.3	22.03	5.3
LSSB	NA	NA	NA	NA	NA	NA
Coarse RCA	122.9	19.31	11.3	128.6	20.19	9.5
Fine RCA	121.6	19.10	11.1	121.7	19.12	11.1
Limestone	142.2	22.34	6.2	143.2	22.49	6.3
RCA+RAP	125.6	19.73	10	125.8	19.76	10.0
Class 6 Aggregate	128.2	20.14	8.3	128.5	20.19	8.3
Class 5Q Aggregate	122.6	19.26	11	128.0	20.11	9.6

MDD = maximum dry density; OMC = optimum moisture content; NA = not available.

3.5. Asphalt Binder Content

In order to find the asphalt binder contents of the materials used, the ignition method (AASHTO T 308 and ASTM D6307) and the quantitative extraction method (AASHTO T 164 and ASTM D2172) were performed [Figures 3.3(a) and 3.3(b), respectively].

Figure 3.3. (a) Ignition furnace used in the ignition method and (b) asphalt extraction bowl used in the quantitative extraction

Overall, asphalt binder contents, determined by the ignition method, were relatively higher than the binder contents, determined by the quantitative extraction method (Table 3.4). Mineral fines and other organic materials may be burned away from the test material during ignition and cause higher asphalt binder contents. In addition, loss of fines, which are lighter than the granular particles, by the ventilation system during ignition may be another reason for observed higher asphalt binder contents by the ignition method.

For both methods, RCA+RAP and Class 6 Aggregate exhibited the highest asphalt binder contents. Asphalt binder content of RCA+RAP was determined to be 3.18 and 1.58% by the ignition method and the quantitative extraction method, respectively. Asphalt binder content of Class 6 Aggregate was determined to be 3.17 and 1.77% by the ignition method and the quantitative extraction method, respectively. Asphalt binder contents of Coarse RCA, Fine RCA, Limestone, and Class 5Q Aggregate were not zero because they contained RAP in small quantities (Figure 3.4). According to the ignition method, asphalt binder content of Fine RCA (2.98%) was close to those of RCA+RAP (3.18%) and Class 6 Aggregate (3.17%). However, according to the quantitative extraction method, Fine RCA contained considerably lower asphalt binder (0.35%) compared to RCA+RAP (1.58%) and Class 6 Aggregate (1.77%). As stated previously, Fine RCA exhibited the lowest G_s (2.17) indicating that it consisted of lighter particles compared to other materials (Table 3.2). It was speculated that the presence of lighter fine particles in Fine RCA caused higher loss of fines by the ventilation system (lighter particles can be sucked by the ventilation system easier than heavier particles) for Fine RCA and this caused asphalt binder content (2.98%) for Fine RCA to be as high as asphalt binder content of RCA+RAP (3.18%) and Class 6 Aggregate (3.17%). According to the ignition method, Coarse RCA and Class 5Q Aggregate had relatively higher asphalt binder contents (2.02 and 2.15%, respectively) compared to Limestone (1.61%). However, according to the quantitative extraction, Coarse RCA and Class 5Q Aggregates had the lowest asphalt binder contents (0.10 and 0.28%, respectively). This result can also be attributed to lower G_s of Coarse RCA (2.25) and Class 5Q Aggregate (2.28) compared to Limestone (2.66).

Table 3.4. Asphalt binder contents of the materials by the two methods

Material	Asphalt Binder Content (%)	
	Ignition Method	Quantitative Extraction Method
Coarse RCA	2.02	0.10
Fine RCA	2.98	0.38
Limestone	1.61	0.35
RCA+RAP	3.18	1.58
Class 6 Aggregate	3.17	1.77
Class 5Q Aggregate	2.15	0.28

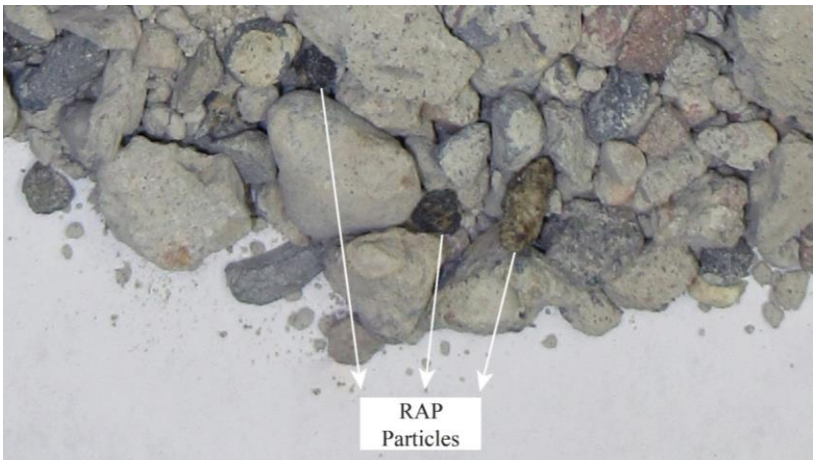

Figure 3.4. RAP particles in Coarse RCA as an example

3.6. Residual Mortar Content

Residual mortar contents of the materials used were determined based on a method developed by Abbas et al. (2008). A saturated sodium sulfate solution (26% by weight) was prepared as described in ASTM C88 (soundness test) (Figure 3.5). In fact, only a sodium sulfate concentration of 17% (by weight) would be enough for the saturated solution. However, according to ASTM C88, it is desirable that an excess of sodium sulfate crystals is to be present in the solution. Therefore, a more-than-needed amount of sodium sulfate (26% by weight) was used. Due to the high sodium sulfate concentration, salt cake formed in the solution (Figure 3.6). For each material, 2000 g of the particles retained on a 1-in sieve (if any), 2000 g of the particles retained on a 3/4-in sieve (if any), 1000 g of the particles retained on a 3/8-in sieve, and 1000 g of the particles retained on a No. 4 sieve were collected (Figure 3.7). The prepared samples were then dried for 24 h at 105°C. After drying, the oven-dried samples were immersed in the sodium sulfate solution for 24 h. While the samples were in the solution, they were subjected to five daily freeze-thaw cycles. Each freeze-thaw cycle included 16 h of freezing at -17°C (1.4°F) [Figure 3.8(a)] and 8 h of thawing at 80°C (176°F) [Figure 3.8(b)]. After the completion of the last cycle, the mixtures of the disintegrated mortar and natural aggregates (Figure 3.9) were washed over No. 4 (4.75 mm) sieve to get rid of the disintegrated mortar. As recommended by Butler et al. (2011), a rubber mallet was used to crush the remaining mortar and the samples were washed again over No. 4 sieve and dried at 105°C (221°F) for 24 h. Then, the final oven-dry mass of each sample was recorded, and the residual mortar content of each material was calculated. Upon visual inspection, 100% removal of the residual mortar could not be achieved as some aggregate particles still contained a thin mortar film on their surfaces (Figure 3.10). However, it was concluded that almost all the residual mortar was removed (Figure 3.11).

Class 5Q Aggregate and Coarse RCA contained the highest (37.1%) and the second highest (33.4%) residual mortar, respectively, compared to other base layer aggregates (Table 3.5). Fine RCA contained the third highest residual mortar (29.6%) (Table 3.5). Class 6 Aggregate exhibited relatively higher residual mortar content (25.6%) than RCA+RAP (20.1%) (Table 3.5). Limestone did not exhibit any considerable residual mortar content (1.3%), as expected (Table 3.5).

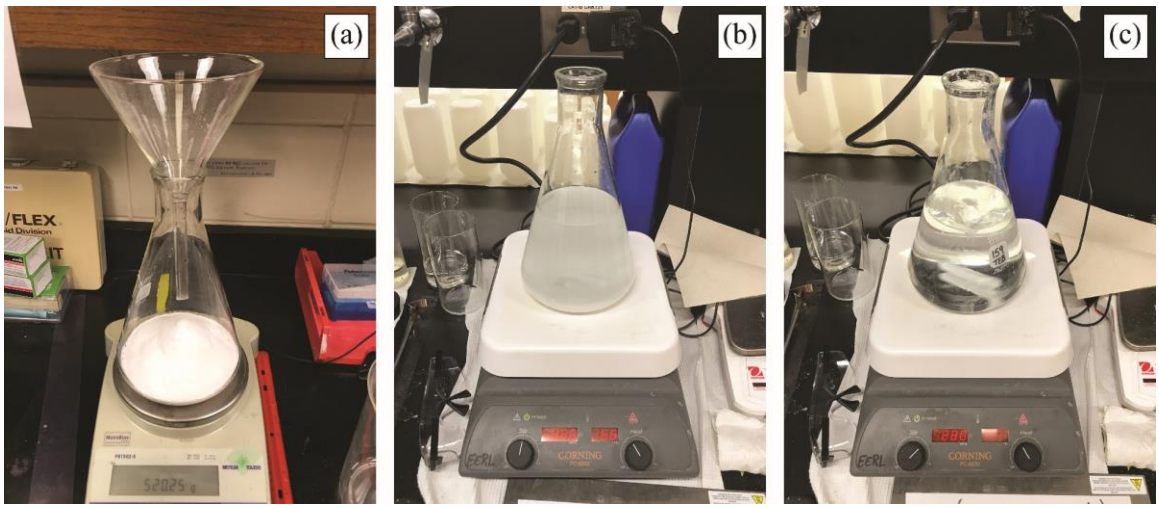

Figure 3.5. (a) Preparation of the sodium sulfate solution, (b) early stage of mixing, and (c) end of mixing

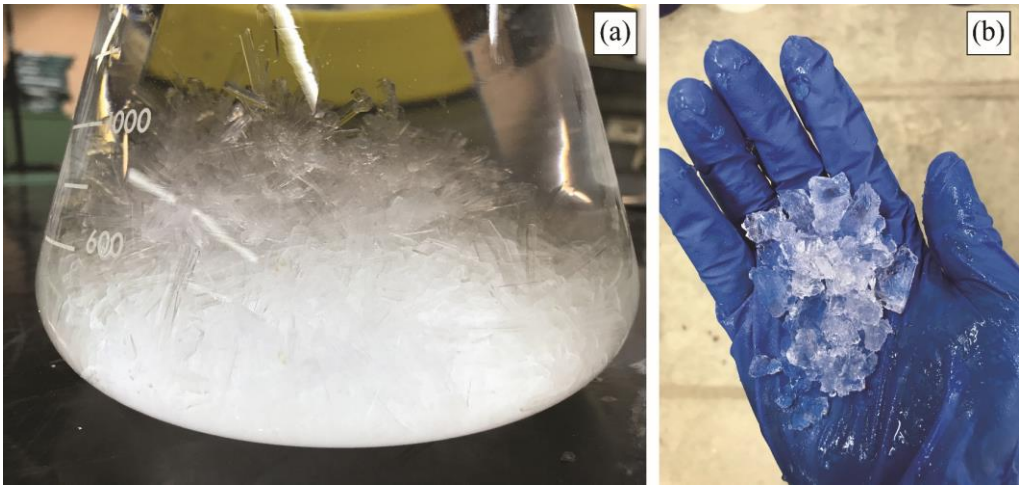

Figure 3.6. (a) Crystallization of sodium sulfate and (b) broken salt crystals

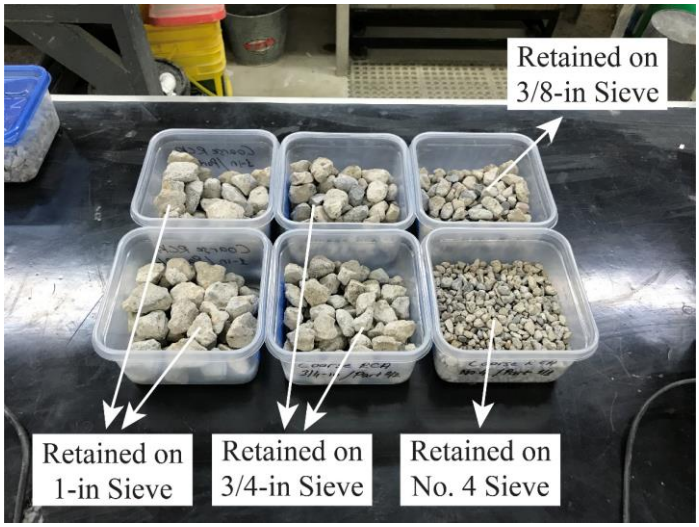

Figure 3.7. Samples prepared for Coarse RCA

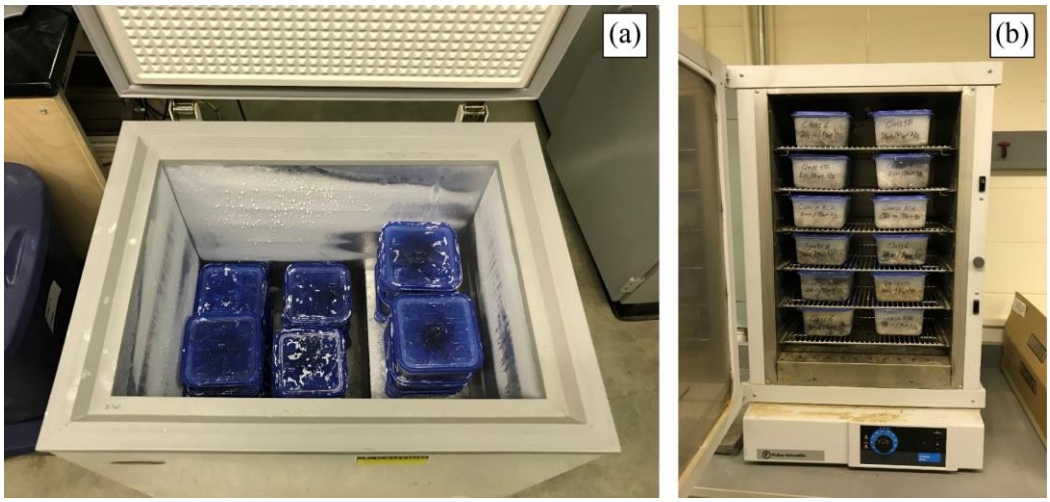

Figure 3.8. (a) Freezing phase and (b) thawing phase

Figure 3.9. Mixture of the disintegrated mortar and aggregates

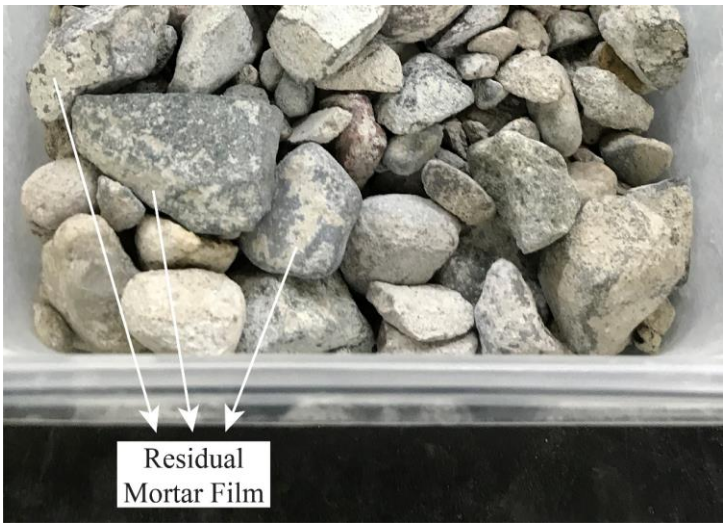

Figure 3.10. Remaining mortar film on the particle surfaces

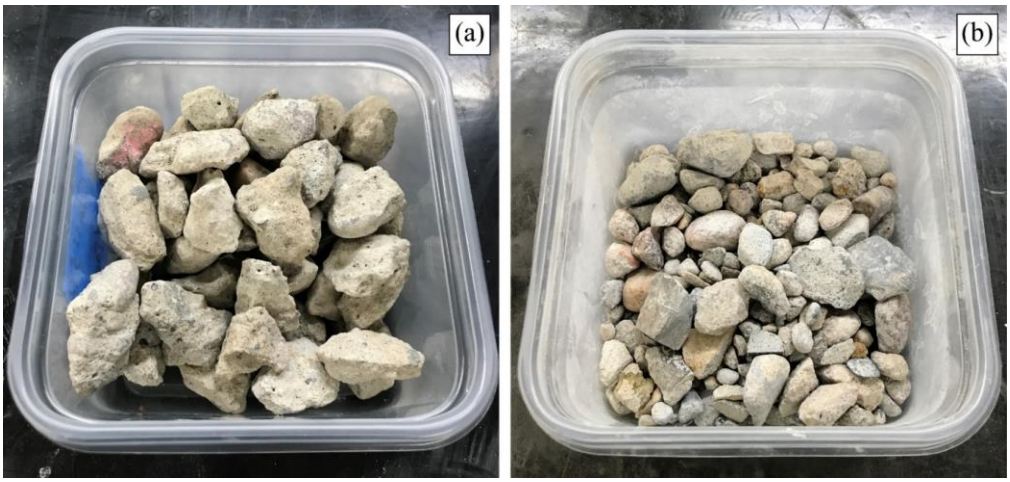

Figure 3.11. (a) Before the residual mortar content determination test and (b) after the test

Table 3.5. Residual mortar contents of the materials

Material	Residual Mortar Content (%)
Coarse RCA	33.4
Fine RCA	29.6
Limestone	1.3
RCA+RAP	20.1
Class 6 Aggregate	25.6
Class 5Q Aggregate	37.1

3.7. Water Repellency

Water repellency of base layer aggregates was evaluated by the apparent contact angle and the water drop penetration time (WDPT) measurements. The apparent contact angle (the angle at zero energy state of water) is the angle between the tangent to the solid surface and the tangent to the liquid-fluid interface (Figure 3.12) (Wolansky and Marmus 1999). The WDPT is defined as the time required for a water drop to completely infiltrates through the materials after its placement at the surface of the aggregate particle (Edil et al. 2012). Mandal and Jayaprakash (2009) classify materials in terms of their water repellency based on their apparent contact angle and WDPT (Table 3.6).

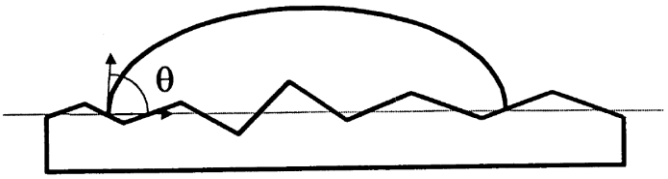

Figure 3.12. Apparent contact angle

Table 3.6. Water repellency classifications provided by Mandal and Jayaprakash (2009)

Water repellency	WDPT (s)	Apparent contact angle (°)
Wettable	<5	0
Slightly to moderately repellent	5–60	67
Strongly water-repellent	60–600	90
Severely water-repellent	600–3600	98
Extremely water-repellent	>3600	122

For Coarse RCA, Fine RCA, and Class 5Q Aggregate, 25 RCA particles were tested for each material. For RCA+RAP and Class 6 Aggregate, 25 RAP and 25 RCA particles were tested for each material. For Limestone, 25 particles were tested. Three examples for Coarse RCA, Fine RCA, Limestone, RCA+RAP, Class 6 Aggregate, and Class 5Q Aggregate are provided in Figures 3.13, 3.14, 3.15, 3.16, 3.17, and 3.18 respectively. The average apparent contact angle and WDPT

for each material are summarized in Table 3.7. Coarse RCA, Fine RCA, Limestone, and Class 5Q Aggregate exhibited 0° apparent contact angle and WDPT less than 5 seconds. Therefore, these materials were classified as wettable or hydrophilic. Apparent contact angles of RCA+RAP and Class 6 Aggregate were 83° and 86°, respectively. In addition, the water drops did not infiltrate through RCA+RAP and Class 6 Aggregate even after 3600 seconds from the placement of the water drops. As a result, these materials were classified as water repellent or hydrophobic.

Figure 3.13. Apparent water contact angle for Coarse RCA

Figure 3.14. Apparent water contact angle for Fine RCA

Figure 3.15. Apparent water contact angle for Limestone

Figure 3.16. Apparent water contact angle for RCA+RAP

Figure 3.17. Apparent water contact angle for Class 6 Aggregate

Figure 3.18. Apparent water contact angle for Class 5Q Aggregate

Table 3.7. Water repellency of the materials

Material	Apparent Contact Angle (°)	Water Drop Penetration Time (WDPT) (s)	Water Repellency
Coarse RCA	~ 0	< 5	Wettable (Hydrophilic)
Fine RCA	~ 0	< 5	Wettable (Hydrophilic)
Limestone	~ 0	< 5	Wettable (Hydrophilic)
RCA+RAP	~ 83	> 3600	Water Repellent (Hydrophobic)
Class 6 Aggregate	~ 86	> 3600	Water Repellent (Hydrophobic)
Class 5Q Aggregate	~ 0	< 5	Wettable (Hydrophilic)

4. SATURATED AND UNSATURATED PROPERTIES

One of the main functions of aggregate base layers is to provide adequate drainage and prevent capillary action to increase the service life of pavements (Cedergren 1988). An increase in the pore water pressure in aggregate base layers causes a reduction in the stiffness of aggregate base layers (Edil et al. 2012).

K_{sat} is the ability of soil to let water flow in the presence of a hydraulic gradient. SWCC is used to describe the relationship between the volumetric water content and the matric suction of unsaturated soils. K_{sat} is used as a parameter for drainage design, and SWCC is used to determine and evaluate the modulus of aggregate base layers (Gupta et al. 2004; NCHRP 2004).

Saturated and unsaturated properties of aggregate base layers could be affected by the type of the recycled aggregate used (RCA or RAP). RCA materials are hydrophilic due to residual mortar content and unhydrated cement content emerging after the demolition of existing concrete (Rahardjo et al. 2010; Edil et al. 2012). The use of RCA materials could reduce the permeability of aggregate base layers due to further cementation of unhydrated cement particles. Another concern may arise with the use of RCA in aggregate base layers due to the tufaceous formation by leaching and precipitation of heavy metals (Ceylan et al. 2013; Abbaspour et al. 2016). First, CO_2 in the atmosphere and H_2O in the aqueous solution of RCA react to form carbonic acid (H_2CO_3). Then, H^+ and CO_3 form after the two-step ionization of H_2CO_3. In the final step, Ca^{2+} released from the cement at the high pH environment reacts with CO_3 coming from the ionization of H_2CO_3 and the reaction forms calcite ($CaCO_3$) (Feldmann et al. 1982). Drainage properties of aggregate base layers constructed with RCA can be reduced as a result of the tufa formation (Ceylan et al.

2013). In addition, the pipes located beneath a pavement system for drainage purposes can be clogged by the tufa formation (Figure 4.1) (Ceylan et al. 2013).

The use of RAP materials could improve the drainage characteristics of aggregate base layers since RAP materials exhibit hydrophobic properties due to the asphalt coating around particles (Rahardjo et al. 2010; Edil et al. 2012).

Figure 4.1. Clean pipe (left) and partially clogged pipe (right) (Ceylan et al. 2013)

4.1. Permeability (K_{sat}) Test

K_{sat} tests were carried out on saturated specimens in accordance with ASTM D5084. For the tests, a permeability instrument with constant head principle (ASTM D5084 method A), which was suitable for coarser materials, was used. A sketch and a picture of the constant head permeability test equipment are provided in Figures 4.2 and 4.3, respectively. For the tests, 6-in diameter and 4-in height specimens were prepared inside of the membrane by light hammering method (Figure 4.4). For Coarse RCA, Fine RCA, Limestone, and RCA+RAP, three specimens were prepared per material. For Sand Subgrade, Class 6 Aggregate, and Class 5Q Aggregate, four specimens were prepared per material. After the completion of the specimen preparation, each specimen was saturated per ASTM D5084. Saturation was controlled by two methods. The first method was observing the color change throughout the membrane. Homogeneous color distribution within the membrane during the saturation process was the first indication of the saturation (this indication may not be 100% accurate since the inside of the specimen may not be saturated even if the homogeneous color distribution was achieved). The second method was observing the K_{sat} measurements over time. During the test, the volume of water passing through the test specimen under the constant hydraulic load was measured with time and K_{sat} values were calculated by Darcy's law, as described in ASTM D5084. In the early stages of the tests, K_{sat} values were not stable. However, after a certain time, K_{sat} values became stable and this was believed to be the actual indication of saturation (Figure 4.5). The K_{sat} value which reached the stability was recorded to be the K_{sat} of the specimen.

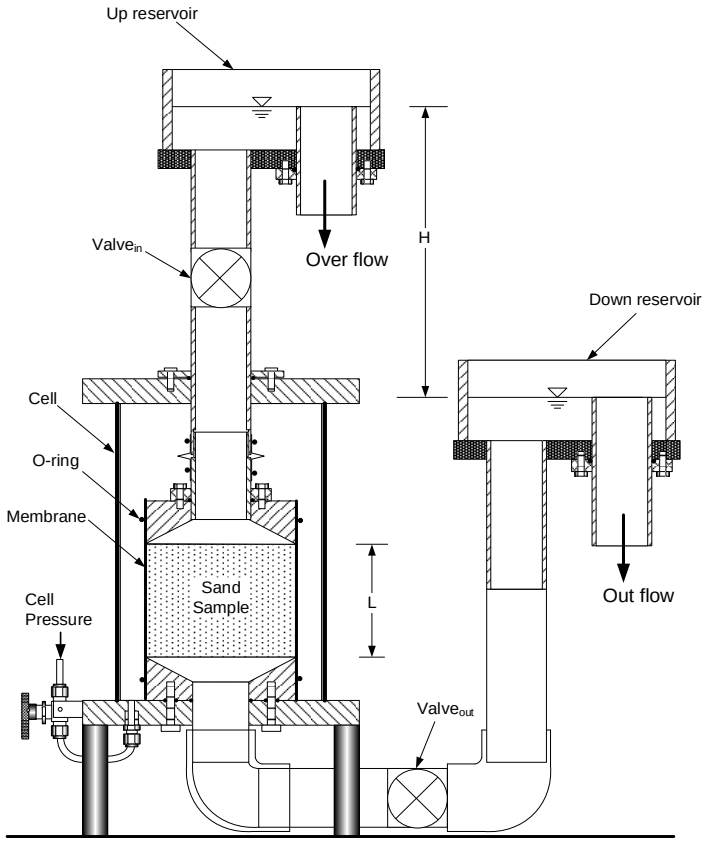

Figure 4.2. Sketch of the constant head permeability test equipment

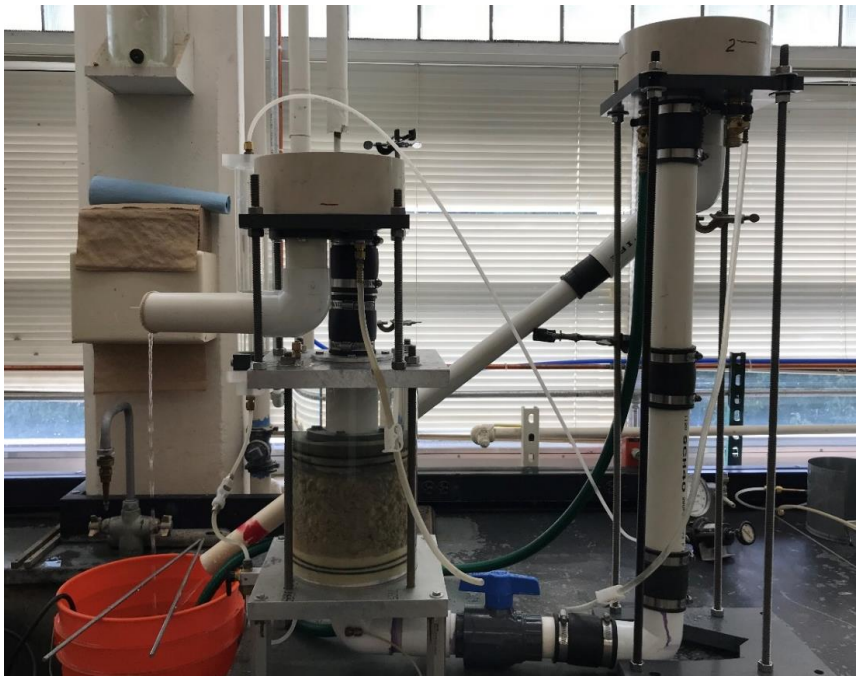

Figure 4.3. Picture of the constant head permeability test equipment

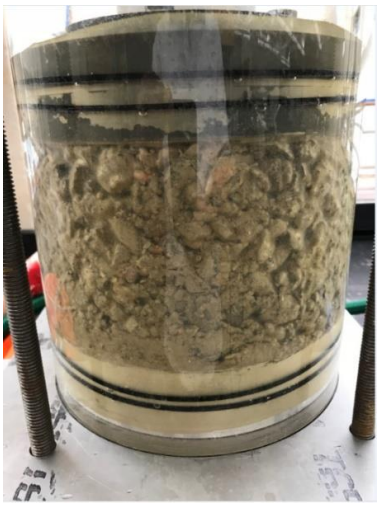

Figure 4.4. Specimen prepared for the constant head permeability test

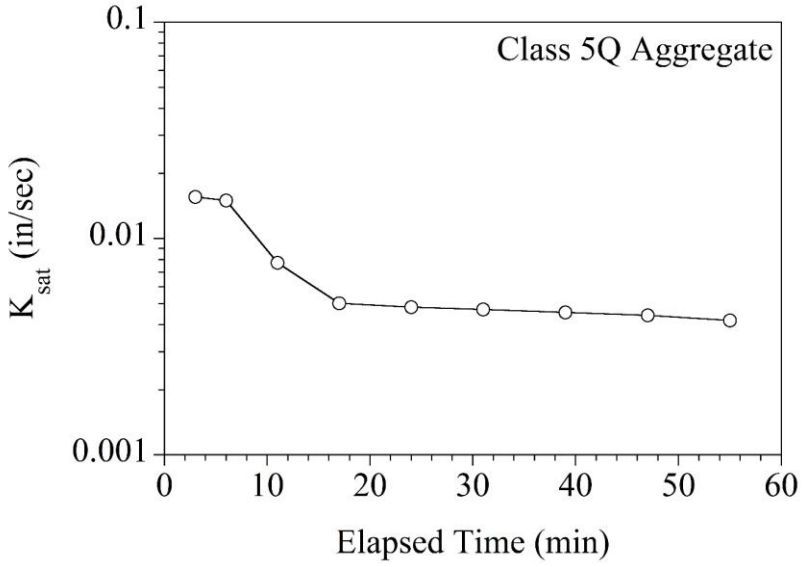

Figure 4.5. K_{sat} versus elapsed time during constant head permeability test

K_{sat} and the degree of compaction (DOC) values of the materials, determined by the constant head permeability tests, are provided in Figure 4.6. Overall, it was concluded that the specimens could not be compacted sufficiently by the light hammering in the membrane because the DOC values were lower than 100% (as low as 84.6%). Fine RCA yielded the highest K_{sat} values with a narrower range (ranging from $1.41x10^{-2}$ to $3.26x10^{-2}$ in/sec). Sand Subgrade, Coarse RCA, and RCA+RAP exhibited relatively lower K_{sat} values with wider ranges (ranging from $3.35x10^{-5}$ to $6.57x10^{-3}$ in/sec). Class 6 Aggregate and Class 5Q Aggregate also exhibited similar K_{sat} values (Class 6 Aggregate exhibited a narrower range) (ranging from $2.07x10^{-3}$ to $9.41x10^{-3}$ in/sec). Limestone exhibited similar K_{sat} values compared to Class 6 Aggregate and Class 5Q Aggregate; however, the minimum K_{sat} value of Limestone ($1.70x10^{-4}$ in/sec) was much lower than those of Class 6 Aggregate ($2.78x10^{-3}$ in/sec) and Class 5Q Aggregate ($2.07x10^{-3}$ in/sec).

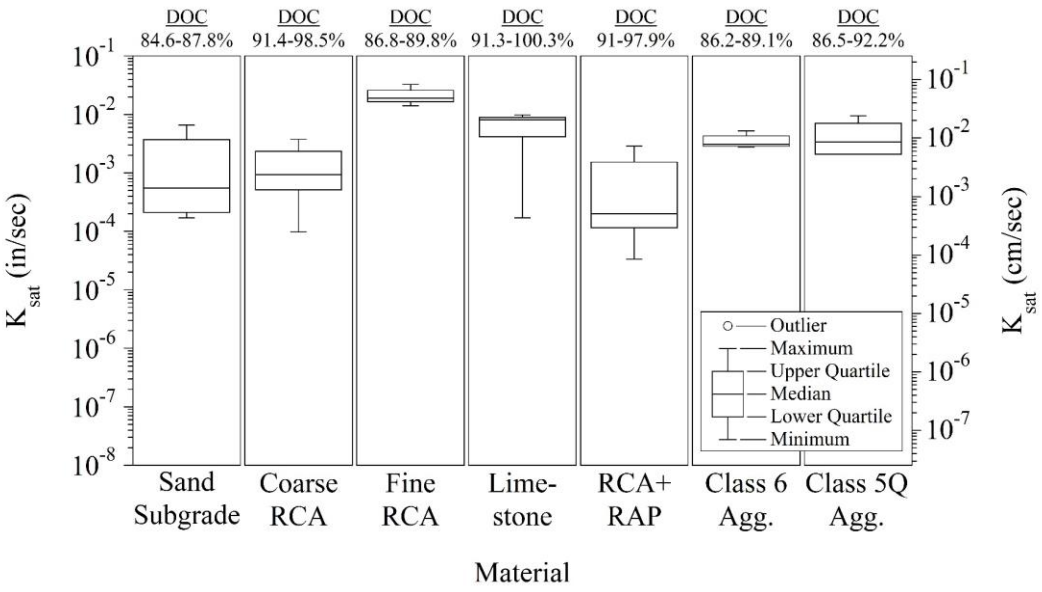

Figure 4.6. Constant head permeability test results (DOC = degree of compaction)

After evaluating the DOC values obtained by the light hammering in the membrane, a new specimen preparation method, in which the specimens were compacted in a 6-in compaction mold in five layers, was followed. First, all materials were sieved through a 3/4-in sieve and then the specimens were compacted to their MDD and OMC (Figure 3.2 and Table 3.3). After the compaction, the specimens were extruded from the compaction mold by a hydraulic jack (Figure 4.7) and placed into a membrane to be put into a triaxial cell. Clay Loam, Coarse RCA, Fine RCA, Limestone, and RCA+RAP specimens were prepared by this method for further testing. For Clay Loam, six specimens were prepared. For Coarse RCA, Fine RCA, Limestone, and RCA+RAP, three specimens were prepared per material.

The permeability test method was also switched to the standard falling head permeability tests (ASTM D5084 method C). The cell and the burette system of the falling head permeability test are provided in Figure 4.8.

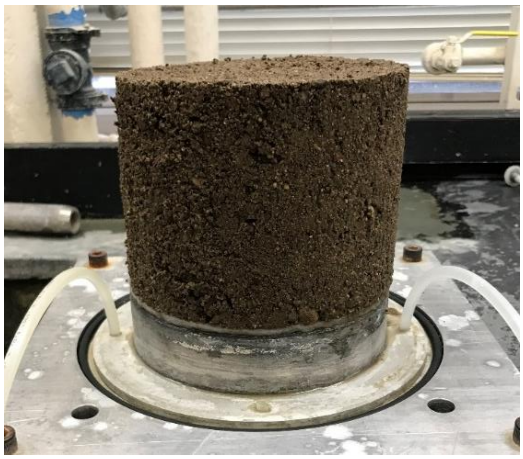

Figure 4.7. Specimen prepared in the compaction mold for the falling head permeability test

Figure 4.8. Picture of the falling head permeability test system

K_{sat} and the DOC values of the specimens, which were prepared in the compaction mold and tested by the falling head permeability test, are provided in Figure 4.9. Relatively higher DOC values were observed by using the compaction mold (the lowest DOC was 96.8%) instead of the membrane [the DOC values were as low as 84.6% (Figure 4.6)]. Overall, the K_{sat} values obtained by the falling head permeability (Figure 4.9) were in narrower ranges compared to those obtained by the constant head permeability (Figure 4.6). Clay Loam exhibited the lowest K_{sat} values as expected (ranging from $3.75x10^{-8}$ to $2.59x10^{-7}$ in/sec). Coarse RCA, Fine RCA, and RCA+RAP exhibited similar K_{sat} values (K_{sat} values of Fine RCA were in a narrower range) (ranging from $3.93x10^{-5}$ to $3.28x10^{-4}$ in/sec). Limestone yielded lower K_{sat} values (ranging from $1.34x10^{-5}$ to $1.93x10^{-5}$ in/sec) than Coarse RCA, Fine RCA, and RCA+RAP.

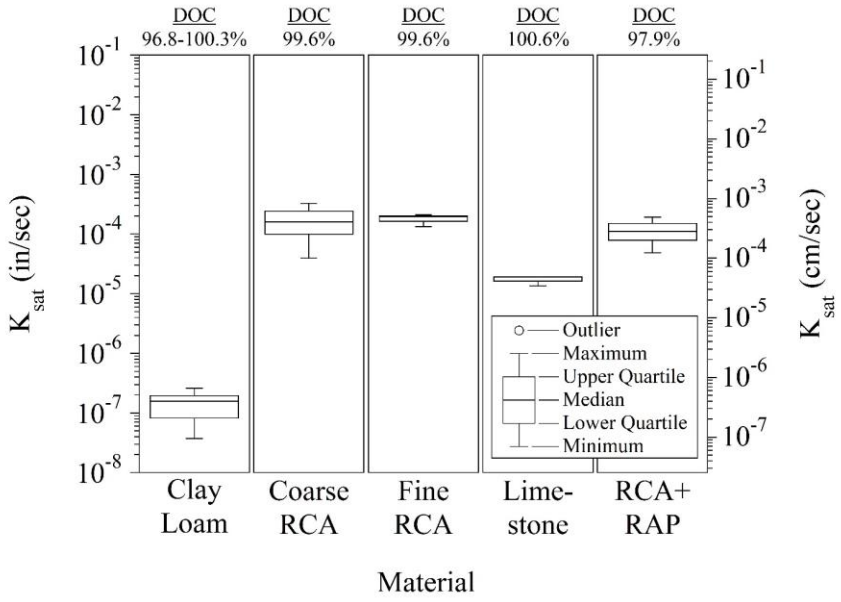

Figure 4.9. Falling head permeability test results (DOC = degree of compaction)

To observe the effects of the DOC on K_{sat} values of each material, more tests were prepared for all materials except Select Granular Borrow and LSSB material. All specimens were compacted in the compaction mold at three different compaction energies to obtain 100, 95, and 90% DOC (Table 3.3). Specimens were compacted at their corresponding OMCs (Table 3.3) and OMCs were kept constant. Then, falling head permeability tests were performed on each material and results were evaluated (Figure 4.10). Particle size distributions of the materials used in the tests are summarized in Figure 4.11 and Table 4.1.

Overall, lowering the DOC yielded higher K_{sat} values for all materials. Less compaction, yielding lower DOC values, was obtained by applying lower compaction energies and these materials exhibited a more porous structure which allowed water to pass through faster. For all three cases, Clay Loam yielded the lowest K_{sat} values ($5.39x10^{-8}$, $5.94x10^{-7}$, and $2.70x10^{-6}$ in/sec for 100, 95, and 90% DOC, respectively). Then, Limestone exhibited the second lowest K_{sat} values for all three cases ($3.17x10^{-5}$, $7.52x10^{-5}$, and $1.29x10^{-4}$ in/sec for 100, 95, and 90%, respectively). Coarse RCA exhibited the third lowest K_{sat} values for 100 and 90% DOC ($5x10^{-5}$ and $2.63x10^{-4}$ in/sec). For 95% DOC, Coarse RCA exhibited the fourth lowest K_{sat} value ($1.92x10^{-4}$ in/sec); however, it was very close to the K_{sat} value of RCA+RAP ($1.89x10^{-4}$ in/sec), which was the third lowest one. Fine RCA exhibited the highest K_{sat} values for 100 and 95% DOC ($1.88x10^{-4}$ and $3.90x10^{-4}$ in/sec, respectively). However, for 90% DOC, Fine RCA exhibited lower K_{sat} value ($3.98x10^{-4}$ in/sec) than Class 6 Aggregate ($6.18x10^{-4}$ in/sec), Class 5Q Aggregate ($6.14x10^{-4}$ in/sec), and RCA+RAP ($5.79x10^{-4}$ in/sec). Class 5Q Aggregate, Sand Subgrade, and Class 6 Aggregate exhibited the second, third, and fourth highest K_{sat} values for 100 and 95% DOC. Overall, it was concluded that the trends between the K_{sat} values of all materials were similar between 100 and 95% DOC. However, for 90% DOC, the trends changed for all materials except Clay Loam and Limestone.

Coarse RCA yielded lower K_{sat} values than Fine RCA at each DOC (Figure 4.10). This result could be attributed to the higher fines content of the representative sample taken from Coarse RCA. In fact, Coarse RCA contained fewer fines content (3.4%) than Fine RCA (7.1%). However, prior to tests, each material was sieved through the 3/4-in sieve for the preparation of the specimens and this caused a difference in the particle size distributions of the materials and test specimens. Since the amount of particles larger than the 3/4-in sieve in Coarse RCA (24.6%) was higher than that of Fine RCA (0.3%), removal of such particles during the specimen preparation caused a higher increase in Coarse RCA's fines content (from 3.4% to 12.4%) than Fine RCA's fines content (from 7.1% to 9.6%). Therefore, Coarse RCA had lower permeability than that of Fine RCA and other base layer materials.

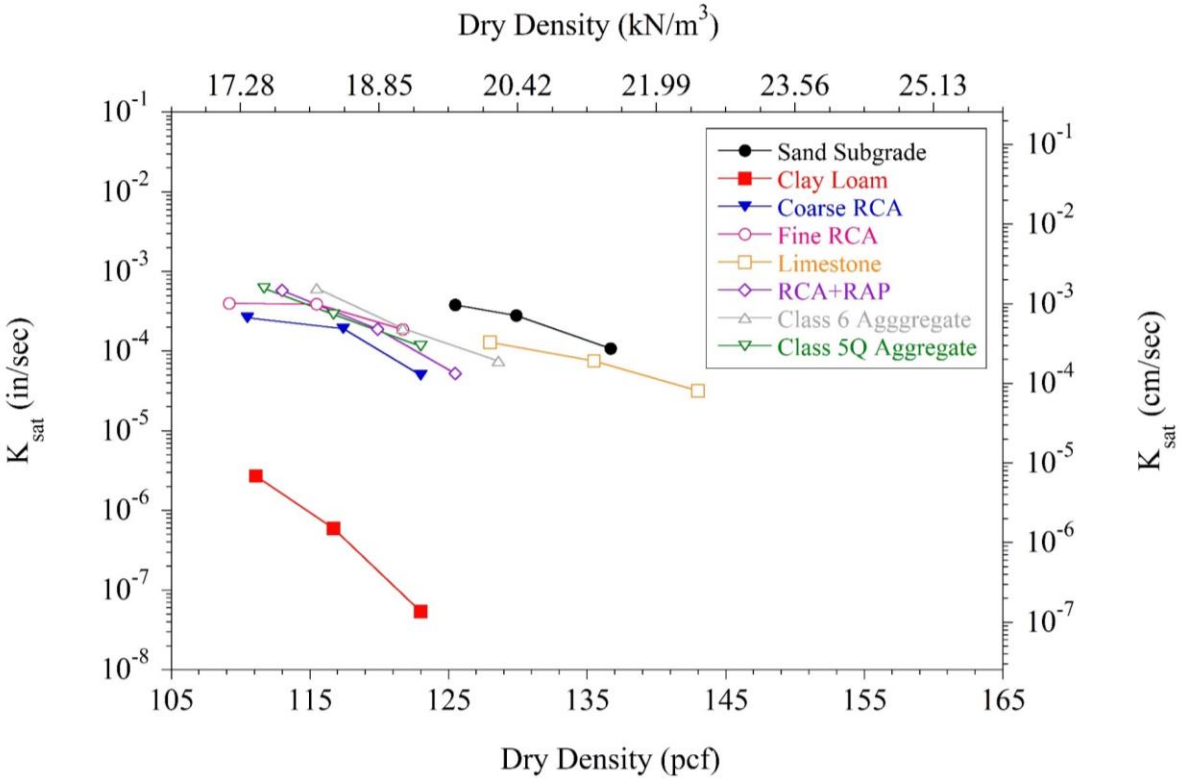

Figure 4.10. Effect of the DOC on the K_{sat} values of the materials

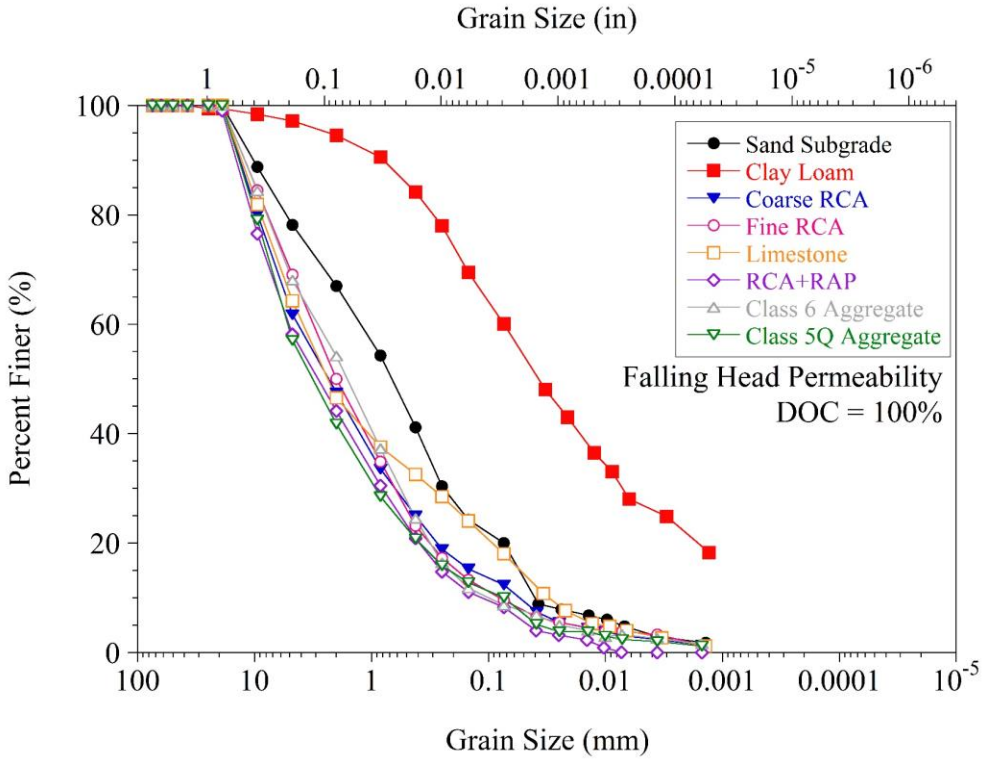

Figure 4.11. Particle size distributions of the falling head permeability test specimens

Table 4.1. Compositions of the falling head permeability test specimens

Material	Gravel (%)	Sand (%)	Fines (%)
Coarse RCA	38.2	49.4	12.4
Fine RCA	30.9	59.5	9.6
Limestone	35.7	46.2	18.1
RCA+RAP	41.8	49.9	8.3
Class 6 Aggregate	31.9	59.4	8.7
Class 5Q Aggregate	42.9	47	10.1
Sand Subgrade	21.8	58.2	20
Clay Loam	2.8	37.1	60.1

Fines = silt and clay

4.2. Soil-Water Characteristic Curve (SWCC)

Soil-water characteristic curve (SWCC) describes the relationship between the volumetric water content of the soil and the soil matric suction (i.e. negative matric potential). SWCC is used to describe the hydraulic properties of unsaturated soils. The variation of the matric suction value in the axes of water content, volumetric water content or saturation degree, whichever plays the leading role in the magnitude of the absorption value, is studied. The relationship between SWCC, permeability, stiffness, and shear resistance can be established. Gradation, morphology, mineralogy, stress history, and weathering of the soil affect the shape of the SWCC. Natural, compacted, and remolded soils also show different SWCC characteristics.

SWCC consists of two curves: wetting (absorption) and drying (desorption) curves (Likos et al. 2013) (Figure 4.12). Hysteresis is a phenomenon that affects the unsaturated hydraulic properties of soils. It is the difference between the matric suctions on the wetting and drying curves (Figure 4.12) (Ebrahimi-Birang et al. 2007). For the same matric suction, the drying curve shows relatively higher volumetric water content than the wetting curve due to hysteresis (Likos et al. 2013). The difference between the two curves is influenced by several factors including the pore water composition and the pore structure. In general, only the drying curve is measured for soils due to the difficulty of obtaining the wetting curve (Hillel 1980, as cited in Nokkaew et al. 2012).

The volumetric water content and matric suction relationship consist of three stages during drying (Figure 4.12). In the first stage, the saturation level of the soil does not decrease considerably in response to the increase in the matric suction. In this stage, the void ratio decreases due to shrinkage.

In the second stage, the so-called desaturation stage, the air starts to enter into the soil voids at the air-entry pressure (or bubbling pressure), which is the pressure required to start desaturation of the largest pores in the soil (Fredlund and Rahardjo 1993). When the matric suction keeps increasing after reaching the air-entry pressure, significant volumes of water begins to flow out of the soil as air enters the soil cavities. For well graded soils, the reduction in the water content is gentler. On the other hand, for uniformly graded soils, this reduction is steeper.

In the third stage, the so-called residual stage, some amount of water remains in the smallest voids. At this stage, a large increase in the matric suction is required for the discharge of water from the smallest voids. Many clayey soils can hold a significant amount of water and require very high matric suction to release the residual water content while still exhibiting a volume reduction and a high degree of saturation of up to 80%. In accordance with the laws of thermodynamics, the total suction value for soil at zero water content is around 145 ksi (1000 MPa).

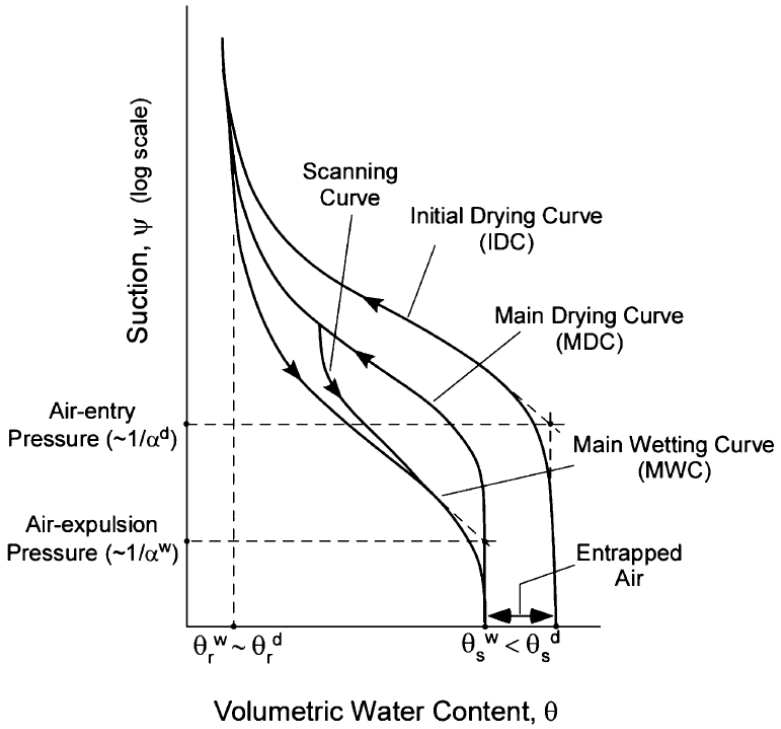

Figure 4.12. Drying curve, wetting curve, and typical hysteretic behavior of soil (Likos et al. 2013)

Three different tests were performed to determine the SWCCs of all the materials excluding Select Granular Borrow and LSSB material. These tests included the hanging column test, the pressure plate test, and the activity meter test (ASTM D6836).

Hanging column tests were carried out on Sand Subgrade, Class 6 Aggregate, and Class 5Q Aggregate with matric suction values up to around 6 psi (40 kPa). A diagram of the hanging column test setup is provided in Figure 4.13. The pictures of the test setup are provided in Figure 4.14. The specimen, which was placed in a retaining ring, was placed on a ceramic disc into a glass funnel. Suction was created by the upper and lower reservoirs and applied to the specimen. The volume of the water, which was entering and leaving the specimen was observed in the horizontal tube. In this testing, the water content balance throughout the specimen was achieved within a period of not more than 1-2 days. To plot the SWCC curves, the test data was used to develop the van Genuchten model (van Genuchten 1980) described in Equation 1.

$$\Theta = \frac{\theta - \theta_r}{\theta_s - \theta_r} = \left[\frac{1}{1 + (\alpha\psi)^n}\right]^m \quad (1)$$

where Θ is the normalized volumetric water content, θ is the soil volumetric water content, θ_r is the residual volumetric water content, θ_s is the saturated volumetric water content, Ψ is the matric suction (kPa), and α, n, and m are the van Genuchten fitting parameters (van Genuchten 1980).

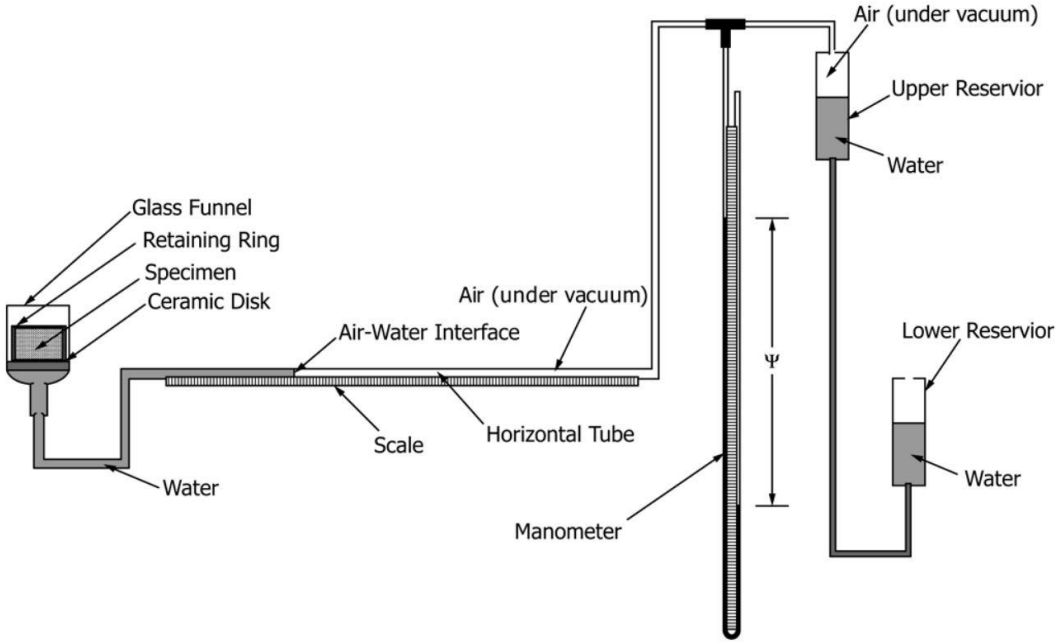

Figure 4.13. Schematic diagram of the hanging column test setup (ASTM D6836)

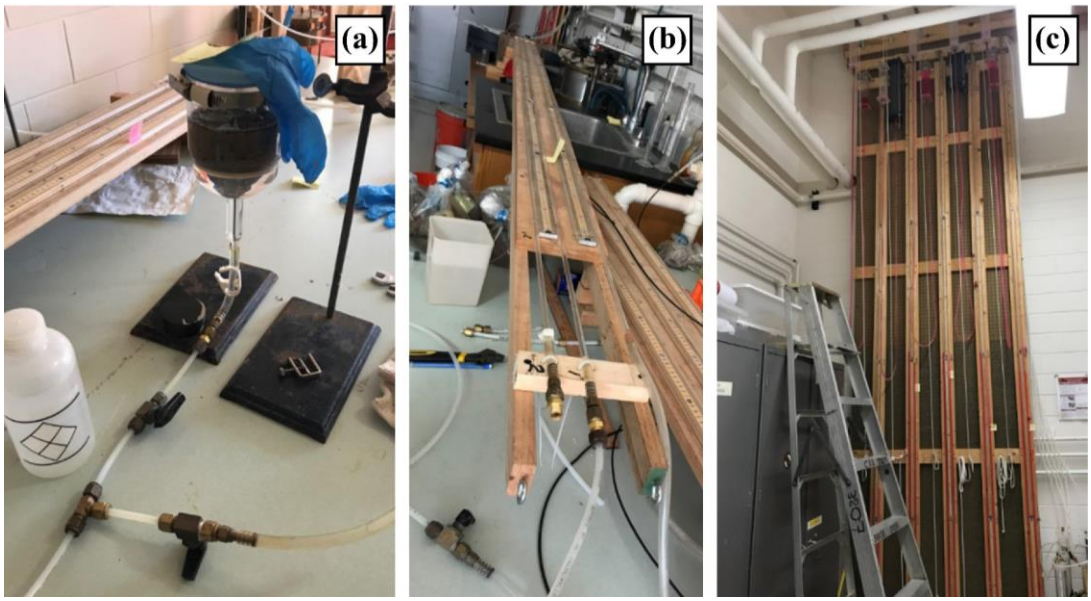

Figure 4.14. Pictures of the hanging column test setup (a) glass funnel, (b) horizontal tube, and (c) manometer

The hanging column test results are provided in Figures 4.15, 4.16, and 4.17 for Sand Subgrade, Class 6 Aggregate, and Class 5Q Aggregate, respectively. The test methodology was successful for Sand Subgrade and Class 6 Aggregate overall. However, some of the tests on Class 5Q Aggregate had to be redone because no satisfactory model fitting could be obtained between the

test data and the van Genuchten model (Figure 4.18). In addition, in the next step, another hanging column test was performed on Fine RCA and the test result did not exhibit a good fit with the van Genuchten model (Figure 4.19). Since both Fine RCA and Class 5Q Aggregate contained RCA particles, this result was attributed to the cementation of the unhydrated cement in the RCA matrix (Figure 4.20). Cementation occurred during the long testing period and it caused difficulty for the water to flow out and created a risk regarding ceramic pore-clogging. In addition, the hanging column test is more suitable for coarse materials. Fines contents of the Class 5Q Aggregate and Fine RCA specimens could be higher than the hanging column test limitations. Therefore, instead of hanging column test, pressure plate and activity meter tests were performed on the rest of the materials.

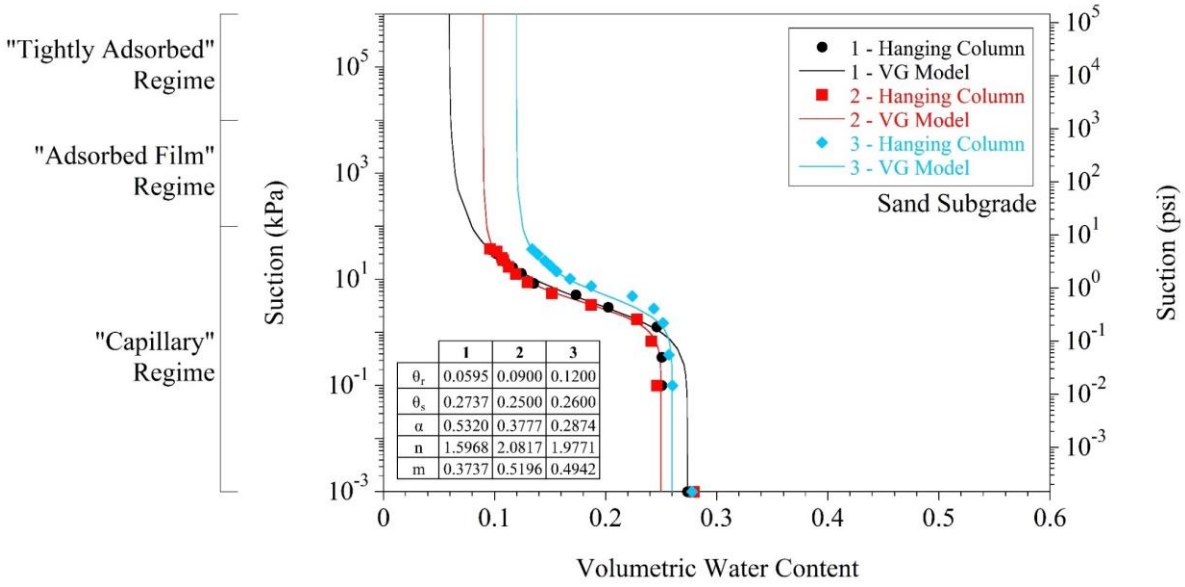

Figure 4.15. SWCC of Sand Subgrade by the hanging column test

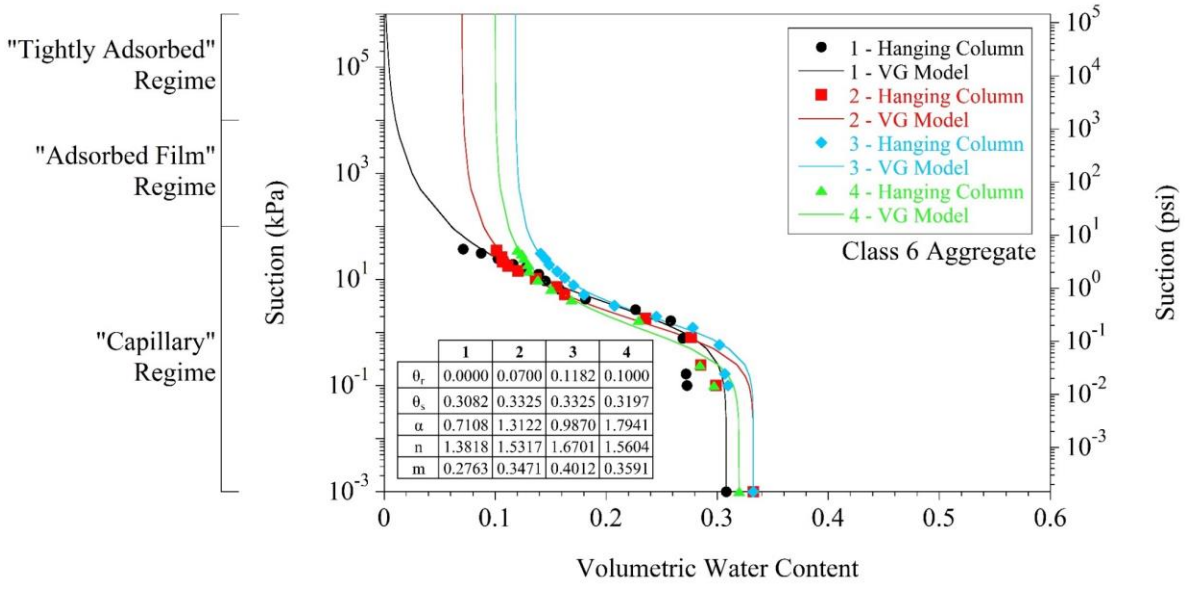

Figure 4.16. SWCC of Class 6 Aggregate by the hanging column test

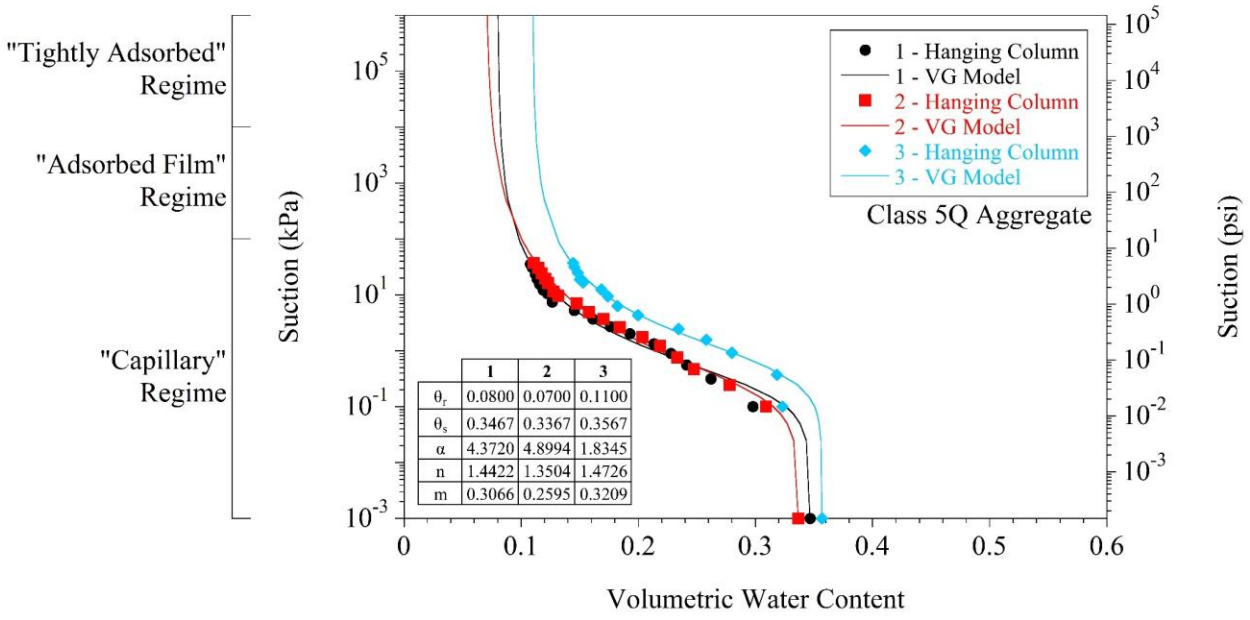

Figure 4.17. SWCC of Class 5Q Aggregate by the hanging column test

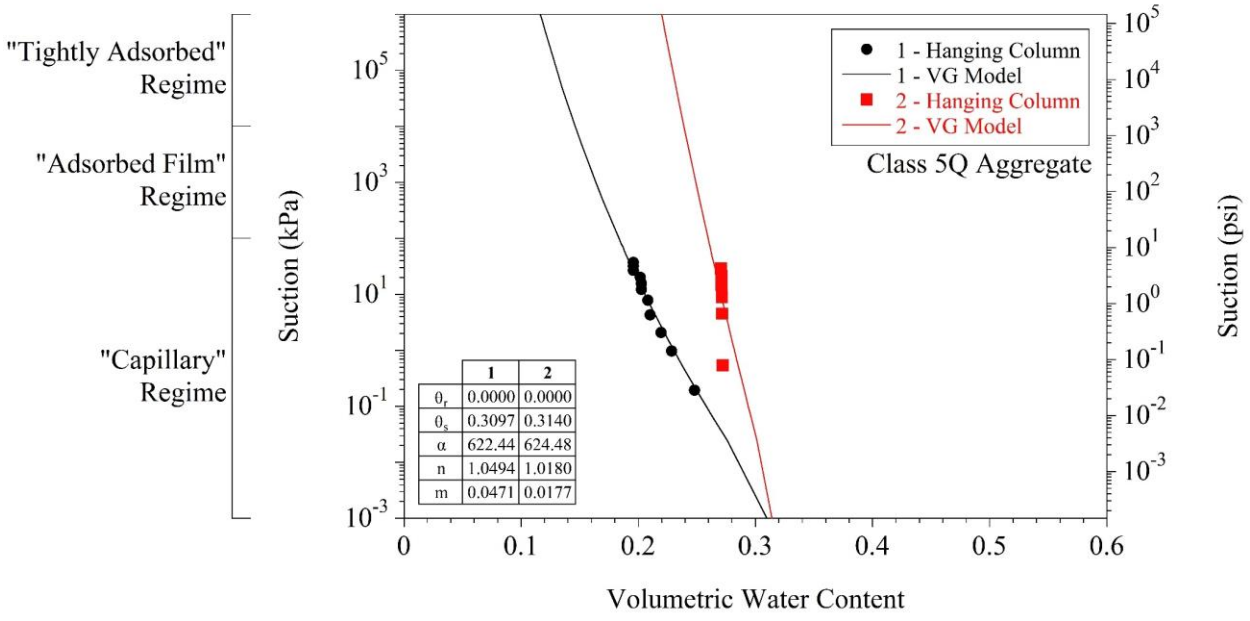

Figure 4.18. Hanging column test data and the van Genuchten model for Class 5Q Aggregate

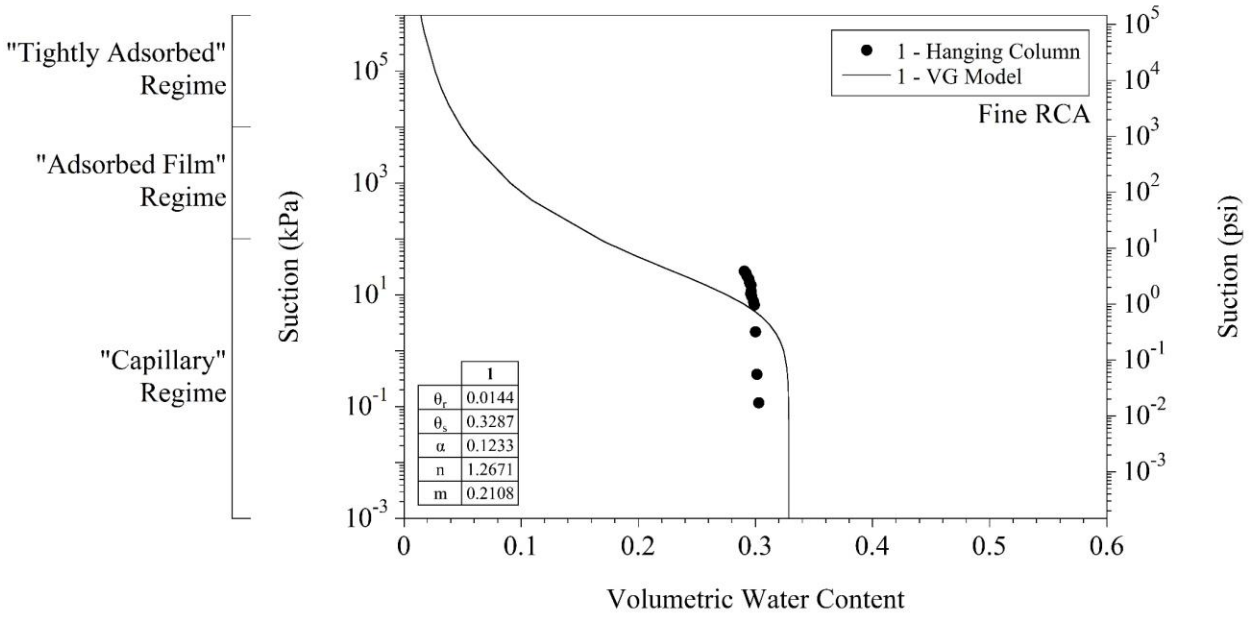

Figure 4.19. Hanging column test data and the van Genuchten model for Fine RCA

Figure 4.20. Cementation of Fine RCA after the hanging column test

The pressure plate and activity meter tests were carried out on Clay Loam, Coarse RCA, Fine RCA, Limestone, and RCA+RAP. Pressure plate tests were performed on the materials passing 3/8-in sieve at matric suction values up to around 220 psi (1500 kPa). Figure 4.21 shows the pressure chambers, which were used for the pressure plate tests. 3-in diameter and 1-in height specimens were compacted in three layers in a ring in the pressure chamber (Figure 4.22). The specimens were then saturated by applying a vacuum in the desiccator and placed in the pressure plate cell. The volume of the water entering and leaving the specimen was measured by means of the horizontal tube as in the hanging column method [Figures 4.13 and 4.14(b)]. By checking the water level in the horizontal tube, it was observed whether the water content of the specimen was constant. This period took around 3 to 10 days for each suction stage.

Even higher suction values had to be applied to the specimens for being able to reach to the residual water contents. Depending on the fines content of the specimen, it was not always possible to reach the residual water content [the water content at which the slope of the SWCC becomes zero in the

third stage, the so-called residual stage (van Genuchten 1980)] in the SWCC by the pressure plate test because of the maximum matric suction that could be created by that method [220 psi (1500 kPa)]. An activity meter device (Figure 4.23) was operated to obtain data at much higher suction values. In fact, the activity meter does not apply suction to the specimens directly. Instead, it measures the relative humidity and then converts the readings to matric suction values by Kelvin's Law, which indicates that the relative humidity and suction are directly related parameters (Sposito 1981; Likos and Lu 2003). The activity meter tests were performed on the finer fractions of the materials [passing No. 10 sieve (2 mm)] because the larger particles are not suitable for this method. 1.6-in (40-mm) diameter specimens were used for the activity meter tests. Since the specimen size that can be used in this testing was relatively smaller, it was actually not possible to provide a representative specimen in terms of the actual gradation of the corresponding material (Figure 3.1 and Table 3.1). It should be noted that the compaction status of the specimen was not important at a high level of suction. In other words, the pore structure of the specimen plays a negligible role at very high suction values. In the high suction rates, it is the properties of the mineral surfaces that dominate the SWCC behavior of the materials.

Figure 4.21. Single-specimen pressure chambers

Figure 4.22. Compacted specimen prepared in a ring in the pressure chamber

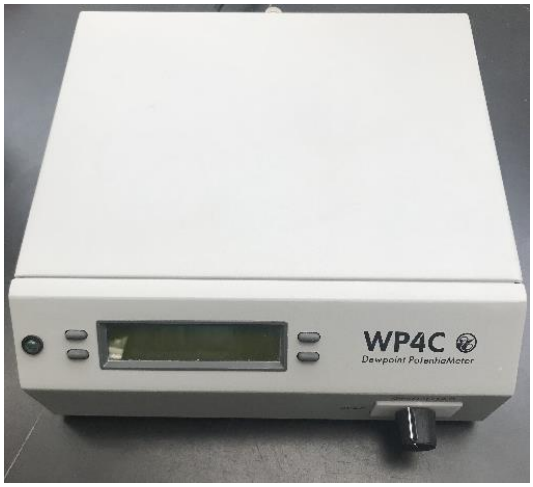

Figure 4.23. Activity meter device

The data collected by the pressure plate and the activity meter tests were combined and used to develop the van Genuchten model (van Genuchten 1980), as described previously in Equation 1. The data obtained from the activity meter was at very high suction [> 220 psi (1500 kPa)] and the data obtained from the pressure plate was at relatively lower suctions [< 220 psi (1500 kPa)]. Combining the data obtained from the two different methods caused discontinuities to some extent. Pressure plate and activity meter test results are provided in Figures 4.24, 4.25, 4.26, 4.27, and 4.28 for Clay Loam, Coarse RCA, Fine RCA, Limestone, and RCA+RAP, respectively.

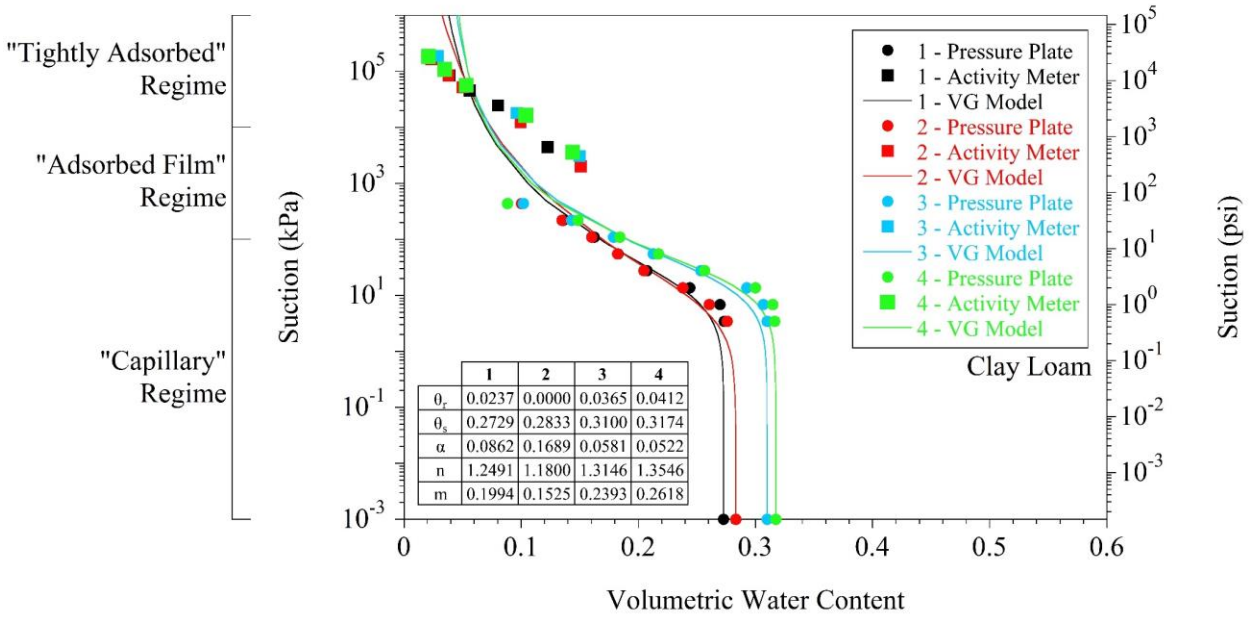

Figure 4.24. SWCC of Clay Loam by the pressure plate and the activity meter tests

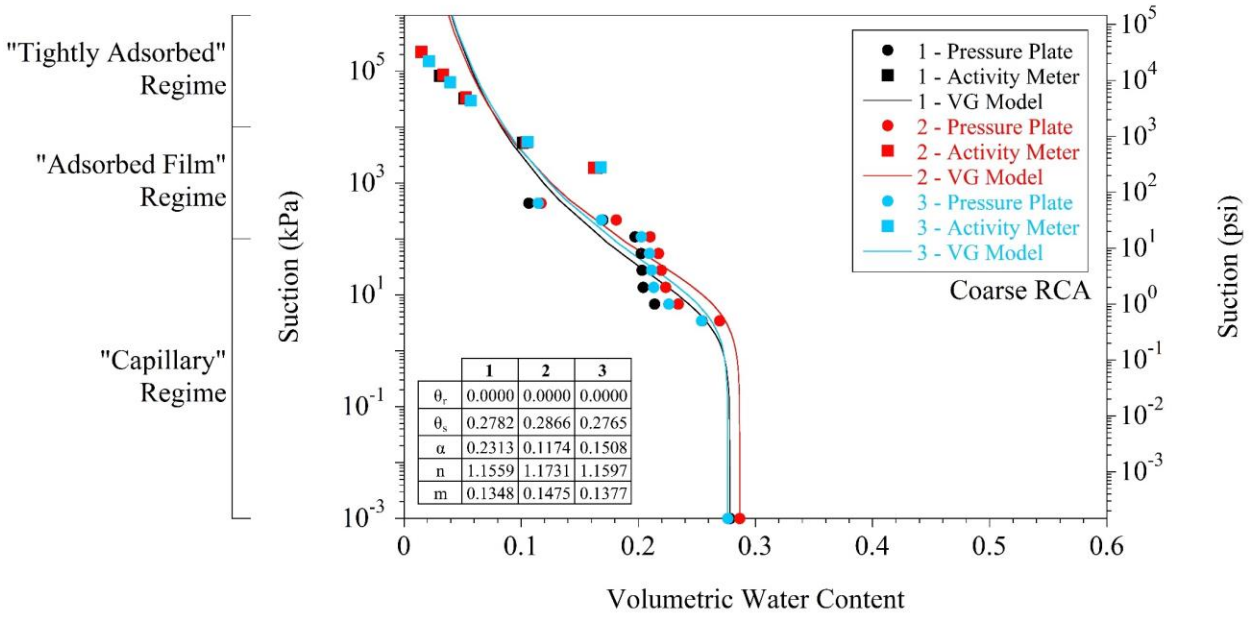

Figure 4.25. SWCC of Coarse RCA by the pressure plate and the activity meter tests

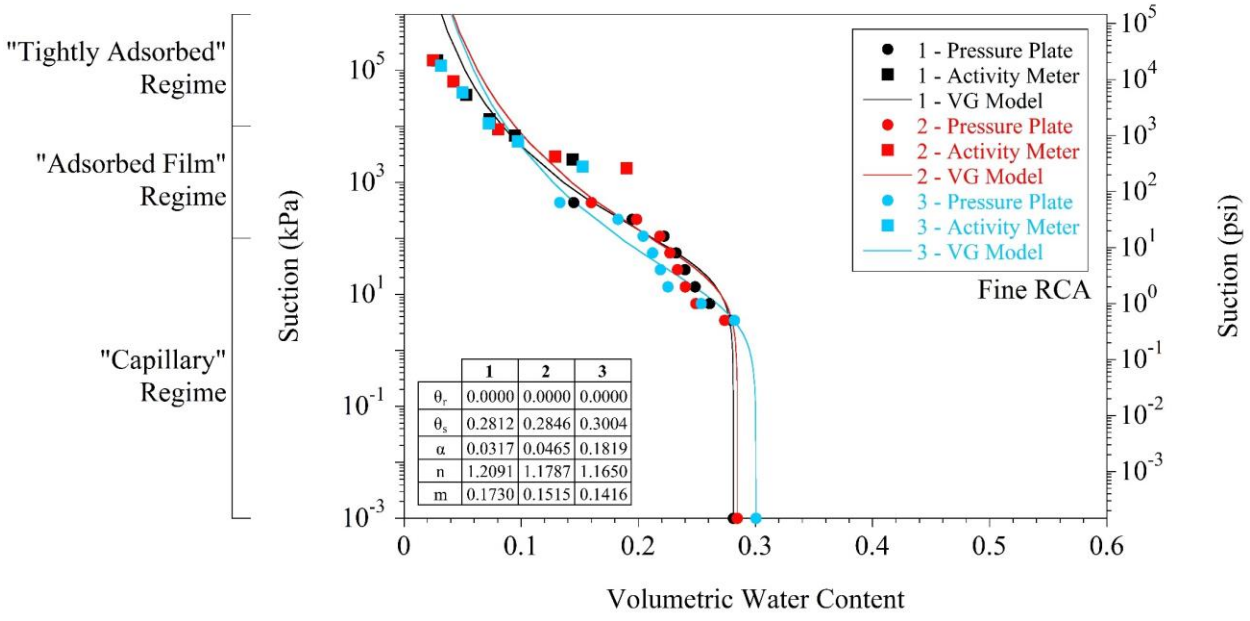

Figure 4.26. SWCC of Fine RCA by the pressure plate and the activity meter tests

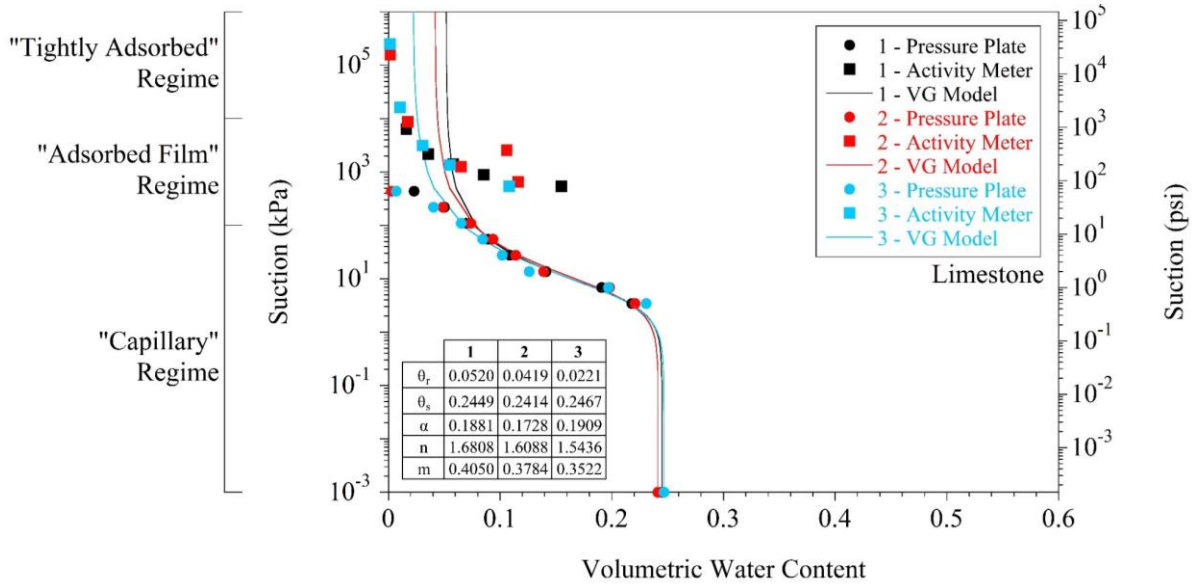

Figure 4.27. SWCC of Limestone by the pressure plate and the activity meter tests

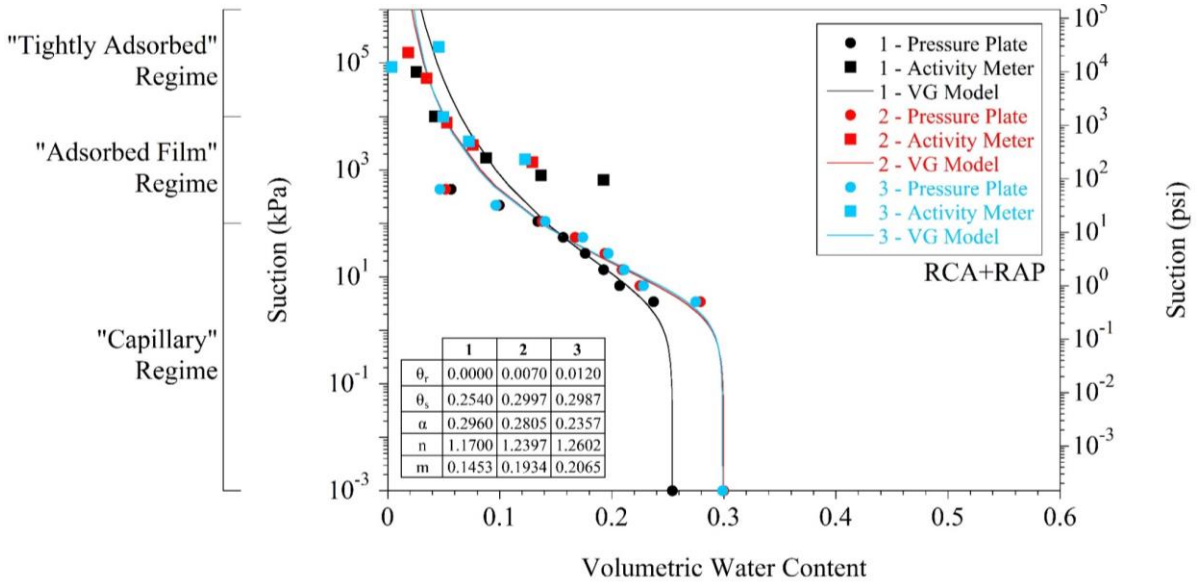

Figure 4.28. SWCC of RCA+RAP by the pressure plate and the activity meter tests

The van Genuchten models of different specimens from the same material were averaged and one summary model for each material is shown in Figure 4.29. Volumetric water content at the fully saturated condition and air-entry pressure of each material are summarized in Table 4.2. Class 5Q Aggregate and Class 6 Aggregate exhibited the highest and the second highest volumetric water content at fully saturated conditions (0.347 and 0.323, respectively). In descending order, volumetric water contents of 0.296, 0.289, 0.284, 0.280, 0.261, and 0.244 were observed for Clay Loam, Fine RCA, RCA+RAP, Coarse RCA, Sand Subgrade, and Limestone, respectively, at fully saturated conditions. Fine RCA and Clay Loam exhibited the highest air-entry pressures (4 and 3.5, respectively). Then, in descending order, air-entry pressure values of 2.5, 1.75, 1.40, 0.85, 0.30, and 0.10 kPa were observed for Coarse RCA, Limestone, RCA+RAP, Sand Subgrade, Class 6 Aggregate, and Class 5Q Aggregate, respectively.

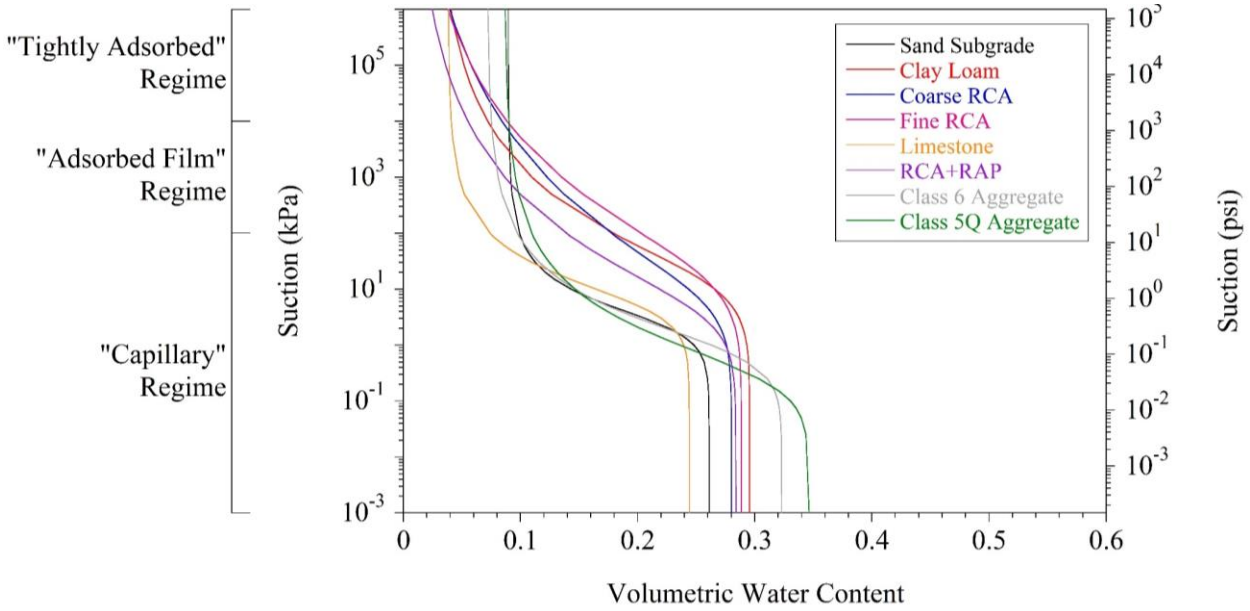

Figure 4.29. van Genuchten models of all materials

Table 4.2. Volumetric water content at the fully saturated condition and air-entry pressure of each material

Material	Initial Volumetric Water Content	Air-Entry Pressure	
		(kPa)	(psi)
Sand Subgrade	0.261	0.85	0.12
Clay Loam	0.296	3.50	0.51
Coarse RCA	0.280	2.50	0.36
Fine RCA	0.289	4.00	0.58
Limestone	0.244	1.75	0.25
RCA+RAP	0.284	1.40	0.20
Class 6 Aggregate	0.323	0.30	0.04
Class 5Q Aggregate	0.347	0.10	0.01

To observe the effects of the DOC on the SWCC characteristics of each material, the 3-in diameter and 1-in height specimens were prepared from all the materials except Select Granular Borrow and LSSB material. All specimens except the Fine RCA specimens were compacted in three layers in the ring by three different compaction energies to obtain 100, 95, and 90% DOC [based on the uncorrected MDD of the materials (Figure 3.2 and Table 3.3)]. The Fine RCA specimens were compacted in the ring at 100, 90, and 80% DOC (Figure 3.2 and Table 3.3). In the beginning, the target DOC values were determined to be 100, 90, and 80%. All materials except Fine RCA could not be removed from the mold without significant disturbance when they were compacted at 80% DOC. Therefore, all materials except Fine RCA were compacted at 100, 95, and 90% DOC.

All specimens were compacted at their corresponding OMCs (Figure 3.2 and Table 3.3). The pressure plate and the activity meter tests were performed, and their result were evaluated. Test

results for Sand Subgrade, Clay Loam, Coarse RCA, Fine RCA, Limestone, RCA+RAP, Class 6 Aggregate, and Class 5Q Aggregate are provided in Figures 4.30, 4.31, 4.32, 4.33, 4.34, 4.35, 4.36, and 4.37 respectively. Volumetric water content at the fully saturated condition and air-entry pressure of each material are summarized in Table 4.3. It was observed that the higher the DOC of the specimens, the lower the initial volumetric water content of the specimens at fully saturated conditions. This was due to the denser structure of the specimens. The denser structure of the specimens yielded lower void ratio values, which in turn lowered the initial volumetric water content at fully saturated conditions. Particle size distributions of the materials used in the tests are summarized in Figure 4.38 and Table 4.4.

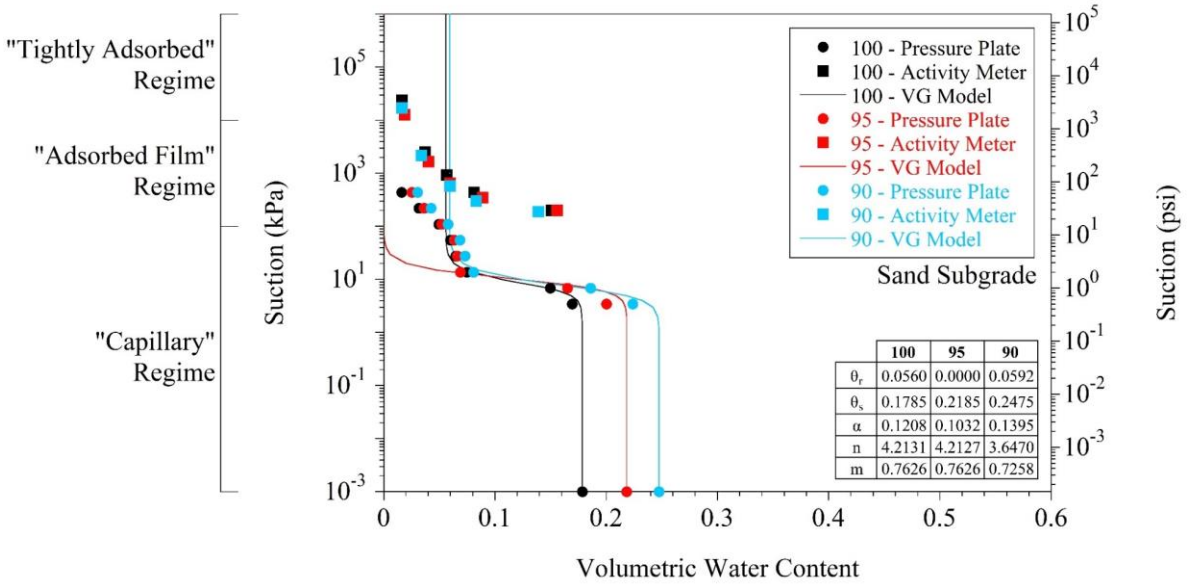

Figure 4.30. Effect of the DOC on the SWCC characteristics of Sand Subgrade

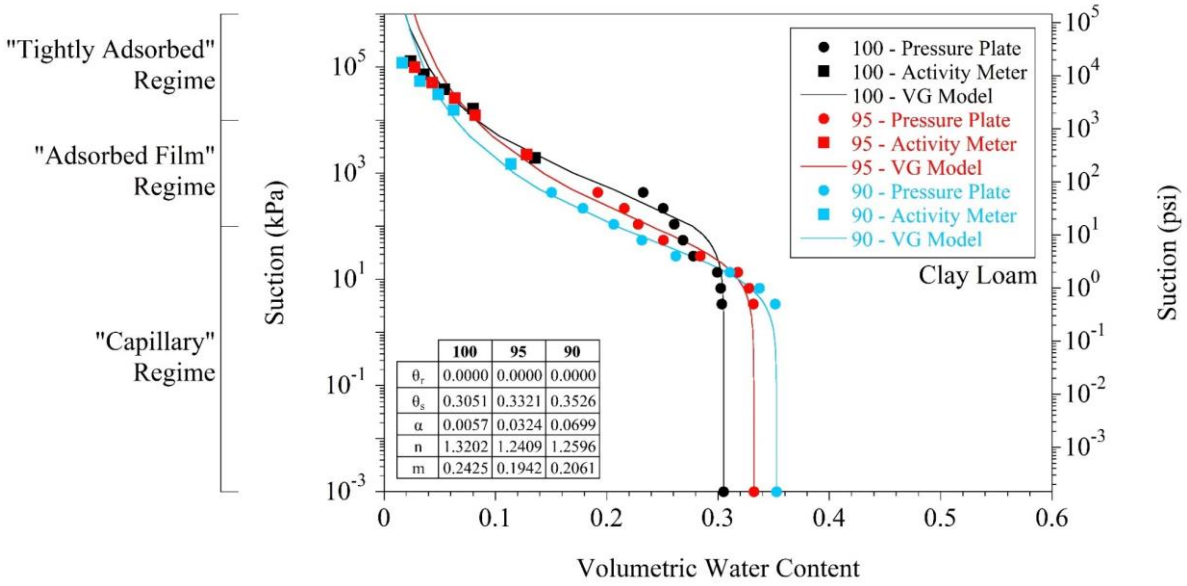

Figure 4.31. Effect of the DOC on the SWCC characteristics of Clay Loam

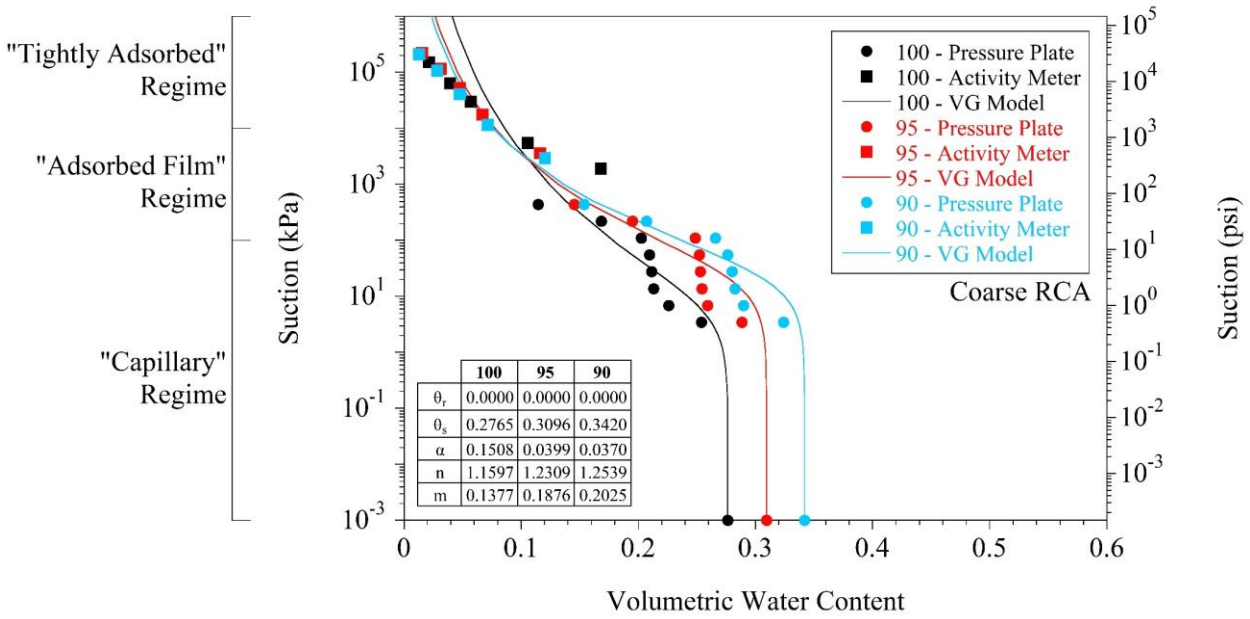

Figure 4.32. Effect of the DOC on the SWCC characteristics of Coarse RCA

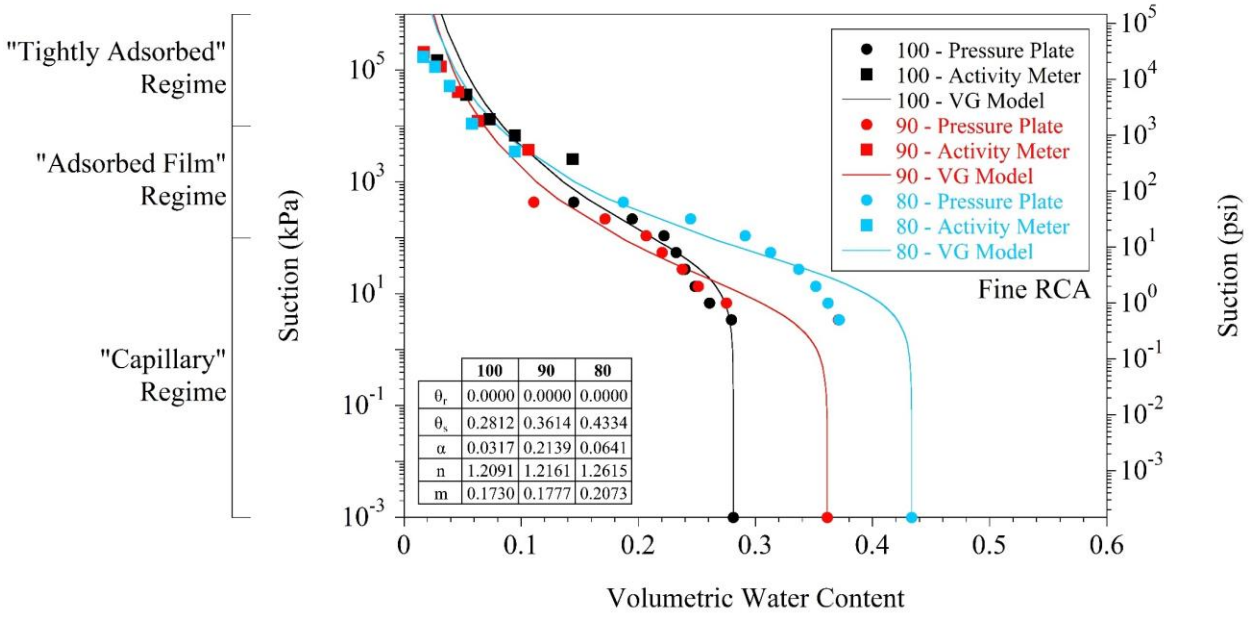

Figure 4.33. Effect of the DOC on the SWCC characteristics of Fine RCA

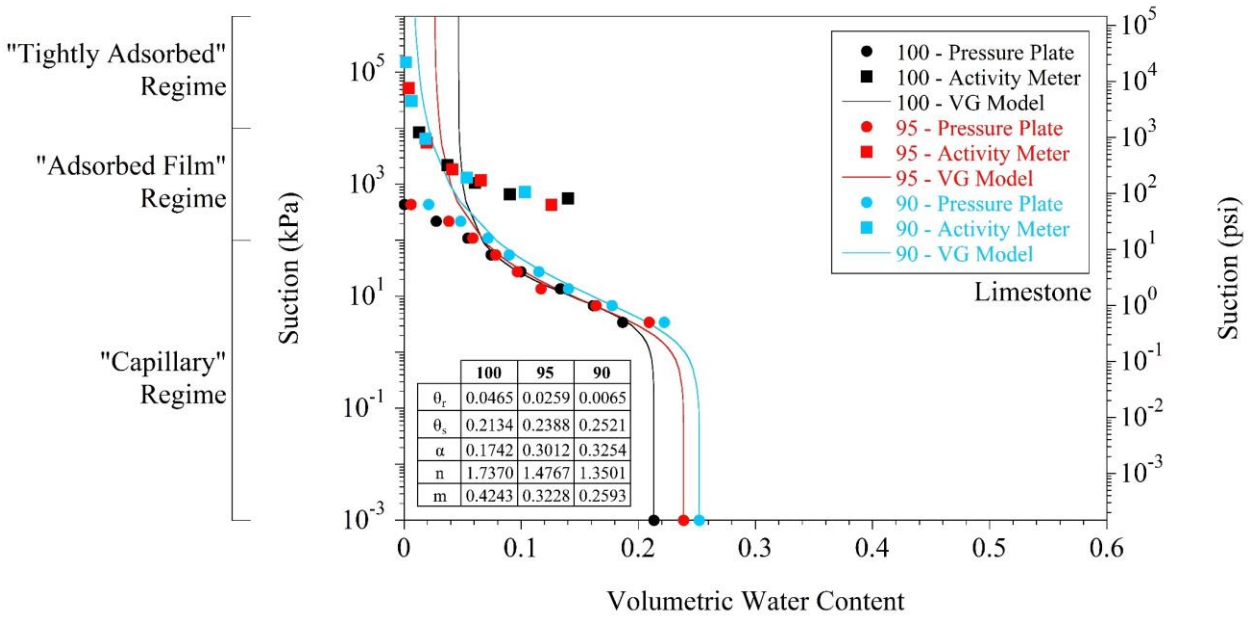

Figure 4.34. Effect of the DOC on the SWCC characteristics of Limestone

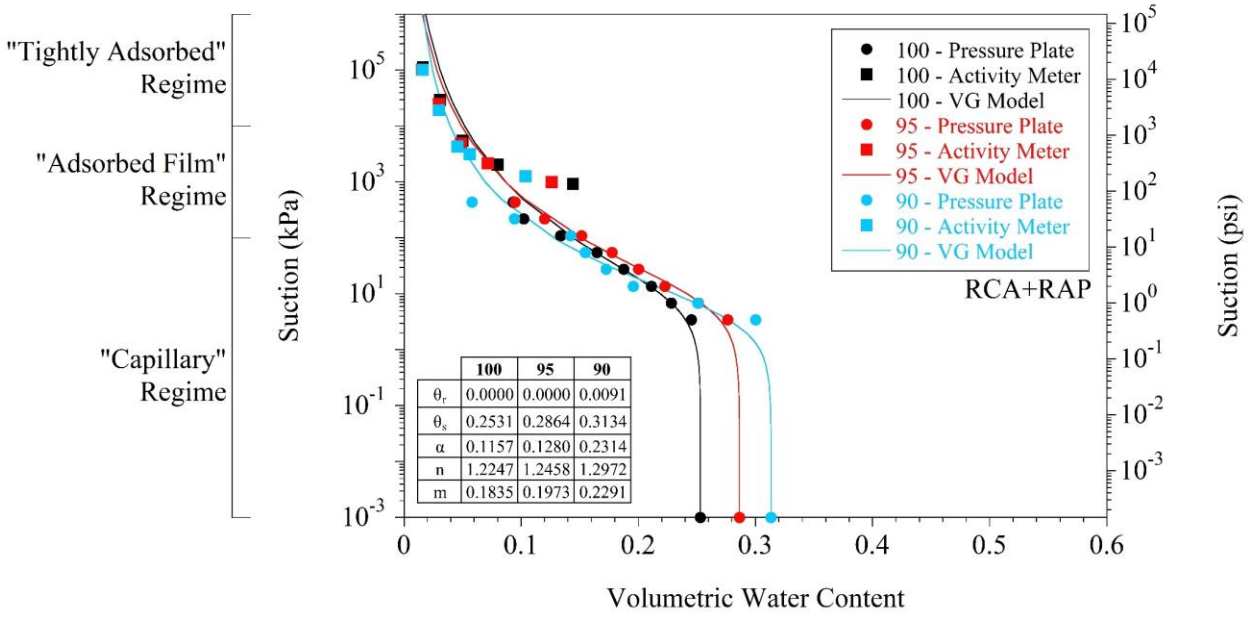

Figure 4.35. Effect of the DOC on the SWCC characteristics of RCA+RAP

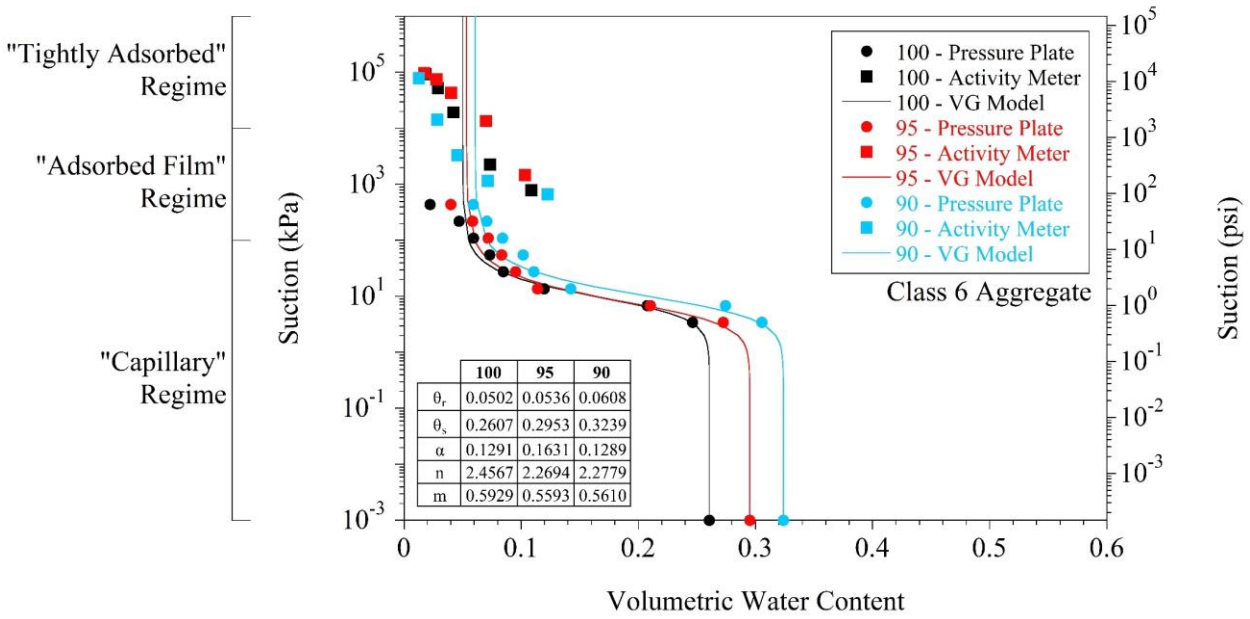

Figure 4.36. Effect of the DOC on the SWCC characteristics of Class 6 Aggregate

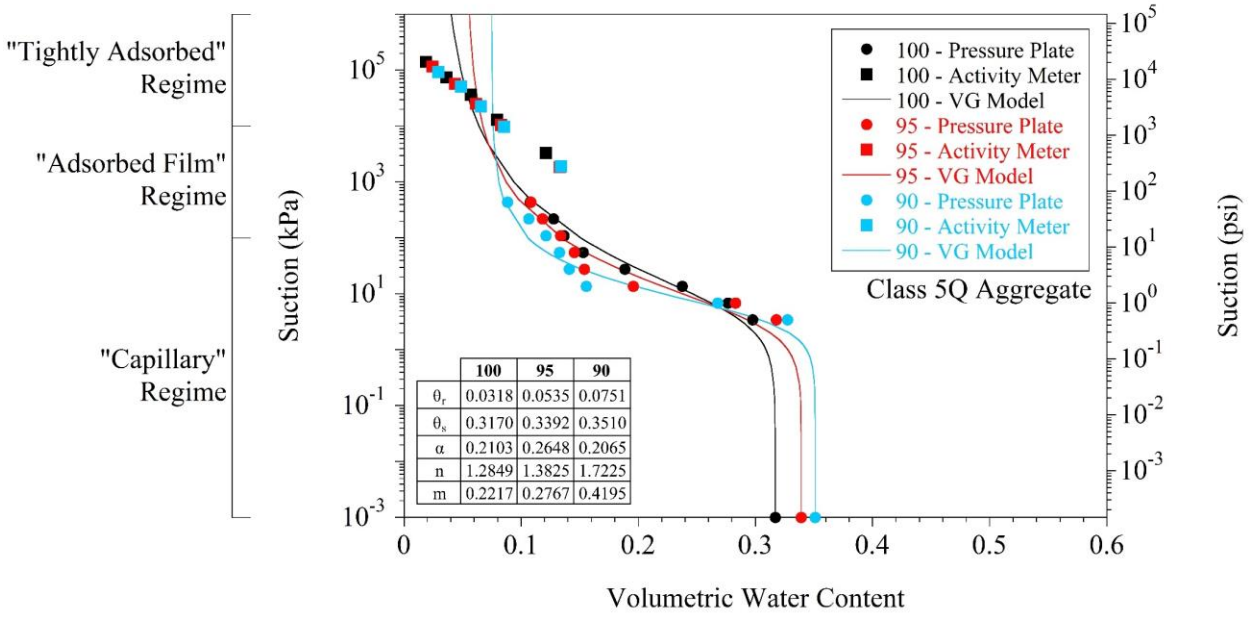

Figure 4.37. Effect of the DOC on the SWCC characteristics of Class 5Q Aggregate

Table 4.3. Volumetric water content at the fully saturated condition and air-entry pressure of each material at different DOC

Material	DOC (%)	Initial Volumetric Water Content	Air-Entry Pressure	
			(kPa)	(psi)
Sand Subgrade	100	0.1785	5	0.73
	95	0.2185	4.8	0.70
	90	0.2475	3.5	0.51
Clay Loam	100	0.3051	14.5	2.10
	95	0.3321	10	1.45
	90	0.3526	5	0.73
Coarse RCA	100	0.2765	3	0.44
	95	0.3096	10	1.45
	90	0.3420	9	1.31
Fine RCA	100	0.2812	10.5	1.52
	90	0.3614	2	0.29
	80	0.4334	5	0.73
Limestone	100	0.2134	2.5	0.36
	95	0.2388	1.5	0.22
	90	0.2521	1.25	0.18
RCA+RAP	100	0.2531	3.5	0.51
	95	0.2864	3	0.44
	90	0.3134	1.5	0.22
Class 6 Aggregate	100	0.2607	3	0.44
	95	0.2953	2.5	0.36
	90	0.3239	3	0.44
Class 5Q Aggregate	100	0.3170	1.75	0.25
	95	0.3392	1.25	0.18
	90	0.3510	1.75	0.25

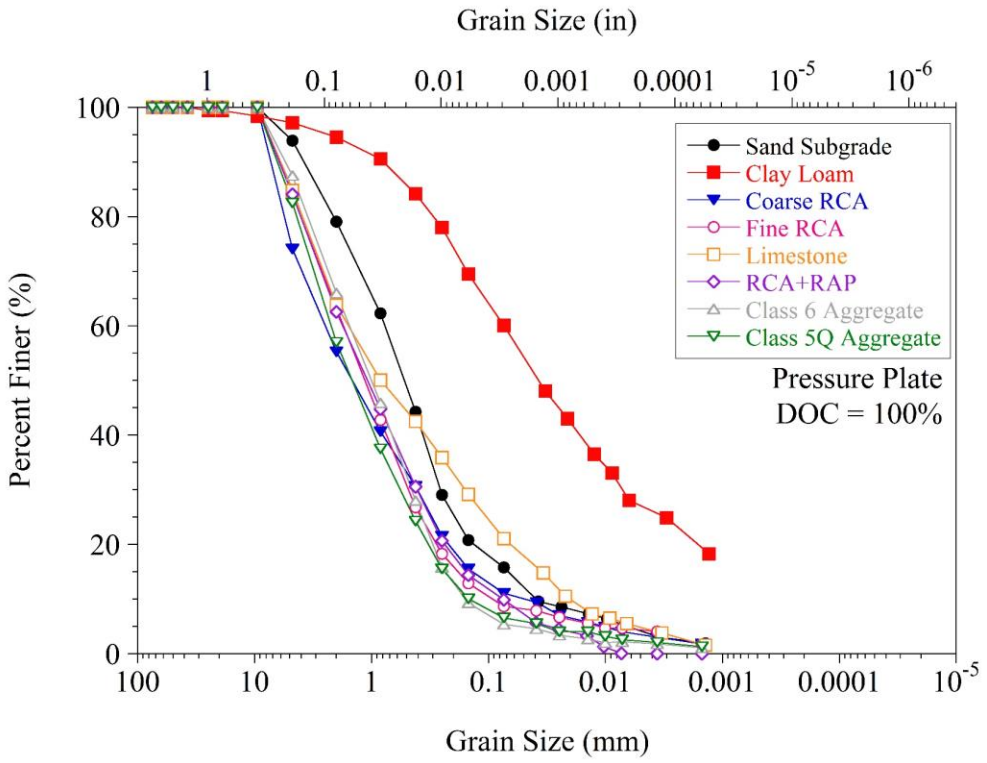

Figure 4.38. Particle size distribution of the pressure plate test specimens

Table 4.4. Compositions of the pressure plate test specimens

Material	Gravel (%)	Sand (%)	Fines (%)
Coarse RCA	25.9	63.0	11.1
Fine RCA	15.1	76.2	8.7
Limestone	15.2	63.7	21.1
RCA+RAP	15.9	74.2	9.9
Class 6 Aggregate	12.5	82.1	5.4
Class 5Q Aggregate	17.5	75.9	6.6
Sand Subgrade	6.1	78.1	15.8
Clay Loam	2.8	37.1	60.1

5. STEREOPHOTOGRAPHY

Particle size and shape characteristics of aggregates must be well known since the engineering properties of aggregates (shear strength, stiffness, permeability, etc.) are significantly affected by these parameters (Cosentino et al. 2003; Tan et al. 2014; Zheng and Hryciw 2014, 2017). The conventional method to determine the particle shape characteristics (elongation and flatness) of aggregates is to measure the length, width, and thickness of the particles by a caliper device (ASTM D4791). Since aggregate particles are evaluated individually by the conventional method, the process is slow (Zheng and Hryciw 2017). In addition, due to the limitations of the size of the existing test equipment, sieve analysis may not be practical for testing of large stones. Several

digital imaging techniques have been developed by researchers as an alternative to standard sieve and particle shape analyses (Fletcher et al. 2003; Kumara et al. 2012; Altuhafi et al. 2013; Ohm and Hryciw 2013; Kazmee et al. 2016). Overall, these techniques were successful. However, most of them contained imperfections such as neglecting or roughly predicting the thickness of aggregate particles, or they were impractical. The length and width of an aggregate particle can be determined from a 2D model, which is simply a single image of the particle at a known scale (Ghalib and Hryciw 1999; Hryciw and Ohm 2012; Ohm and Hryciw 2013). However, the thickness of the aggregate particle cannot be measured by the 2D model (Zheng and Hryciw 2014, 2017). Stereophotography is a promising technique to determine particle size and shape (sphericity and roundness) characteristics of aggregates. In stereophotography, the image analysis algorithm combines two images, which are captured from two different positions, and creates a 3D half surface model to determine such characteristics of aggregates (Zheng and Hryciw 2014, 2017). The image analysis algorithm includes basic matching, dynamic programming, pyramidal matching, and sub-pixel estimation functions (Zheng and Hryciw 2014, 2017). These functions identify corresponding points between two images and back-calculate the physical distance between the points in the image and the camera. Detailed mathematical derivation of the process is provided by Zheng and Hryciw (2014, 2017).

5.1. Test Method

Stereophotography was performed on all the materials except Sand Subgrade, Clay Loam, and Select Granular Borrow. For Coarse RCA, Fine RCA, Limestone, RCA+RAP, Class 6 Aggregate, and Class 5Q Aggregate, sieve analyses were performed without any problem. However, for LSSB material, sieve analysis was not practical because most of the large particles had to be sieved one by one. The 12-in diameter sieves, which were on hand, could not be stacked on top of each other since a great number of particles were larger than the stacked height (around 1.6 in) of the half-height sieves. In addition, since the sieves could not be stacked, a mechanical sieve shaker could not be used effectively to sieve LSSB material.

The stereophotography system, which was developed for this study, is shown in Figure 5.1. The system was set up on an AV cart [Figure 5.1(a)]. A camera, a camera slider, and LED lighting were installed on the bottom face of the top shelf of the AV cart [Figures 5.1(a), 5.1(b), and 5.1(c)]. It is recommended by Zheng and Hryciw (2017) that two cameras at fixed locations could be placed. The system, developed for this study, had one camera. The camera was a 20.2-megapixel digital camera, which could capture images up to 5184 x 3888 pixels. The camera could be moved horizontally along the camera slider [Figures 5.1(b) and 5.1(c)]. LED lighting provided uniform illumination and improved image sharpness [Figures 5.1(b) and 5.1(c)]. A test surface was set up on the top surface of the bottom shelf of the AV cart [Figures 5.1(a), 5.1(b), and 5.1(d)]. Self-adhesive measuring tapes were placed on the test surface in two directions to specify the area that test material could be placed and to indicate the scales in both directions [Figure 5.1(d)]. A replaceable white ledger size paper (11 x 17 in) was placed on the area that was specified by the measuring tapes (the color of the paper could be different depending upon the color of the aggregate particles).

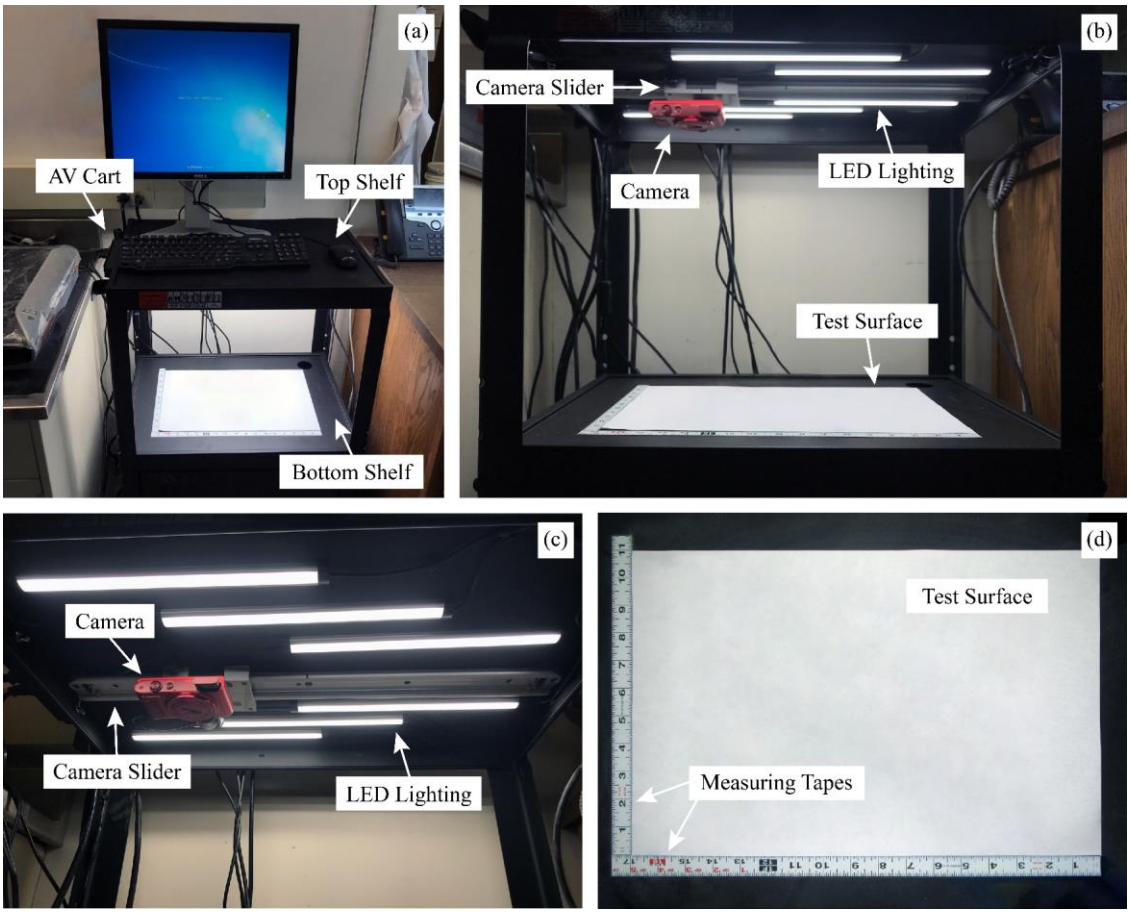

Figure 5.1. (a) AV cart and top and bottom shelves, (b) main components of the stereophotography system, (c) camera, camera slider, and LED lighting, and (d) test surface and self-adhesive measuring tapes

The key parameters for constructing the stereophotography system include the vertical distance between the camera center and the test surface (D_B), the camera separation distance (L), the focal length of the camera (*f*) (Figure 5.2). These parameters can be determined by a system calibration process (Zheng and Hryciw 2014, 2017).

Different D_B values were evaluated by adjusting the height of the top shelf of the AV cart [Figure 5.1(a)]. It was determined that a height of 15.4 inches yielded a satisfactory field of view and depth of focus for the evaluation of the size and shape characteristics of aggregate particles. After fixing the D_B value, different L values were evaluated by sliding the camera to different locations. A large L value may cause a reduction in the number of aggregate particles that could be captured. On the other hand, a small L value may not be suitable to capture the two different sides of aggregate particles effectively. The most appropriate L value was found to be 4 inches. After the determination of the D_B and L values, the *f* value was fixed to 1869 pixels. The detailed information about the system calibration is provided by Zheng and Hryciw (2017).

Particles were placed on the test surface in groups and not allowed to touch each other to eliminate the process of watershed analysis (Zheng and Hryciw 2016). For each group, two pictures [Figures 5.3(a) and 5.3(b)] were taken by shifting the camera at the distance of L = 4 in (Figure 5.2). Then,

the image taken from the left position (the other image could also be used) was converted into a binary image (2D) by a Photoshop program [Figure 5.3(c)] to determine the two dimensions of the particles in the group. As the final step, the two images [Figures 5.3(a) and 5.3(b)] and the binary image [Figure 5.3(c)] were input into a computer code developed in Matlab (Zheng and Hryciw 2017), which generated the 3D half surface model of the particles in the group (Figure 5.4). In the 3D half surface model, the X- and Y-axes show the 2D dimensions of the particles (Figure 5.4). A color legend is also provided to show the variations of the 3rd dimension of the particles in the group (Z-axis) (Figure 5.4). The dark blue color represents the test surface at Z = 0 in (Figure 5.4) and the dark red color represents the highest surface points of the particles (from the test surface, Z = 0 in) (Figure 5.4). All the particles larger than No. 4 sieve (4.75 mm) were selected and analyzed by this method. In total, 4766 LSSB particles, 5160 Coarse RCA particles, 6671 Fine RCA particles, 5527 Limestone particles, 5893 RCA+RAP particles, 5507 Class 6 Aggregate particles, and 5762 Class 5Q Aggregate particles were analyzed.

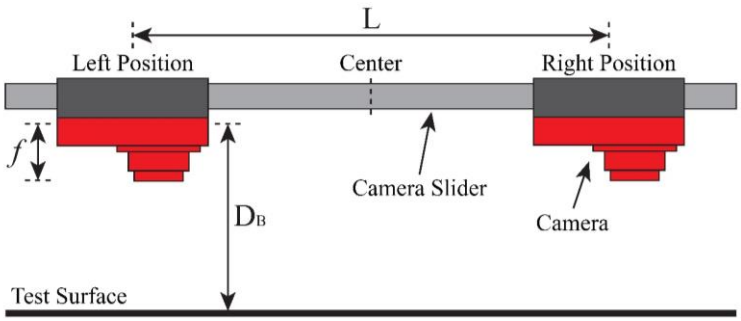

Figure 5.2. Vertical distance between the camera center and the test surface (D_B), the camera separation distance (L), and the focal length of the camera (*f*) (not to scale)

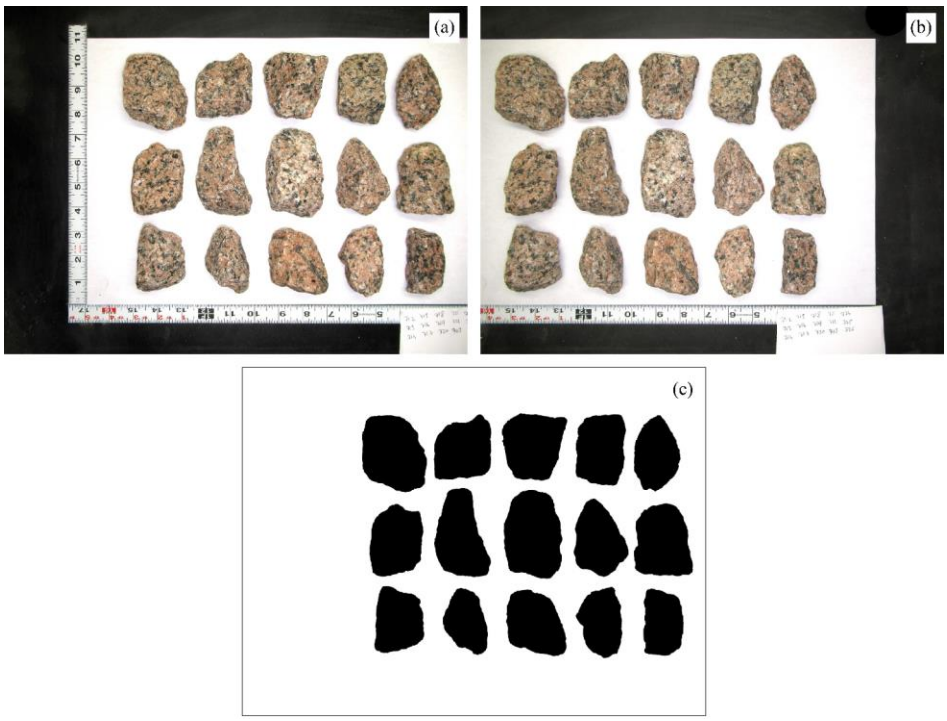

Figure 5.3. (a) Image taken from the left position, (b) image taken from the right position, and (c) binary image for LSSB material

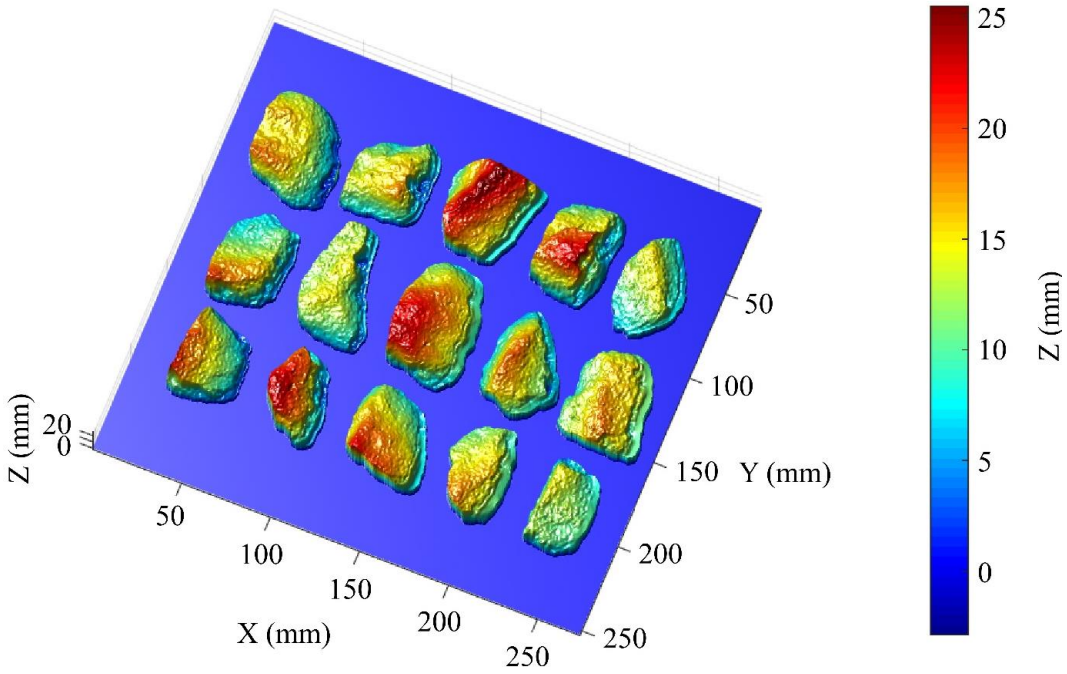

Figure 5.4. 3D half surface model of the group of particles for LSSB material

5.2. Particle Size Analysis

The length (d_1), width (d_2), and thickness (d_3) of each aggregate particle were described as the largest, intermediate, and smallest dimensions, respectively (Zheng and Hryciw 2014, 2017). An ellipsoidal particle model [Figure 5.5(a)] was considered to determine the equivalent sieve opening size (d_e) of each aggregate particle [Figure 5.5(b)] (Zheng and Hryciw 2014, 2017). Equation 2 was used to determine the d_e values (Zheng and Hryciw 2014, 2017).

$$d_e = \sqrt{\frac{d_2^2 + d_3^2}{2}} \tag{2}$$

The volume (V) of each aggregate particle was calculated by Equation 3 (Zheng and Hryciw 2014, 2017). Then, the particle size distribution of the material (by volume) was determined.

$$V = d_1 \times d_2 \times d_3 \tag{3}$$

Stereophotography test results for LSSB material, Coarse RCA, Fine RCA, Limestone, RCA+RAP, Class 6 Aggregate, and Class 5Q Aggregate are provided in Figures 5.6, 5.7, 5.8, 5.9, 5.10, 5.11, and 5.12, respectively. Gradations of the materials, provided in Figure 3.1, are also provided in the figures to compare the results of stereophotography and sieve analysis. Sand and fines contents of the materials could not be determined by stereophotography because only the particles retained on No. 4 sieve (4.75 mm) were used as noted earlier. For LSSB material, it was determined by sieve analysis that sand, silt, and clay particles were only 0.4% by dry weight (Figure 3.1 and Table 3.1). Therefore, even with eliminating the particles passing through No. 4 sieve (4.75 mm), stereophotography provided almost the entire gradation curve for LSSB material. However, since

Coarse RCA, Fine RCA, Limestone, RCA+RAP, Class 6 Aggregate, and Class 5Q Aggregate contained considerable amounts of particles finer than No. 4 sieve (4.75 mm) (Figure 3.1 and Table 3.1), significant portions of the gradation curves of these materials could not be determined by stereophotography. However, for all materials, the result of stereophotography remarkably matched with the result of sieve analysis for the particles larger than No. 4 sieve (4.75 mm).

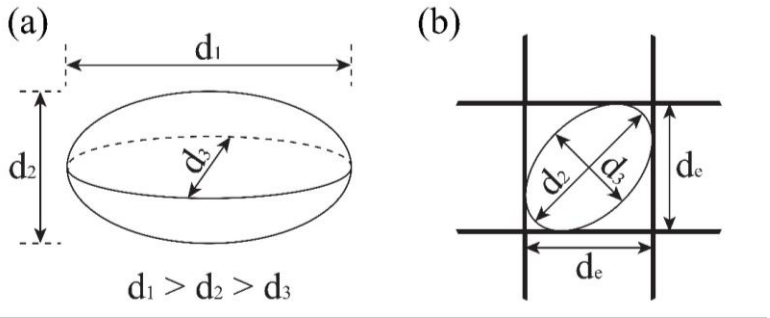

Figure 5.5. (a) Length (d_1), width (d_2), and thickness (d_3), and (b) equivalent sieve opening size (d_e) of the particles (Zheng and Hryciw 2014, 2017)

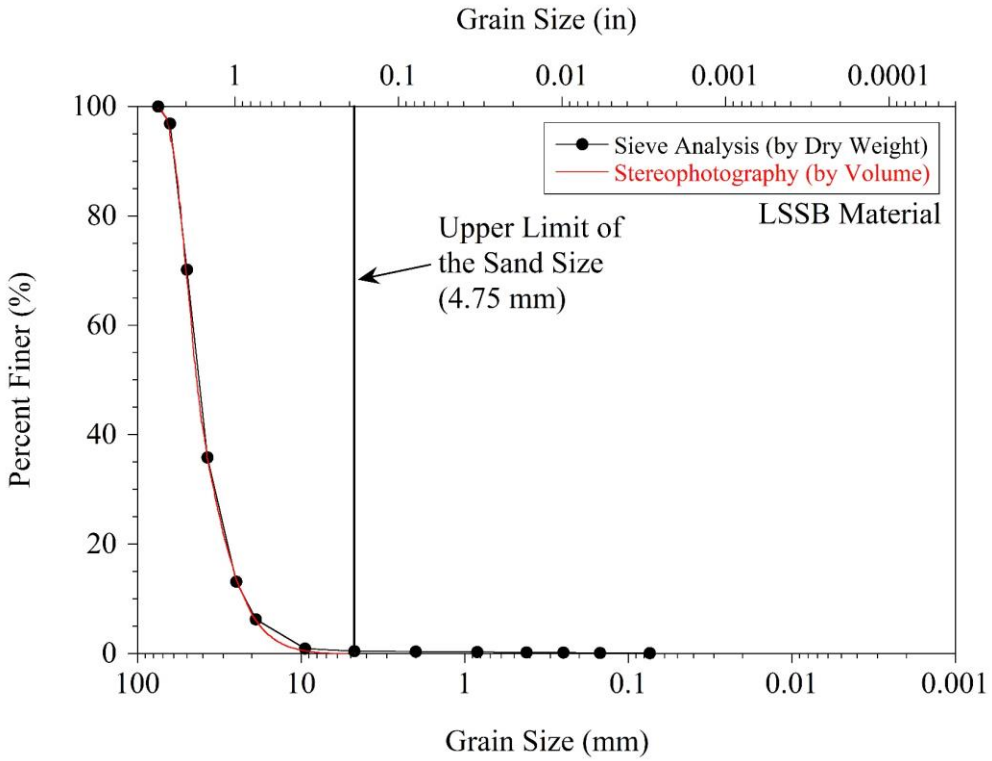

Figure 5.6. Gradations of LSSB material determined by sieve analysis and stereophotography

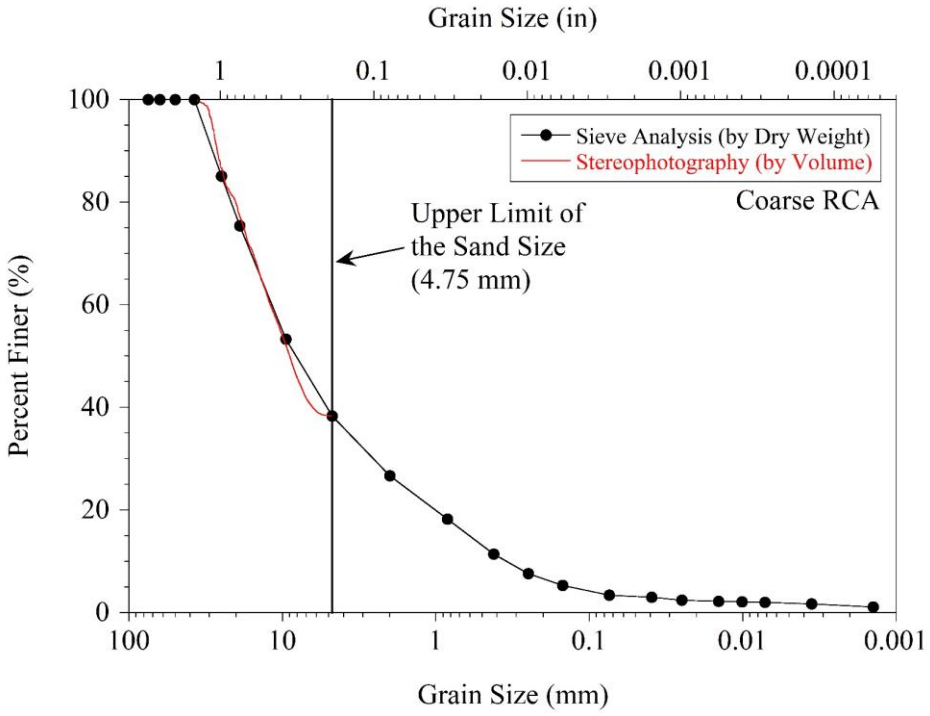

Figure 5.7. Gradations of Coarse RCA determined by sieve analysis and stereophotography

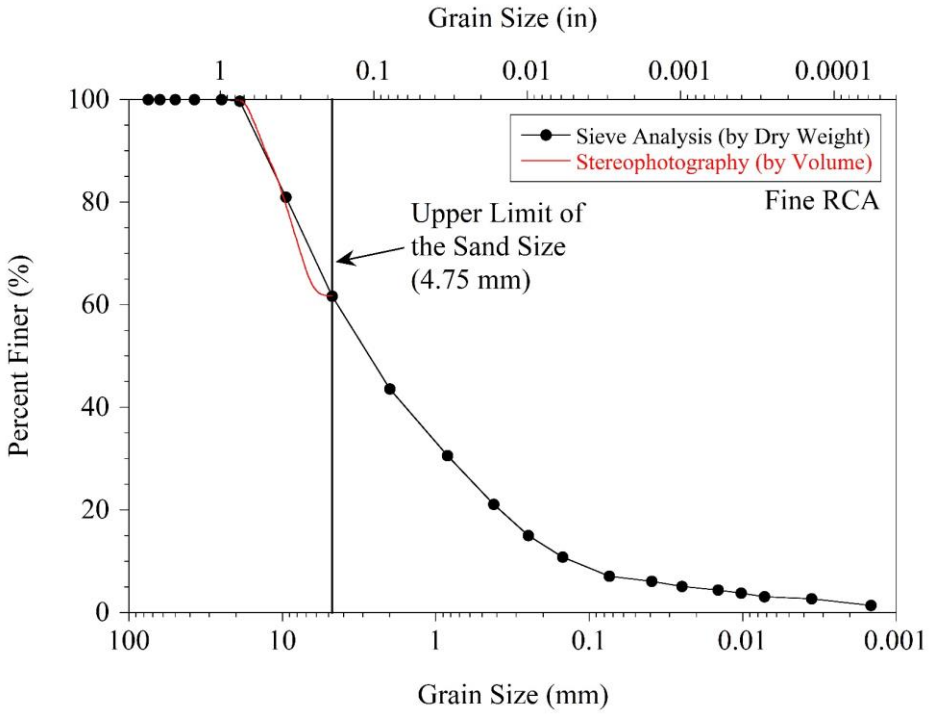

Figure 5.8. Gradations of Fine RCA determined by sieve analysis and stereophotography

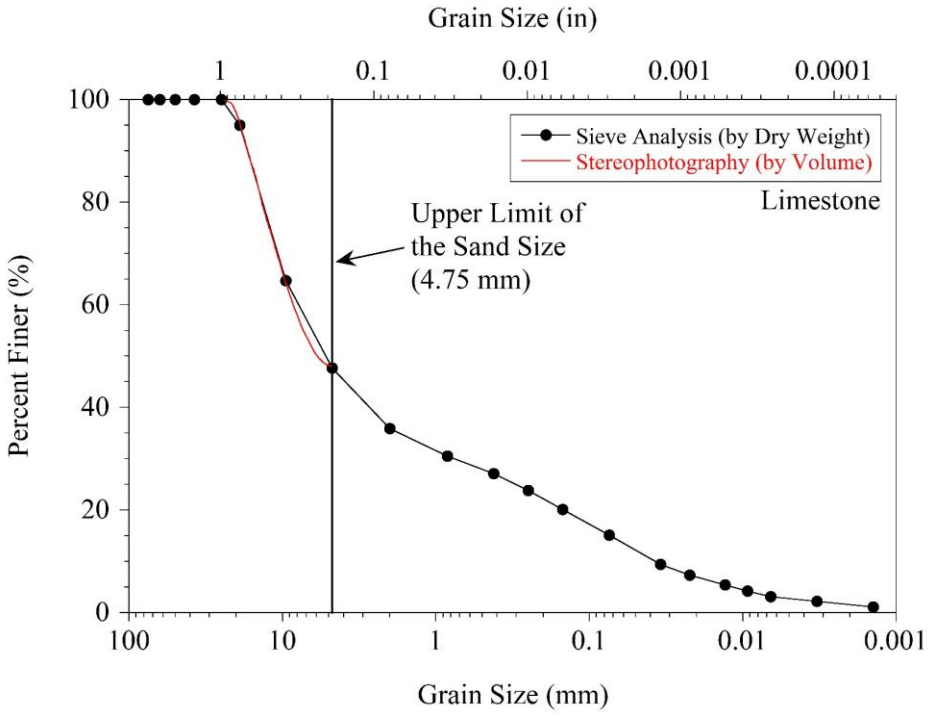

Figure 5.9. Gradations of Limestone determined by sieve analysis and stereophotography

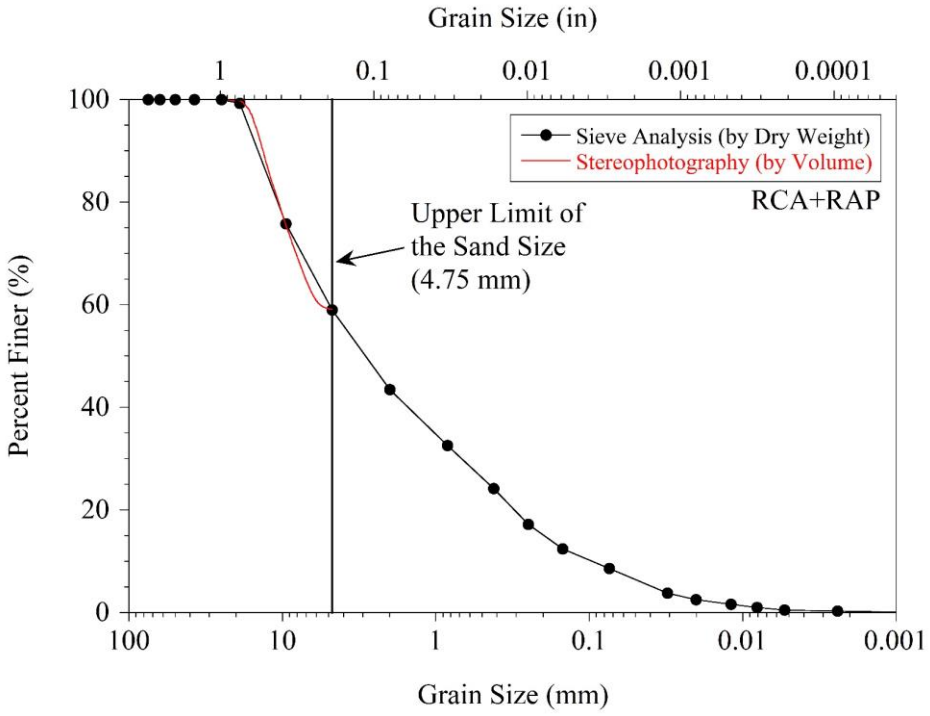

Figure 5.10. Gradations of RCA+RAP determined by sieve analysis and stereophotography

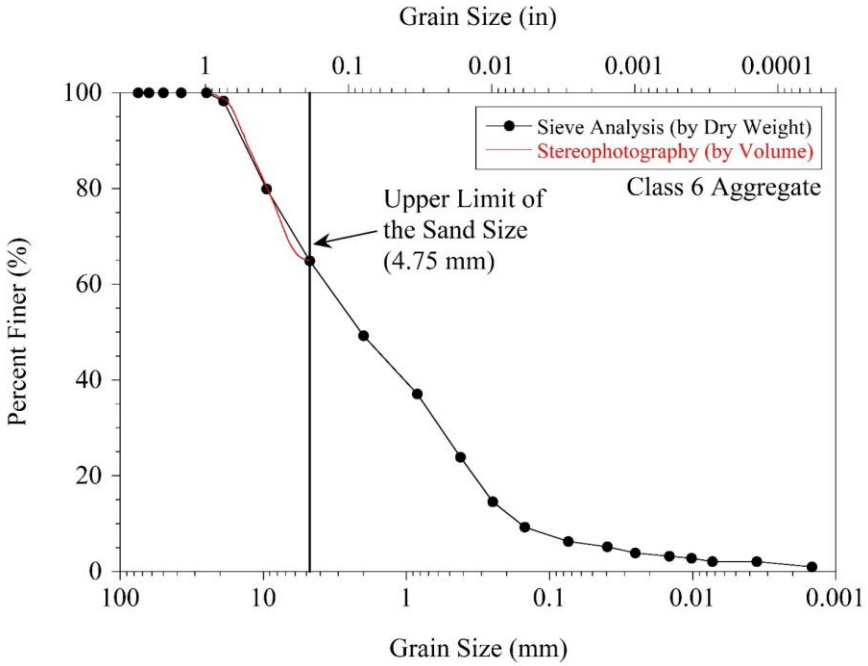

Figure 5.11. Gradations of Class 6 Aggregate determined by sieve analysis and stereophotography

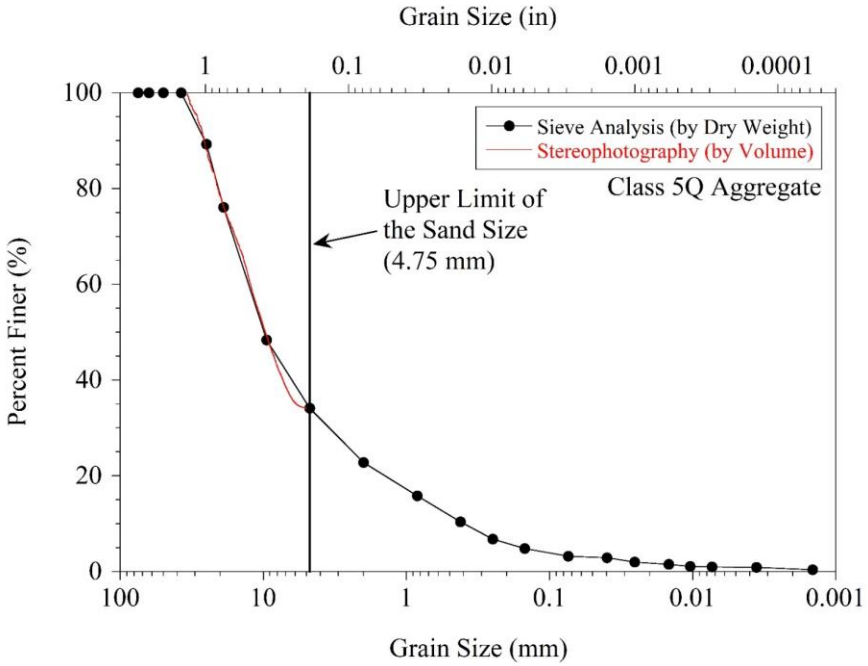

Figure 5.12. Gradations of Class 5Q Aggregate determined by sieve analysis and stereophotography

5.3. Particle Shape Analysis

Particle shape characteristics of the materials were also determined by stereophotography. The Matlab code provided eight different parameters: area sphericity, diameter sphericity, circle ratio

sphericity, perimeter sphericity, width-to-length ratio sphericity, circularity, convexity, and roundness. Each parameter is summarized in Table 5.1. Zheng and Hryciw (2015) stated that the width-to-length ratio sphericity (S_{WL}), defined by Krumbein and Sloss (1951) [Figure 5.13(a)], is the most useful approach to evaluate sphericity and yields the widest range of sphericity values (between 0 and 1). In addition, S_{WL} parameter does not depend on particle roundness, defined by Wadell (1932, 1933, 1935) [Figure 5.13(b)] (Zheng and Hryciw 2015; Hryciw et al. 2016). The Krumbein-Sloss chart (Figure 5.14) is a very well-known chart, which combines S_{WL} and roundness parameters (Zheng and Hryciw 2015; Kim et al. 2019). Therefore, in this study, S_{WL} and roundness (R) parameters were used to evaluate the particle shape characteristics.

Table 5.1. Particle shape parameters determined by stereophotography

Parameter	Formula	Description	Reference
Area Sphericity	$S_A = \frac{A}{A_{cir}}$	The ratio of the area of the particle (A) to the area of the smallest circumscribing circle (A_{cir}).	Riley (1941)
Diameter Sphericity	$S_D = \frac{D_e}{D_{cir}}$	The ratio of the diameter of a circle having the same area as the original particle (D_e) to the diameter of the minimum circumscribing circle (D_{cir}).	Wadell (1935)
Circle Ratio Sphericity	$S_C = \frac{D_{ins}}{D_{cir}}$	The ratio of the diameter of the largest inscribed circle of the particle (D_{ins}) to the smallest circumscribing circle of the particle (D_{cir}).	Santamarina and Cho (2000)
Perimeter Sphericity	$S_P = \frac{P_e}{P}$	The ratio of the perimeter of the circle having the same area as the particle (P_e) to the real perimeter of the particle (P).	Kuo and Freeman (2000)
Width-to-Length Ratio Sphericity (Aspect Ratio, Elongation)	$S_{WL} = \frac{d_2}{d_1}$	The ratio of the width of the particle (d_2) to the length of the particle (d_1).	Krumbein and Sloss (1951)
Circularity	$C = \frac{4\pi A}{P^2}$	The ratio of the area of the particle (A) to the area of the circle having the same perimeter as the particle ($P^2/4\pi$).	ISO (2008)
Convexity (Solidity)	$C_x = \frac{A}{A_c}$	The ratio of the area of the particle (A) to the area of the minimum convex boundary circumscribing the particle (A_c).	Mora and Kwan (2000)
Roundness (Angularity)	$R = \frac{\sum_{i=1}^{N} r_i / N}{r_{ins}}$	The ratio of the average radius of corner circles of the particles (r_i is the radius of i-th corner and N is the number of corners) to the radius of the maximum inscribed circle (r_{ins}).	Wadell (1932, 1933, and 1935)

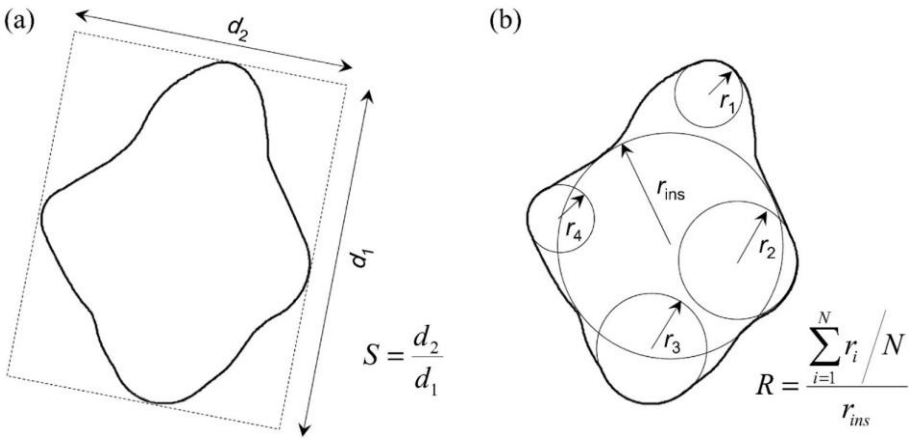

Figure 5.13. Definitions of (a) width-to-length ratio sphericity (Krumbein and Sloss 1951; Hryciw et al. 2016) and (b) roundness (Wadell 1932, 1933, and 1935)

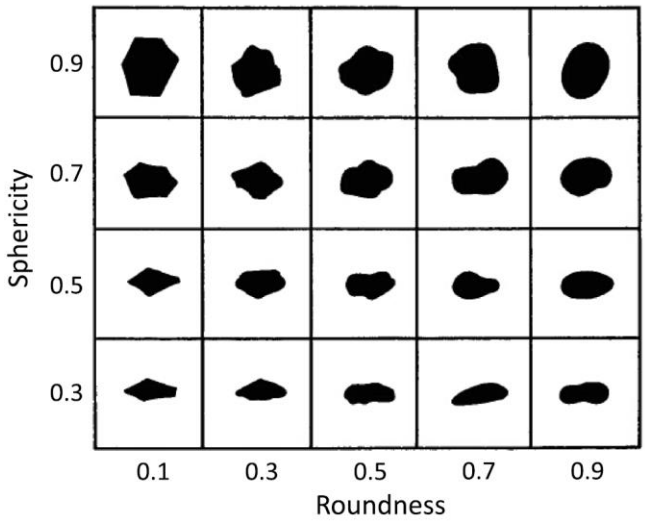

Figure 5.14. Krumbein-Sloss chart (Krumbein and Sloss 1951; Hryciw et al. 2016)

Particle distributions based on their width-to-length ratio sphericity and roundness values are provided in Figures 5.15 and 5.16, respectively. Summaries of the width-to-length ratio sphericity and roundness distributions are provided in Tables 5.2 and 5.3, respectively. For the distributions, the number of particles was considered instead of the volume of particles. If the volume of particles was considered, particle size would affect the particle shape distributions (Li et al. 2017). To avoid this, the number of particles was used in order to evaluate the distributions.

For all materials, there was no particle exhibiting an S_{WL} value smaller than 0.3 (Figure 5.15 and Table 5.2). Base layer aggregates exhibited similar S_{WL} distributions (Figure 5.15). However, LSSB particles were less spherical than base layer aggregates overall (Figure 5.15). In terms of roundness, none of the particles exhibited roundness value at around 0.1 (Figure 5.16 and Table 5.3). While base layer aggregates yielded similar roundness distributions, the roundness distribution of LSSB particles was considerably different from those of base layer aggregates (Figure 5.16). LSSB particles were relatively less rounded (more angular) than base layer aggregates (Figure 5.16).

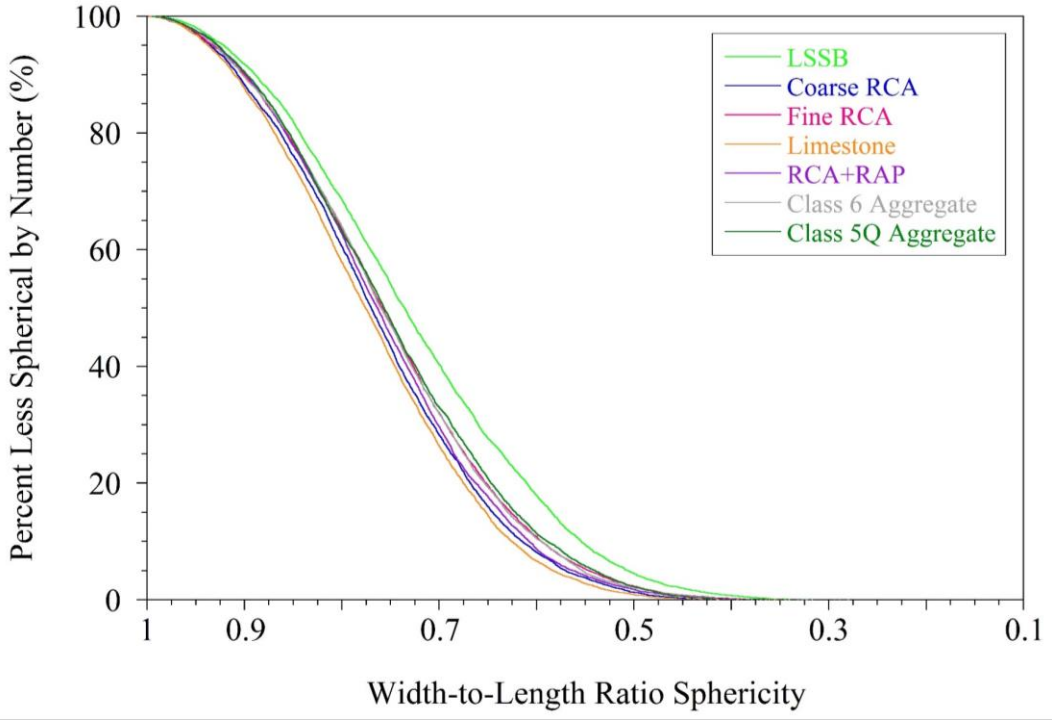

Figure 5.15. Width-to-length ratio sphericity distributions of the materials determined by stereophotography

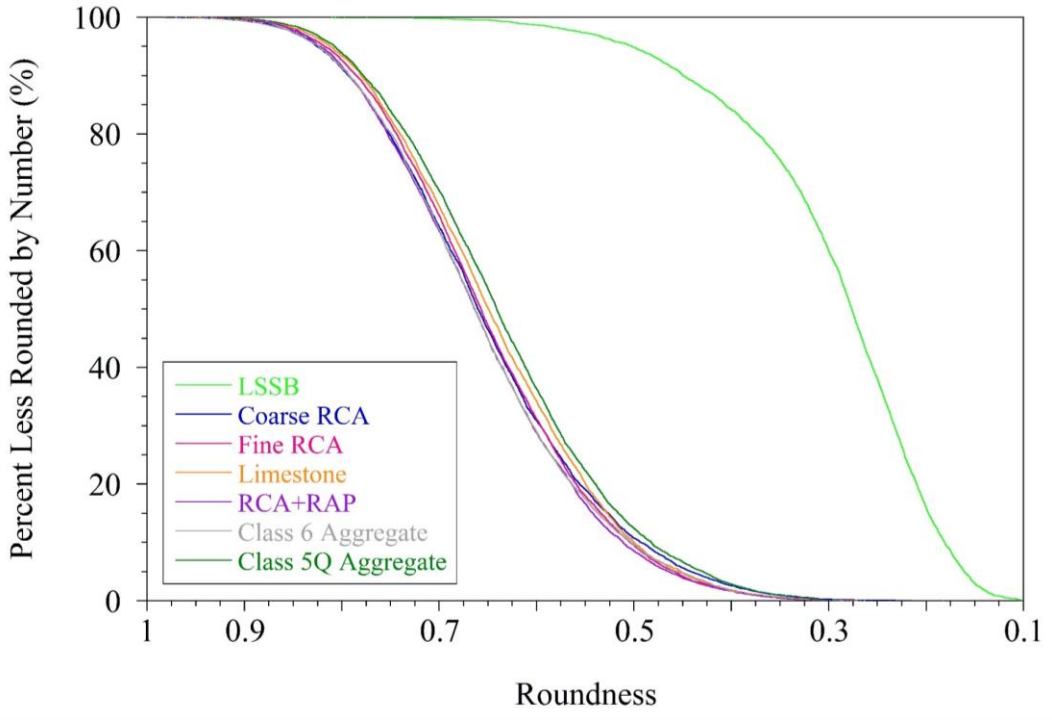

Figure 5.16. Roundness distributions of the materials determined by stereophotography

Table 5.2. Summary of the width-to-length ratio sphericity distributions

Material	Percent Less Spherical by Number (%)				
	0.9	**0.7**	**0.5**	**0.3**	**0.1**
LSSB	92	40	4.5	0	0
Coarse RCA	88	28	1	0	0
Fine RCA	90	32	2.5	0	0
Limestone	88	26	1	0	0
RCA+RAP	90.5	30	2	0	0
Class 6 Aggregate	90	32	2	0	0
Class 5Q Aggregate	90.5	33	2	0	0

Table 5.3. Summary of the roundness distributions

Material	Percent Less Rounded by Number (%)				
	0.9	**0.7**	**0.5**	**0.3**	**0.1**
LSSB	100	100	95	60	0
Coarse RCA	99.5	64	11	0.5	0
Fine RCA	99.5	66	9.5	0	0
Limestone	99.5	67.5	10	0	0
RCA+RAP	100	63.5	8.5	0	0
Class 6 Aggregate	99	63.5	10	0	0
Class 5Q Aggregate	100	70	12.5	0	0

6. GYRATORY COMPACTION AND ABRASION

Degradation (or abrasion) of aggregates used in aggregate base layers can significantly affect the engineering properties of the pavement systems (Zeghal 2009). Due to degradation, aggregates become finer and reduction in aggregate sizes may decrease permeability and freeze-thaw (F-T) durability (Cho et al. 2006; Vallejo et al. 2006; White and Vennapusa 2014). Gradation, mineralogy, morphology, and loading conditions affect the degradation of aggregates (Li et al. 2017). Los Angeles (LA) abrasion (ASTM C131) and Micro-Deval tests (ASTM D6928) are the most commonly used tests to evaluate the degradation of aggregates. Specimens must be prepared at standard gradations to be tested by these two methods. However, each aggregate has a different gradation and the gradation affects the engineering properties of aggregates significantly (shear strength, stiffness, permeability, etc.) (Cosentino et al. 2003; Tan et al. 2014; Zheng and Hryciw 2014, 2017). Preparing aggregate specimens at standard gradations cannot represent the actual behavior of aggregates in the field; therefore, aggregates should be tested at their own gradations (Li et al. 2017). In addition, it is stated by Li et al. (2017) that the LA abrasion and Micro-Deval tests do not simulate the field loading conditions.

To overcome such problems, the Gyratory Abrasion and Image Analysis (GAIA) method was developed by Li et al. (2017). Gyratory compaction is generally used for testing asphalt materials (Harman 2002). In addition, it is also used for soils and aggregates as an alternative to Proctor

compaction (Kim et al. 2007; Li et al. 2015). Previously, the 2D image analysis was used by Li et al. (2017). However, in this study, stereophotography, which is the previously described 3D image processing technique, was performed. Changes in the particle size and shape characteristics of aggregates due to gyratory compaction effort were evaluated by the image analysis. In the GAIA method, aggregates were tested at their actual gradations.

6.1. Test Method

The GAIA method was performed on Coarse RCA, Fine RCA, Limestone, RCA+RAP, Class 6 Aggregate, and Class 5Q Aggregate. First, sieve analysis was performed on each material and the particles retained on the sieves (1 in, 3/4 in, 3/8 in, No. 4, No. 10, No. 20, No. 40, No. 60, No. 100, and No. 200 sieves) were separated, washed (particles passing No. 200 sieve were not washed), and dried in an oven at 110°C for 24 hours. The weight of each specimen was determined to be 4500 g and the required amount of each particle size (separated by the sieves) was calculated based on the original gradation of the material (Figure 3.1). Two particle fractions were kept in two different sealed bags: one for the particles larger than No. 4 sieve (4.75 mm) and another one for the particles finer than No. 4 sieve [Figure 6.1(a)]. Three specimens were prepared for each material (18 specimens in total from six different materials). Then, stereophotography, as described previously, was performed on the particles larger than No. 4 sieve (4.75 mm). After the completion of the image analysis, the two sealed bags were mixed in a pan prior to gyratory compaction [Figure 6.1(b)].

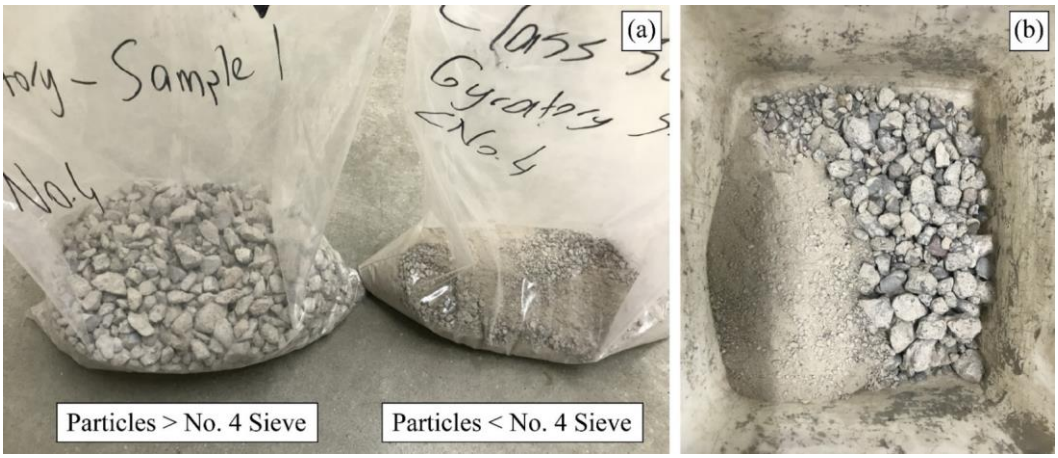

Figure 6.1. (a) Particle groups stored in different sealed bags and (b) mixing all particle groups prior to gyratory compaction

The gyratory compactor, used in this study, is shown in Figure 6.2. The information regarding the specimen sizes and the operation parameters is summarized in Table 6.1 (ASTM D6925). For three specimens from the same material, the first, the second, and the third specimen were subjected to 100, 300, and 500 gyrations, respectively. 100 and 300 gyrations were applied in a single test for the first and the second specimens. In fact, for the second specimen, 299 gyrations were applied since it was the maximum number of gyrations that could be applied in a single test. However, the number was rounded to 300 for simplicity. To apply 500 gyrations for the third specimen, two consecutive 250-gyration tests were applied. Examples of the particles crushed due to the gyratory compaction effort are provided in Figure 6.3.

After compaction, similar sieving, separating, washing, and drying operations were performed on the compacted materials. Stereophotography, described previously, was performed on the particles retained on No. 4 sieve (4.75 mm). Then, the particle size and shape characteristics of the particles larger than No. 4 sieve before and after the gyratory compaction effort were compared.

Figure 6.2. Picture of the gyratory compactor used in this study

Table 6.1. Specimen sizes and operation parameters of the gyratory compactor

Parameter	Value
Compaction Mold Diameter [inch (mm)]	6 (150)
Specimen Height [inch (mm)]	6 - 7.25 (150 - 185)
Vertical Applied Pressure [psf (kPa)]	12,530 (600)
Number of Gyrations	100, 300[a], 500[b]
Angle of Gyration (°)	1.25 ± 0.02
Frequency of Gyration (gyrations/min)	30 ± 0.5
Number of Dwell Gyrations	2

[a]In fact, 299 gyrations (maximum number of gyrations that can be applied per test) were applied. However, the number is rounded to 300 for simplicity. [b]Applied in two consecutive tests with 250 gyrations each.

Figure 6.3. Examples of crushed particles after gyratory compaction

6.2. Compaction Analysis

Height changes of the specimens during the gyratory compaction were recorded at each gyration by the compactor's integral displacement transducer. From the recorded heights and known diameter of the compaction mold (6 inches), volume changes of the specimens during the compaction were calculated. Then, based on the specimen weight and volume changes during the compaction, changes in the dry unit weight (γ_{dry}) of the specimens were calculated and shown in Figure 6.4.

As expected, the γ_{dry} of each specimen increased during gyratory compaction. Applying 100 and 300 gyrations yielded uninterrupted curves showing the increase in the dry unit weight of the specimens. On the other hand, applying 500 gyrations yielded interrupted curves. As stated previously, two sets of 250-gyration tests were performed to be able to apply 500 gyrations in total. At the end of the first set of the 250 gyrations, the test stopped automatically and was restarted manually. When the test stopped, the gyratory compactor released the vertical pressure (12,530 psf) and applied two dwell gyrations in order to zero the angle of gyration (1.25 ± 0.02°). This caused some disturbance of the data for 500 gyrations (Li et al. 2017). However, in Figure 6.4, the disturbance was eliminated, and dashed lines were added between the end of the first 250-gyration stage and the point, where the dry unit weight values went back to the actual trend.

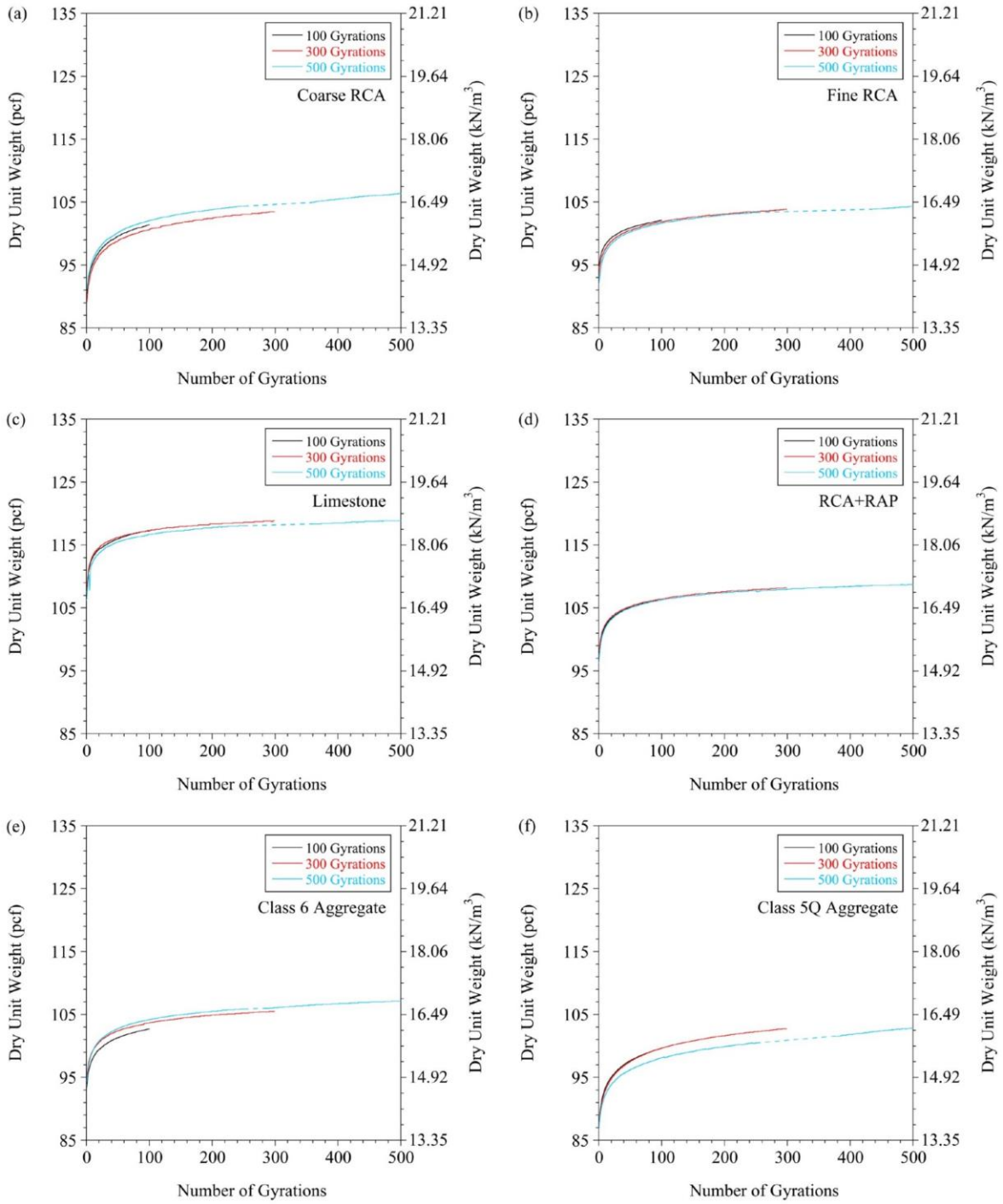

Figure 6.4. Changes of dry unit weight of the specimens during the gyratory compaction (a) Coarse RCA, (b) Fine RCA, (c) Limestone, (d) RCA+RAP, (e) Class 6 Aggregate, (f) Class 5Q Aggregate

6.3. Abrasion on the Particle Size

The gradations of the materials before and after the gyratory compaction (after 100, 300, and 500 gyrations) are shown in Figures 6.5, 6.6, 6.7, 6.8, 6.9, and 6.10 for Coarse RCA, Fine RCA,

Limestone, RCA+RAP, Class 6 Aggregate, and Class 5Q Aggregate, respectively. To evaluate the degradation during compaction, breakage potential (B_p), total breakage (B_t), and relative breakage (B_r) parameters, described by Hardin (1985), were used. B_p is defined as the area between the initial gradation curve (before compaction) and the line, which defines the upper limit of the silt size (0.075 mm) (Hardin 1985) (Figure 6.11). B_t is defined as the area between the initial (before compaction) and the final (after compaction) gradation curves (Hardin 1985) (Figure 6.11). For B_p and B_t, the areas are the relative areas compared to the unit area, which is the area of one log cycle (Hardin 1985). B_r is the ratio between the B_t and B_p (Figure 6.11). B_p, B_t, and B_r of the materials are summarized in Figures 6.12, 6.13, and 6.14, respectively.

Coarse RCA and Class 5Q Aggregates exhibited higher B_p than the other materials (1.81 and 1.86, respectively) (Figure 6.12). In fact, the highest B_p was observed with Class 5Q Aggregate (1.86) (Figure 6.12). According to these results, Coarse RCA and Class 5Q Aggregate were expected to exhibit higher degradation compared to other materials. This behavior could be related to the coarser gradations of these two materials. Coarse RCA and Class 5Q Aggregate consisted of 96.6% (61.7% gravel and 34.9% sand) and 96.8% (65.9% gravel and 30.9% sand) gravel- and sand-size particles, respectively (Figure 3.1. and Table 3.1). These amounts were higher than other materials (Table 3.1). According to Hardin (1985), the larger the particle size the higher the B_p. This is because less stress is required to break up the larger particles compared to the finer particles (Hardin 1985). In descending order, B_p values of 1.47, 1.40, 1.40, and 1.35 were determined for Limestone, Fine RCA, RCA+RAP, and Class 6 Aggregate (Figure 6.12).

Coarse RCA and Class 5Q Aggregate showed larger B_t than the other materials (from 0.06 to 0.12 for Coarse RCA and from 0.09 to 0.15 for Class 5Q Aggregate) for each number of gyrations (Figure 6.13). Class 5Q Aggregate actually exhibited the highest B_t values (from 0.09 to 0.15) (Figure 6.13). This means that Class 5Q Aggregate experienced the highest degradation, which was followed by Coarse RCA, for each number of gyrations. This result was compatible with the B_p values, explained previously (Figure 6.12). Li et al. (2017) also observed that there was a linear relationship between the initial gravel content of the materials, used in that study, and B_t. While Fine RCA's B_p value (1.40) was lower than and equal to those of Limestone (1.47) and RCA+RAP (1.40) (Figure 6.12), respectively, it exhibited higher B_t (from 0.04 to 0.07) than Limestone (from 0.02 to 0.04) and RCA+RAP (from 0.03 to 0.04) for each number of gyrations (Figure 6.13). In the literature, it is stated that an increase in the residual mortar content can yield an increase in aggregate degradation because of the crushing and degradation of the porous mortar (Juan and Gutiérrez 2009; Butler et al. 2011; Bhasya and Bharatkumar 2018). In addition, Coarse RCA and Class 5Q Aggregate exhibited higher degradation because of not only their coarser gradations but also their residual mortar content. Both Coarse RCA and Class 5Q Aggregates may have gravel size cemented aggregates, which could break down right away under pressure. Thus, higher B_t values could be observed for these two materials. B_r values of the materials (Figure 6.14) exhibited a similar trend as observed for the B_t values (Figure 6.13).

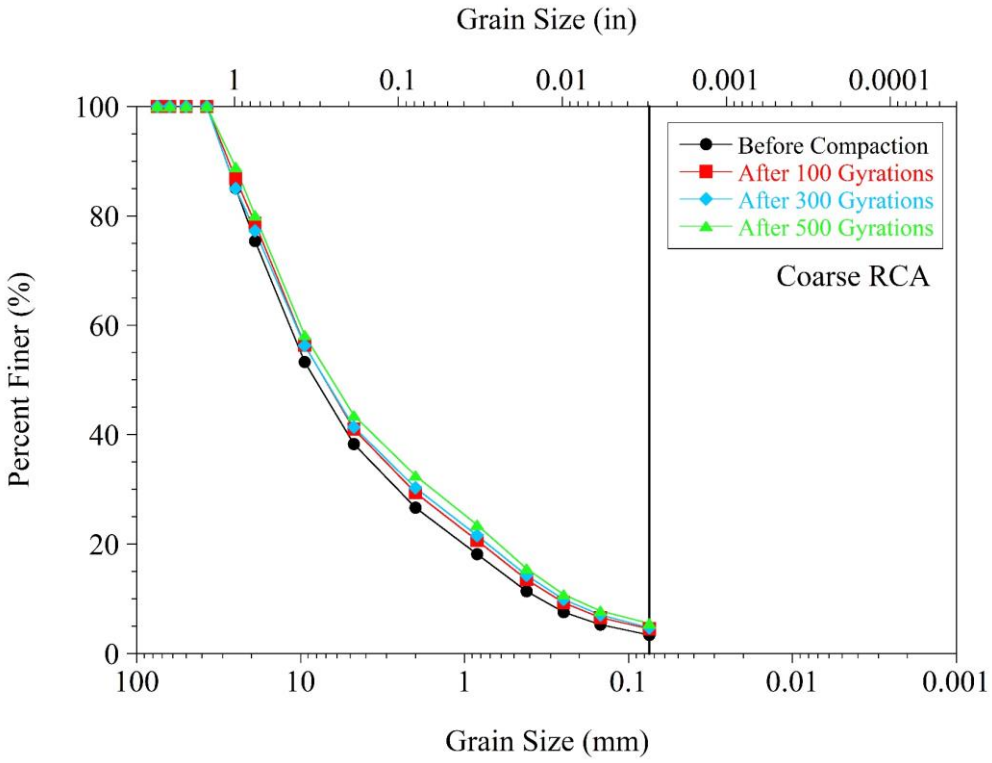

Figure 6.5. Gradations of Coarse RCA before and after the gyratory compaction

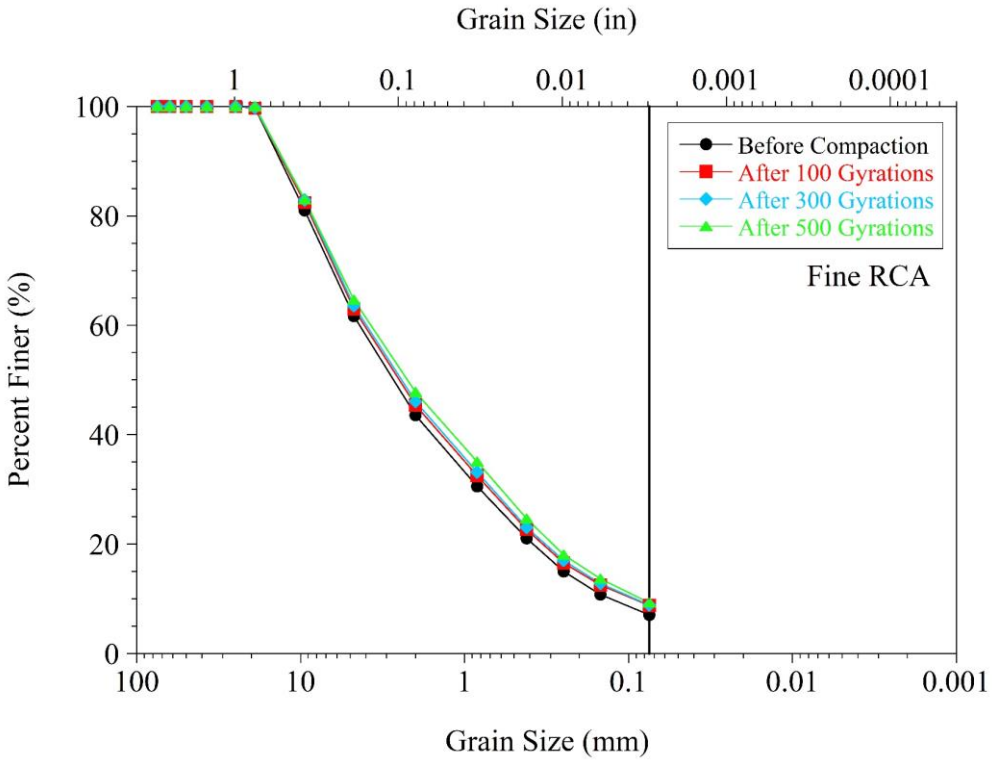

Figure 6.6. Gradations of Fine RCA before and after the gyratory compaction

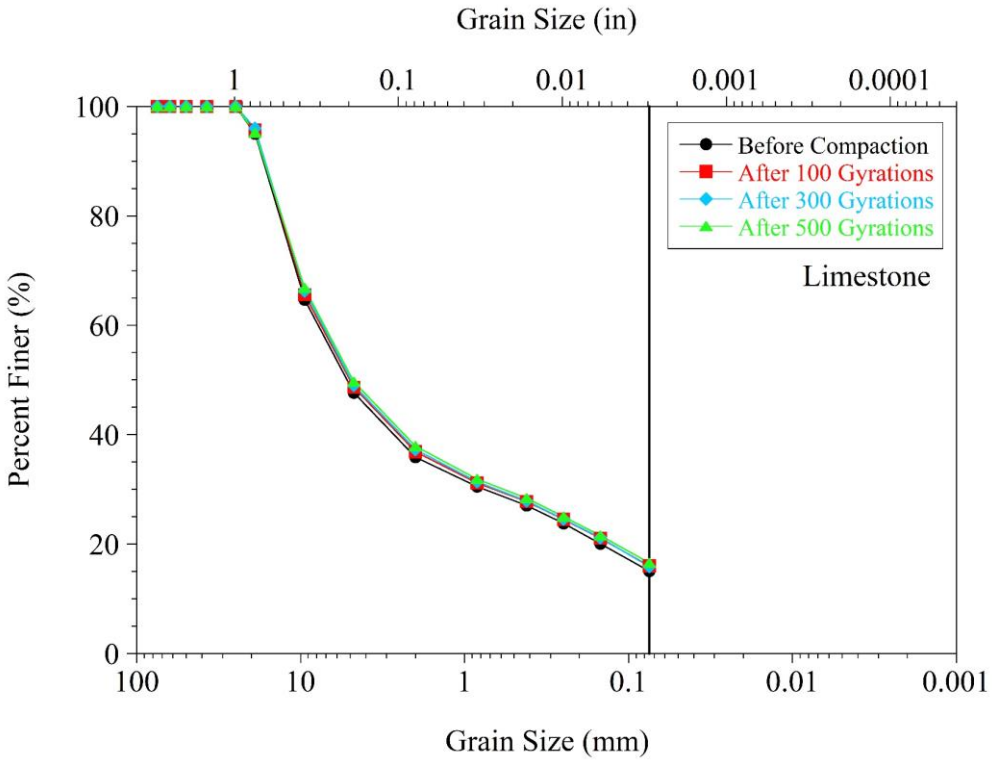

Figure 6.7. Gradations of Limestone before and after the gyratory compaction

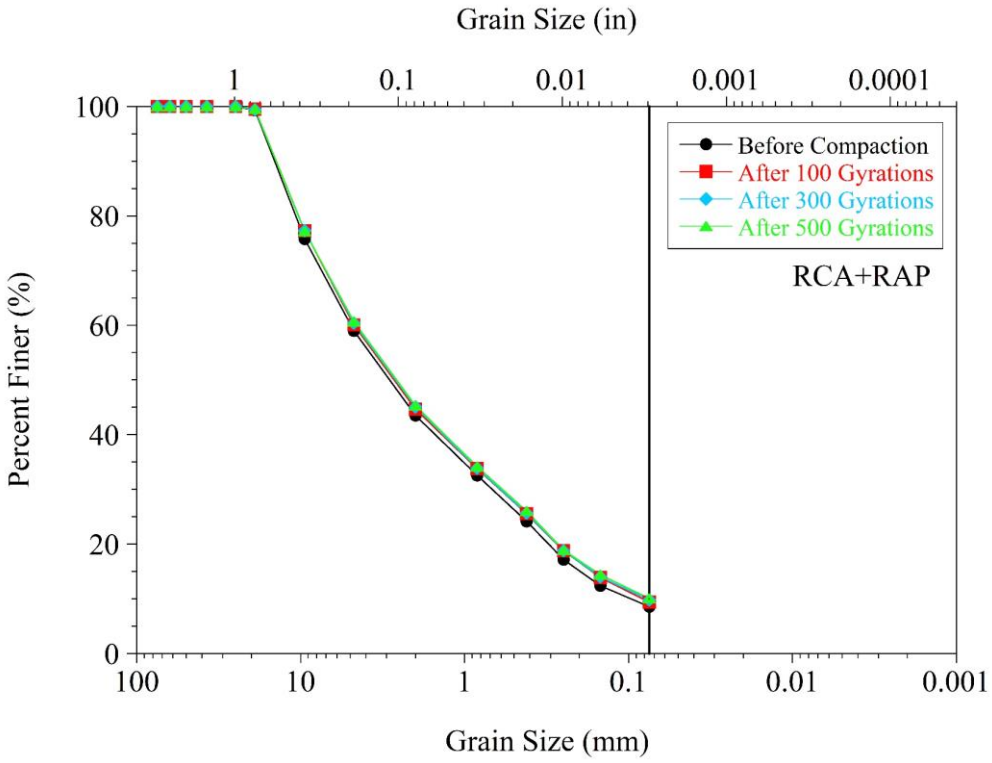

Figure 6.8. Gradations of RCA+RAP before and after the gyratory compaction

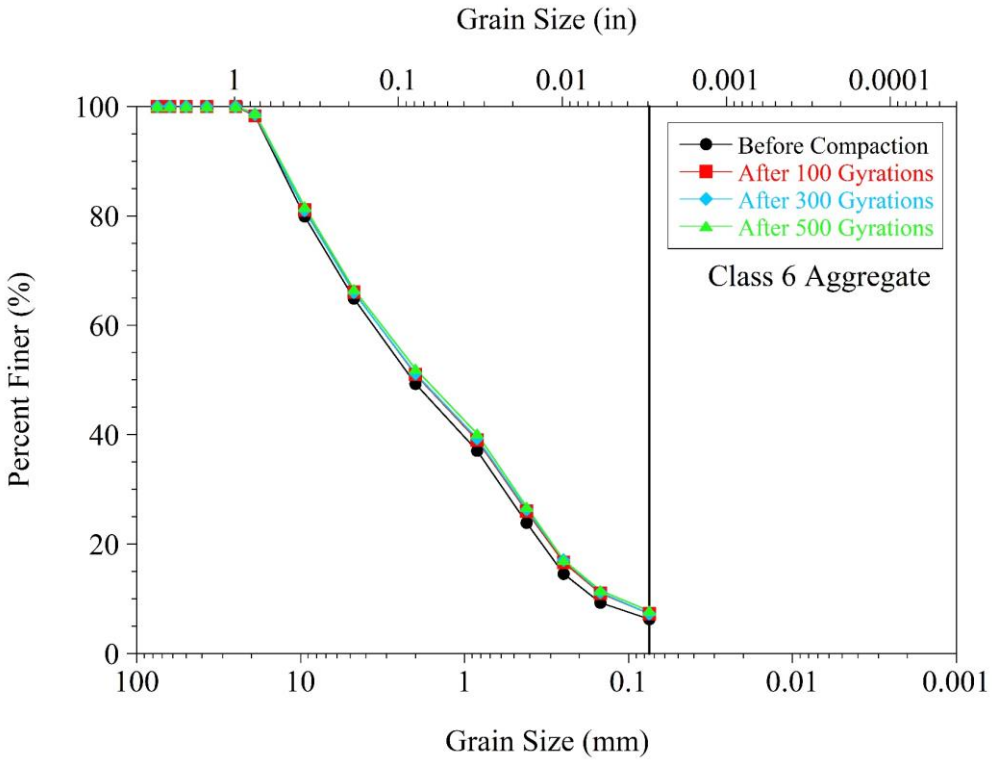

Figure 6.9. Gradations of Class 6 Aggregate before and after the gyratory compaction

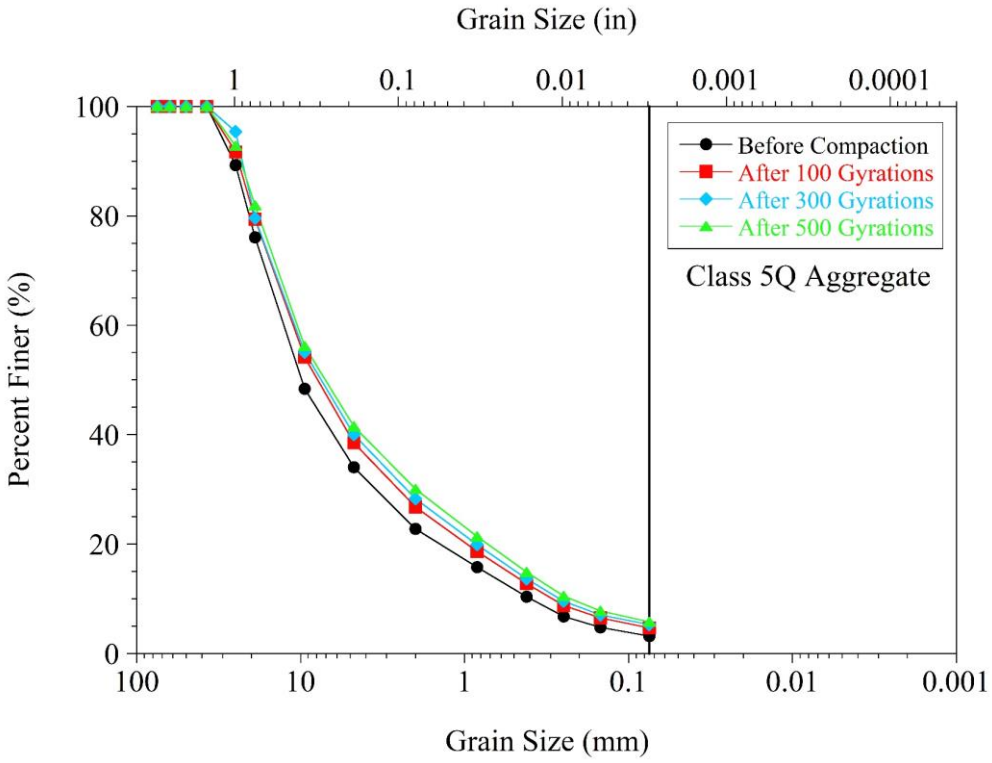

Figure 6.10. Gradations of Class 5Q Aggregate before and after the gyratory compaction

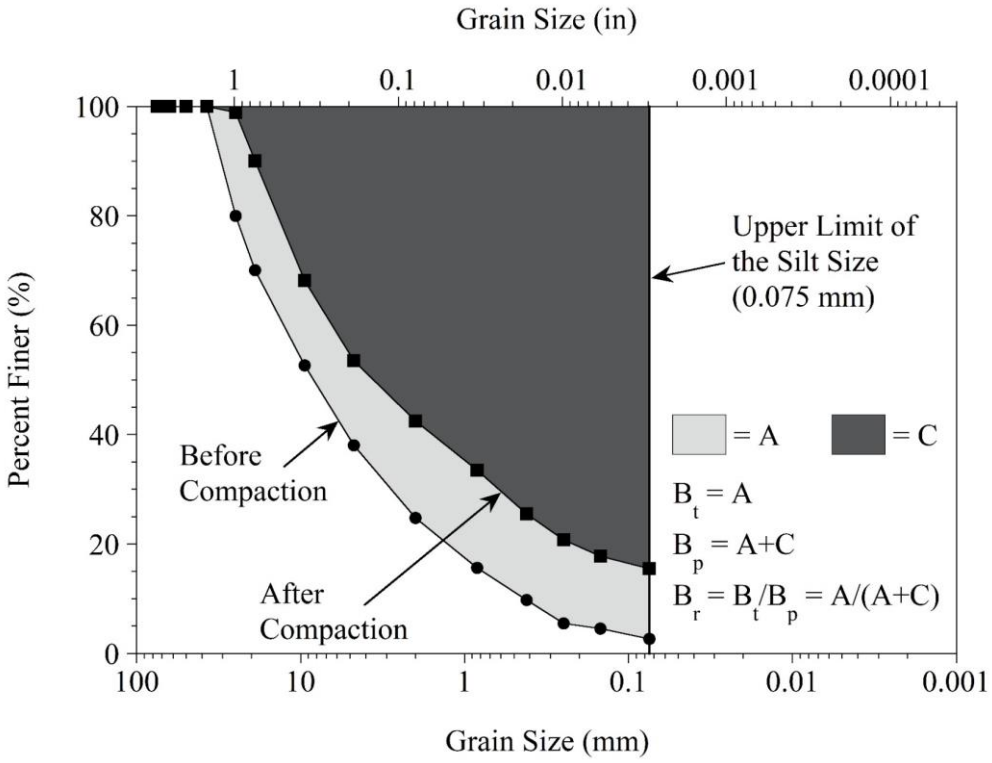

Figure 6.11. Hardin's concept to evaluate the degradation of aggregates

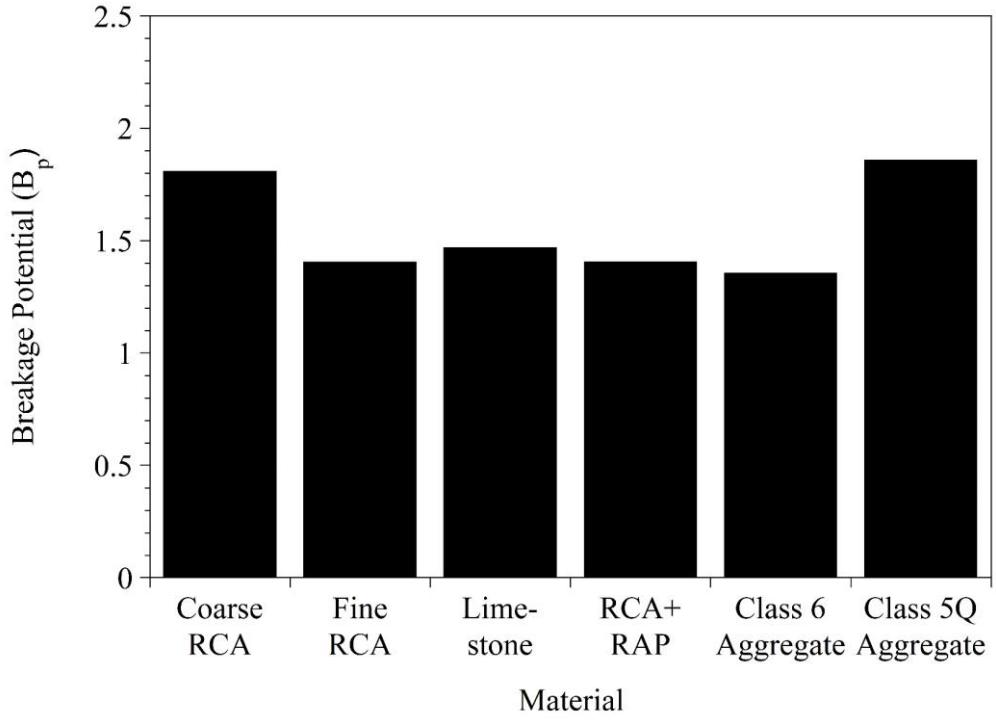

Figure 6.12. Breakage potential (B_p) of the materials

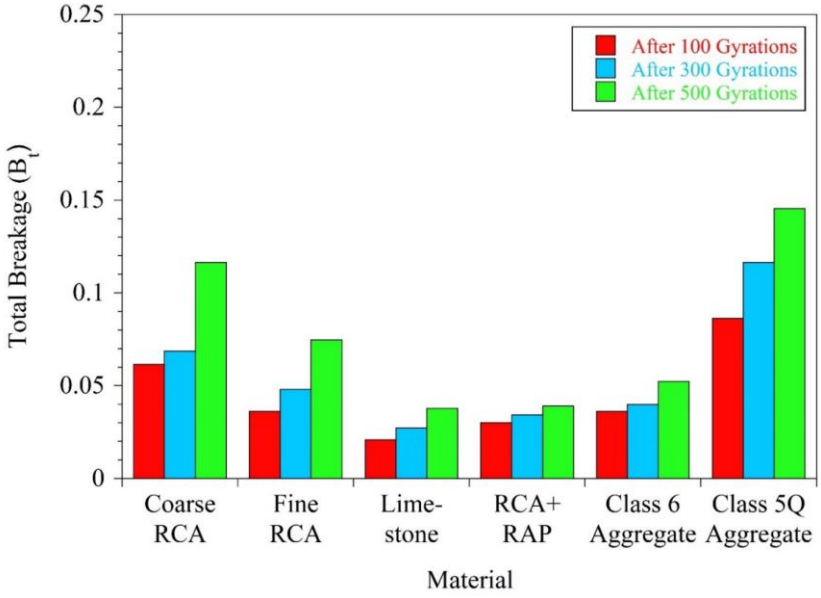

Figure 6.13. Total breakage (B_t) of the materials

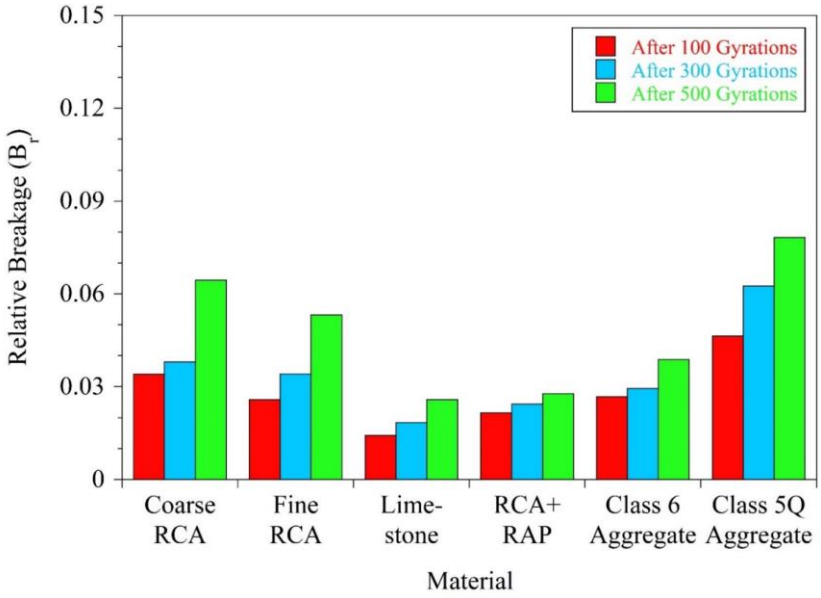

Figure 6.14. Relative breakage (B_r) of the materials

6.4. Abrasion on the Particle Shape

The width-to-length ratio sphericity and roundness of the materials (Table 5.1 and Figure 5.13) before and after compaction were evaluated. Figures 6.15 and 6.16 provide examples of the changes in the width-to-length ratio sphericity and roundness of Coarse RCA due to gyratory compaction, respectively. Overall, it was concluded that an increase in the gyration number yielded higher changes in the particle shapes.

Summaries of the test results are provided in Figures 6.17, 6.18, and 6.19 for 100, 300, and 500 gyrations, respectively. Box plots were used for the evaluation of the abrasion on the particle shape.

Similar to the results obtained by Li et al. (2017), the materials became slightly more spherical and rounded due to abrasion caused by gyratory compaction.

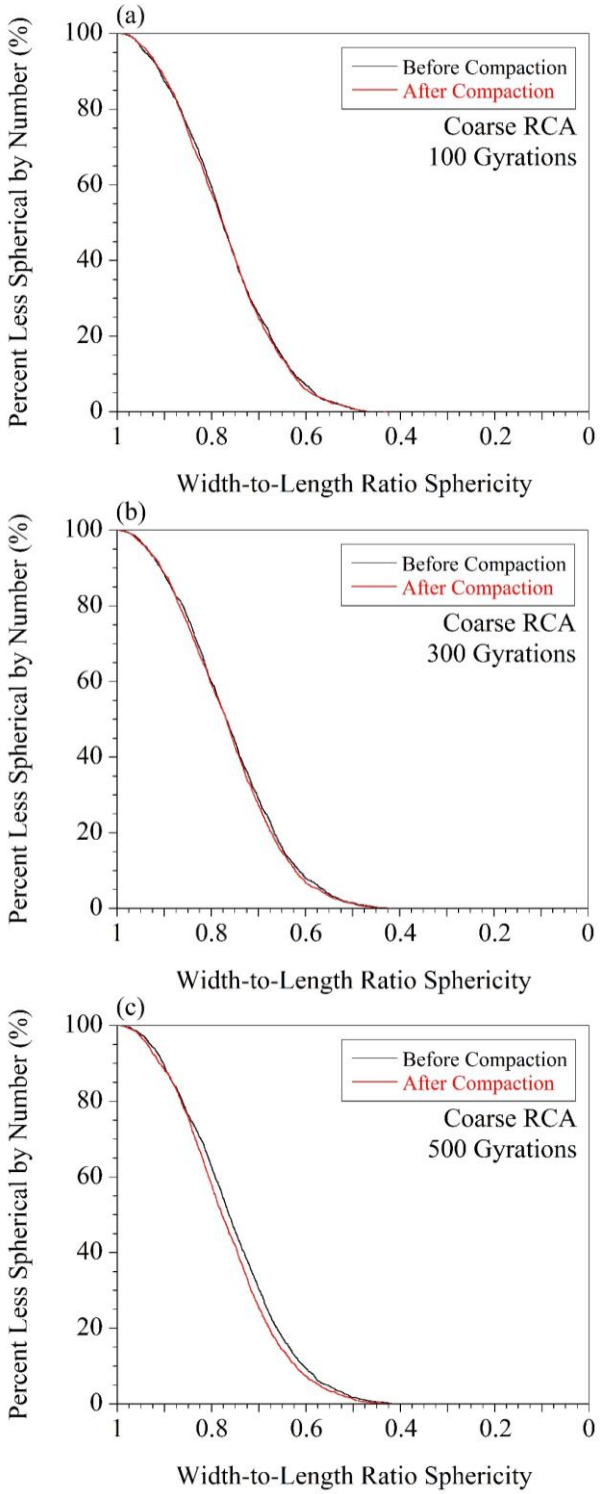

Figure 6.15. Abrasion on the width-to-length ratio sphericity of Coarse RCA after (a) 100 gyrations, (b) 300 gyration, and (c) 500 gyrations

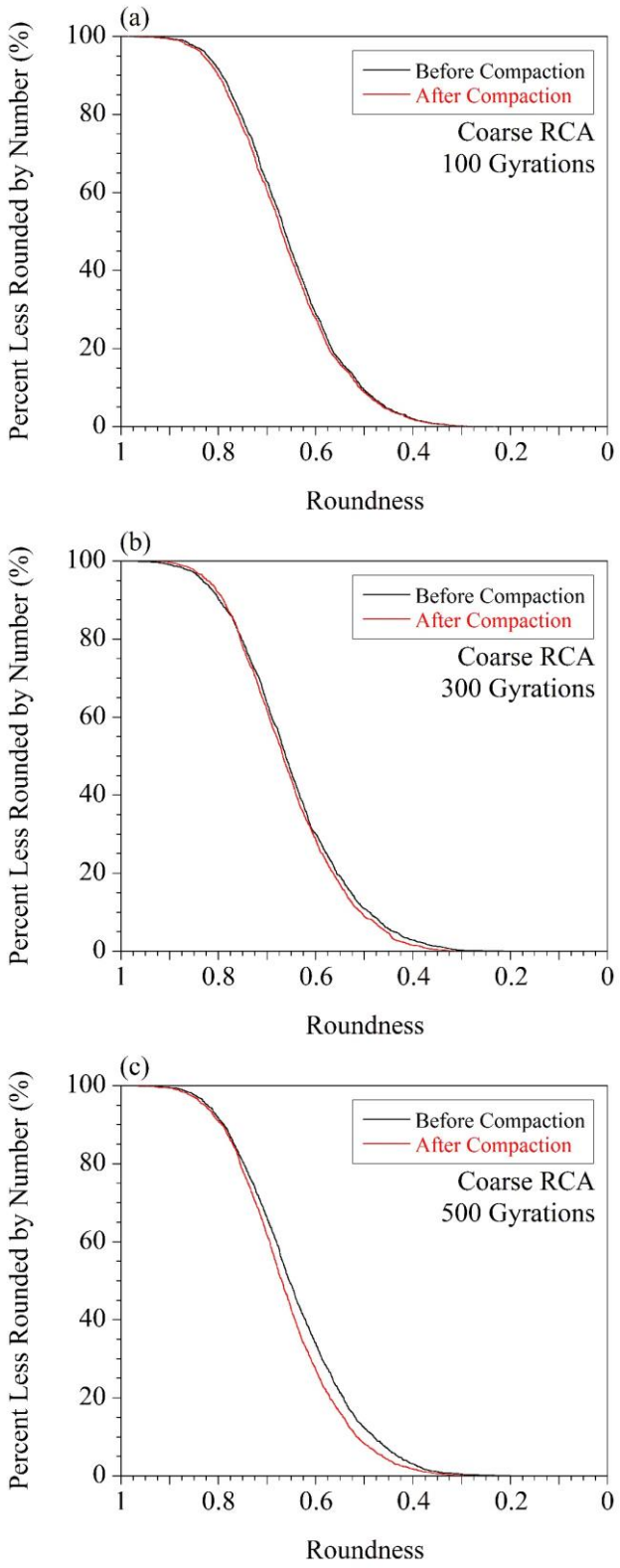

Figure 6.16. Abrasion on the roundness of Coarse RCA after (a) 100 gyrations, (b) 300 gyration, and (c) 500 gyrations

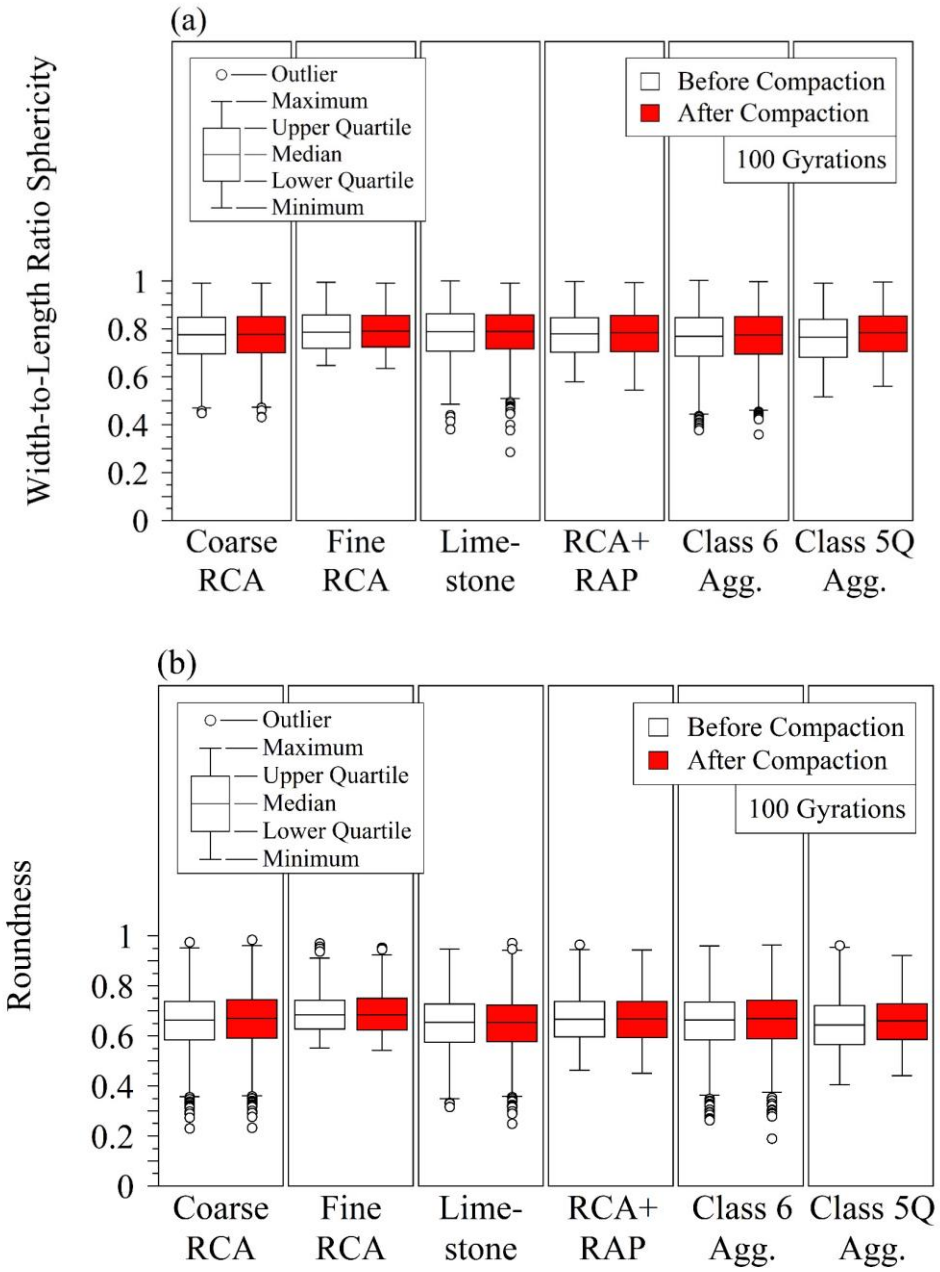

Figure 6.17. Abrasion on the particle shape after 100 gyrations in terms of (a) width-to-length ratio sphericity and (b) roundness

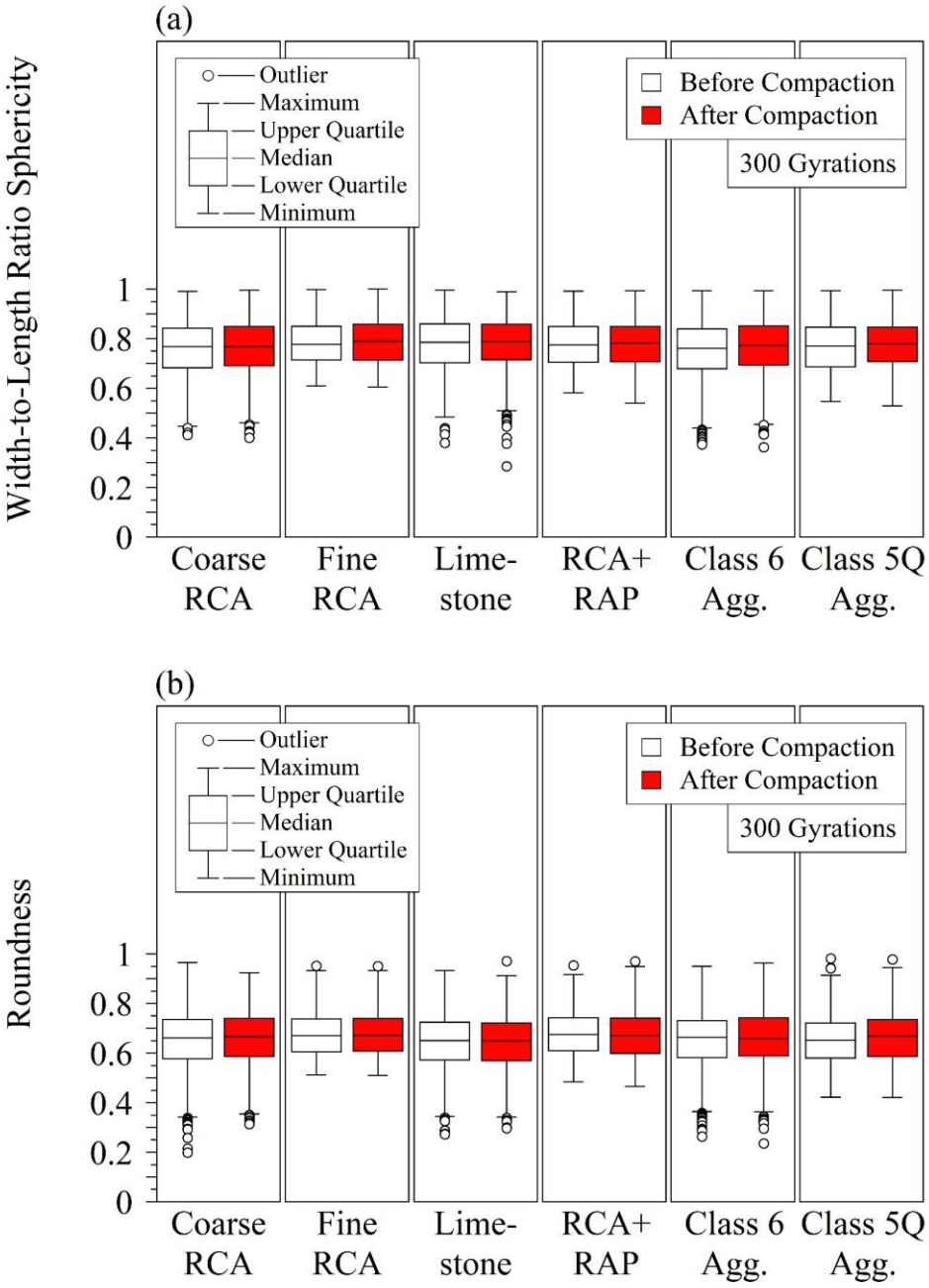

Figure 6.18. Abrasion on the particle shape after 300 gyrations in terms of (a) width-to-length ratio sphericity and (b) roundness

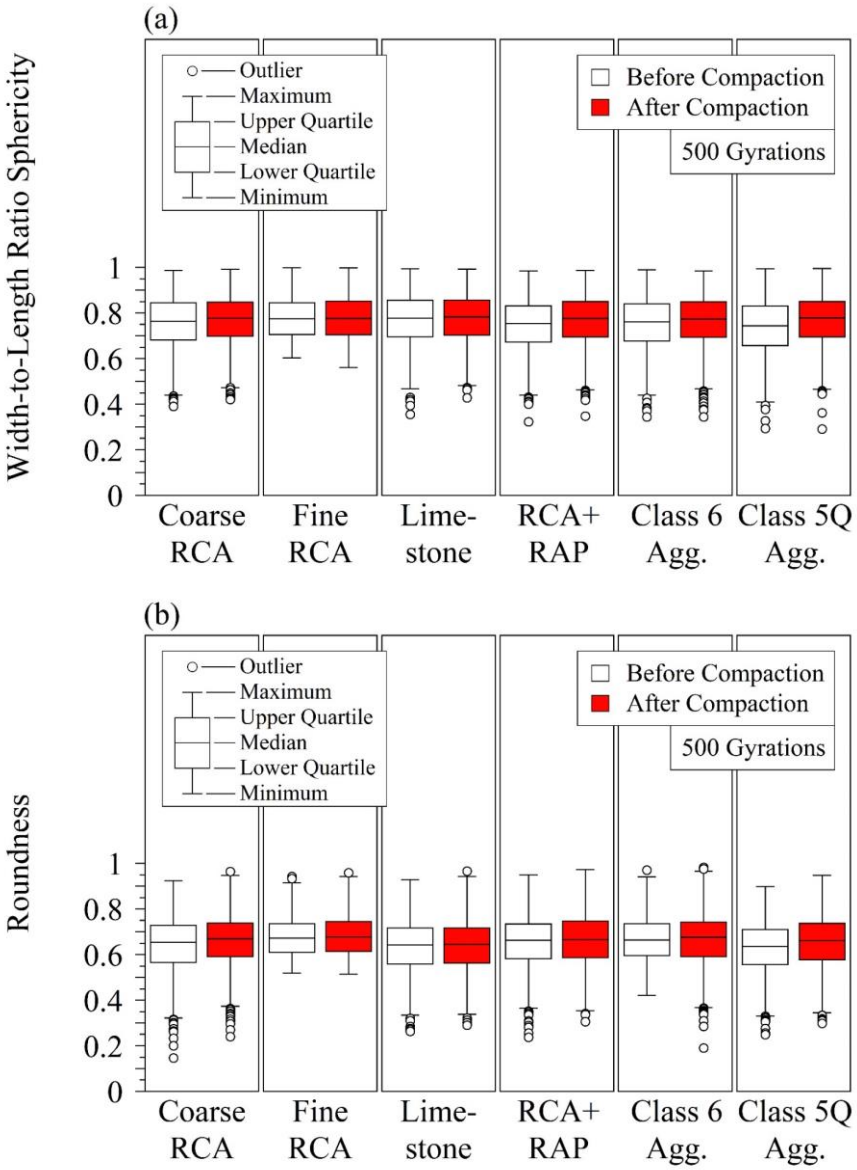

Figure 6.19. Abrasion on the particle shape after 500 gyrations in terms of (a) width-to-length ratio sphericity and (b) roundness

7. SUMMARY

- Each material contained less than 0.1% (by dry weight) deleterious materials and satisfied the quality requirements determined by the MnDOT. These deleterious materials included plant roots, leaves, wood chips, plastic, and fabric. No reinforcing steel was observed in the materials.

- Each material contained RAP particles to some extent. However, those RAP particles were considered to be the part of the materials, and therefore, were not removed.

- Coarse RCA, Fine RCA, and RCA+RAP exhibited lower G_s than Limestone because of their residual mortar content and porous structure. Low-density asphalt binder and trapped air

between the asphalt and aggregate particles were also the reason for the lower G_s of RCA+RAP. Fine RCA exhibited lower G_s than Coarse RCA. It was concluded that Class 6 Aggregate and Class 5Q Aggregate contained considerable amounts of recycled aggregates (RCA and RAP for Class 6 Aggregate and only RCA for Class 5Q Aggregate) because their G_s values were considerably lower than Limestone.

- Coarse RCA, Fine RCA, and RCA+RAP exhibited higher absorption than Limestone due to their residual mortar content and porous structure. Fine RCA exhibited higher absorption than Coarse RCA. RCA+RAP exhibited lower absorption than Coarse RCA and Fine RCA due to the presence of hydrophobic RAP material. Class 6 Aggregate and Class 5Q Aggregate also exhibited higher absorption than that of Limestone. These results were another sign of the presence of the recycled aggregates in Class 6 Aggregate and Class 5Q Aggregate.

- Coarse RCA, Fine RCA, and RCA+RAP exhibited lower MDD and higher OMC than Limestone because of the presence of residual mortar and cementation of unhydrated cement particles in the RCA matrix. Fine RCA exhibited lower MDD and higher OMC than those of Coarse RCA and RCA+RAP. Class 6 Aggregate and Class 5Q Aggregate exhibited lower MDD and higher OMC than Limestone due to the presence of the recycled aggregates in their matrices.

- The ignition method yielded higher asphalt binder contents compared to the quantitative extraction method and this was attributed to burned mineral fines and loss of fines in the ventilation system during ignition.

- For both the ignition and the quantitative extraction methods, the asphalt binder contents of RCA+RAP and Class 6 Aggregate were higher than those of other materials. Relatively lower asphalt binder contents were observed with Coarse RCA, Limestone, and Class 5Q Aggregate. According to the ignition method, asphalt binder content of Fine RCA was close to those of RCA+RAP and Class 6 Aggregate. However, according to the quantitative extraction method, Fine RCA contained considerably lower asphalt binder compared to RCA+RAP and Class 6 Aggregate. This result was attributed to the G_s of Fine RCA. It was concluded that the rate of loss of fines by the ventilation for Fine RCA was higher due to its relatively lower G_s.

- The freeze-thaw method developed by Abbas et al. (2008) to determine the residual mortar contents of the materials was successful. The residual mortar contents of Class 5Q Aggregate and Coarse RCA were higher than those of other materials. Fine RCA exhibited higher residual mortar content than Class 6 Aggregate and RCA+RAP. Limestone did not contain a considerable amount of residual mortar.

- Coarse RCA, Fine RCA, Limestone, and Class 5Q Aggregate exhibited 0° apparent contact angle and WDPT less than 5 seconds. Therefore, these materials were classified as wettable or hydrophilic. Apparent contact angles of RCA+RAP and Class 6 Aggregate were 83° and 86°, respectively. In addition, the water drops did not infiltrate through RCA+RAP and Class 6 Aggregate even after 3600 seconds from the placement of the water drops. As a result, these materials were classified as water repellent or hydrophobic.

- In the constant head permeability tests, the specimens could not be compacted sufficiently by the light hammering in the membrane because the degree of compaction (DOC) values were lower than 100%. Fine RCA yielded the highest permeability values with a narrower range. Sand Subgrade, Coarse RCA, and RCA+RAP exhibited relatively lower K_{sat} values with wider ranges. Class 6 Aggregate and Class 5Q Aggregate also exhibited similar K_{sat} values (Class 6 Aggregate exhibited a narrower range). Limestone exhibited similar K_{sat} values compared to Class 6 Aggregate and Class 5Q Aggregate; however, the minimum K_{sat} value of Limestone was much lower than those of Class 6 Aggregate and Class 5Q Aggregate.

- In the falling head permeability tests, the compaction process was more efficient by compacting the specimens in the rigid compaction mold. Overall, the K_{sat} values obtained by the falling head permeability were in narrower ranges compared to those obtained by the constant head permeability, in which the specimens were compacted by light hammering in the membrane. According to the falling head permeability tests, Clay Loam exhibited the lowest K_{sat} values as expected. Coarse RCA, Fine RCA, and RCA+RAP exhibited similar K_{sat} values (K_{sat} values of Fine RCA were in a narrower range) and they were higher than those of Limestone.

- Lowering the DOC yielded higher K_{sat} values for all materials. Less compaction, yielding lower DOC values, was obtained by applying lower compaction energies and these materials exhibited a more porous structure which allowed water to pass through faster.

- The hanging column tests for evaluating the soil-water characteristic curves (SWCCs) of materials were generally successful on Sand Subgrade and Class 6 Aggregate. However, results obtained for Class 5Q Aggregate and Fine RCA were not reliable. This result was attributed to the cementation of the unhydrated cement in the RCA matrix. Cementation occurred during the long testing period and it caused difficulty for the water outflow and created a risk regarding ceramic pore-clogging. Another reason could be related to the fines content of the Class 5Q and Fine RCA specimens. Hanging column test is more suitable for coarse materials.

- The pressure plate and activity meter tests were successful on Clay Loam, Coarse RCA, Fine RCA, Limestone, and RCA+RAP. In addition, the pressure plate and activity meter tests yielded narrower ranges for the specimens from the same materials compared to the hanging column tests. It was concluded that pressure plate and activity meter tests were more suitable for materials that contained RCA or that contained higher fines contents.

- It was observed that the higher the DOC of the specimens, the lower the initial volumetric water content of the specimens at the fully saturated condition. This was due to the denser structure of the specimens. The denser structure of the specimens yielded lower void ratio values, which in turn lowered the initial volumetric water content at fully saturated conditions.

- Sand and fines contents of the materials could not be determined by stereophotography because only the particles retained on No. 4 sieve (4.75 mm) could be used for this technique. For LSSB material, the entire gradation curve could be obtained because a very small portion of the particles was finer than No. 4 sieve. However, for Coarse RCA, Fine RCA, Limestone, RCA+RAP, Class 6 Aggregate, and Class 5Q Aggregate, significant portions of the gradation

curves of these materials could not be determined by stereophotography because those materials contained significant amounts of particles passing No. 4 sieve. Overall, for all materials, the result of stereophotography remarkably matched with the result of sieve analysis for the particles retained on No. 4 sieve.

- Base layer aggregates exhibited similar width-to-length ratio sphericity (S_{WL}) distributions. However, LSSB particles were less spherical than base layer aggregates overall. While base layer aggregates yielded similar roundness distributions, the roundness distribution of LSSB particles was considerably different from those of base layer aggregates. LSSB particles were relatively less rounded (more angular) than base layer aggregates.

- The dry unit weight of each specimen increased during the gyratory compaction. Applying 100 and 300 gyrations yielded uninterrupted curves showing the increase in the dry unit weight of the specimens. On the other hand, applying 500 gyrations yielded interrupted curves because the test stopped automatically and was restarted manually at the end of the first set of the 250 gyrations.

- The highest breakage potential (B_p) was observed with Class 5Q Aggregate followed by Coarse RCA because of their coarser gradations. The B_p values of Fine RCA, RCA+RAP, and Class 6 Aggregate were not very different from each other.

- The highest total breakage (B_t) was observed with Class 5Q Aggregate followed by Coarse RCA for each number of gyrations. This result was compatible with the B_p values of these two aggregates, which were higher than the other materials. While Fine RCA's B_p value was lower than and equal to those of Limestone and RCA+RAP, respectively, it exhibited higher B_t than those materials for each number of gyrations. This result was attributed to the higher residual mortar content of Fine RCA. B_r values of the materials exhibited a similar trend as observed for the B_t values.

- Overall, it was concluded that an increase in the gyration number yielded higher changes in the particle shapes. In addition, the materials became slightly more spherical and rounded due to abrasion caused by gyratory compaction.

8. DISCUSSIONS

- The use of Coarse RCA and Class 5Q Aggregate in aggregate base layers may cause several problems. Test results showed that Coarse RCA and Class 5Q Aggregate exhibited higher breakage potential (B_p) and higher total breakage (B_t). Higher breakage of particles may decrease the permeability of aggregate base layers which can then affect the long-term pavement performance negatively.

- Breakage of Coarse RCA and Class 5Q Aggregate may also cause a release of unhydrated cement content which presents in the RCA particle's matrix. This may increase the potential for tufa formation. Drainage properties of aggregate base layers constructed with RCA can be reduced as a result of the tufa formation.

- All the materials which contain RCA (Coarse RCA, Fine RCA, RCA+RAP, Class 6 Aggregate, and Class 5Q Aggregate) may attract more water due to higher absorption capacity and hydrophilicity. An increase in the water-holding capacity of aggregate base layers constructed with RCA materials may cause a decrease in the freeze-thaw (F-T) resistance.

- Light hammering in the membrane was not a suitable method to prepare the specimens for constant head permeability testing. Instead, compacting the materials in the compaction mold was more suitable to reach higher DOC values and to obtain more consistent K_{sat} readings.

- The hanging column test method was not suitable to determine the SWCC characteristics of RCA materials due to the cementation of the unhydrated cement in the RCA matrix. In addition, the hanging column test method did not work well for materials having relatively higher fines content. It was observed that the pressure plate and activity meter worked better for RCA materials and materials with higher fines content.

9. RECOMMENDATIONS

Based on Task 4 results, the following recommendations were made for practical applications:

- It can be concluded that any base layer aggregate with asphalt binder contents higher than 3% (per the ignition method) and 1.5% (per the quantitative extraction method) would exhibit hydrophobic properties. This would result in materials with higher freeze-thaw durability and better drainage properties.

- Degree of compaction (DOC) of coarse-grained RCA materials should be between 90% and 95% due to the higher breakage potential and total breakage of large size aggregates in their matrices.

- Base layer aggregates should be treated as RCA materials if their absorption contents and mortar contents are equal to or higher than 6% and 25%, respectively.

- Gradation characteristics of RCA materials collected from quarries should be determined after they are subjected to compactions tests to evaluate the effects of abrasion on the gradation.

- Laboratory test results showed that specs and guidelines should be updated based on gradation, absorption, residual mortar content, and abrasion. However, more detailed information regarding this will be provided in Task 7 (pavement design criteria) after completion of Task 5 (performance monitoring and reporting) and Task 6 (instrumentation).

10. REFERENCES

Abbas, A., Fathifazl, G., Isgor, O. B., Razaqpur, A. G., Fournier, B., & Foo, S. (2008). Proposed method for determining the residual mortar content of recycled concrete aggregates. *Journal of ASTM International*, *5*(1), 1-12.

ACPA (2009). *Recycling Concrete Pavements*. Engineering Bulletin 043P. American Concrete Paving Association, Skokie, IL.

ACPA (2010). *Why Recycle Concrete Pavements?* TS043.1P. American Concrete Paving Association, Skokie, IL. http://1204075.sites.myregisteredsite.com/downloads/TS/EB043P /TS04 3.1P.pdf.

Altuhafi, F., O'sullivan, C., & Cavarretta, I. (2012). Analysis of an image-based method to quantify the size and shape of sand particles. *Journal of Geotechnical and Geoenvironmental Engineering*, *139*(8), 1290-1307.

Bhasya, V., & Bharatkumar, B. H. (2018). Mechanical and Durability Properties of Concrete Produced with Treated Recycled Concrete Aggregate. *ACI Materials Journal*, *115*(2).

Butler, L., West, J. S., & Tighe, S. L. (2011). Quantification of recycled concrete aggregate (RCA) properties for usage in bridges and pavements: An Ontario case study. In *Innovative Developments in Sustainable Pavements, Annual Conference of the Transportation Association of Canada* (pp. 1-17).

Cedergren, H. R. (1988). Why all important pavements should be well drained. *Transportation research record*, *1188*, 56-62.

Ceylan, H., Gopalakrishnan, K., Kim, S., & Steffes, R. F. (2013). "Evaluating Roadway Subsurface Drainage Practices," IHRB Project TR-643. Institute for Transportation, Iowa State University, Ames, IA.

Chen, J., & Brown, B. (2012). Leaching characteristics of recycled aggregate used as road base. *University of Wisconsin system solid waste research program Student Project Report*.

Cho, G. C., Dodds, J., & Santamarina, J. C. (2006). Particle shape effects on packing density, stiffness, and strength: natural and crushed sands. *Journal of geotechnical and geoenvironmental engineering*, *132*(5), 591-602.

Cosentino, P. J., Kalajian, E. H., Shieh, C. S., Mathurin, W. J. K., Gomez, F. A., Cleary, E. D., & Treeratrakoon, A. (2003). *Developing specifications for using recycled asphalt pavement as base, subbase or general fill materials, phase II* (No. FL/DOT/RMC/06650-7754).

De Juan, M. S., & Gutiérrez, P. A. (2009). Study on the influence of attached mortar content on the properties of recycled concrete aggregate. *Construction and Building Materials*, *23*(2), 872-877.

Ebrahimi-Birang, N., Fredlund, D. G., & Samarasekera, L. (2007). Hysteresis of the soil-water characteristic curve in the high suction range. In *Proc. OttawaGeo Conf* (pp. 1061-1068).

Edil, T. (2011). Specifications and recommendations for recycled materials used as unbound base course, Recycled Materials Resource Center, Univ. of Wisconsin-Madison, Madison, WI.

Edil, T. B., Tinjum, J. M., & Benson, C. H. (2012). Recycled Unbound Materials. Report No. 2012-35. Minnesota Department of Transportation. St. Paul, MN.

Fletcher, T., Chandan, C., Masad, E., & Sivakumar, K. (2003). Aggregate imaging system for characterizing the shape of fine and coarse aggregates. *Transportation Research Record*, *1832*(1), 67-77.

Fredlund, D. G., & Rahardjo, H. (1993). *Soil mechanics for unsaturated soils*. John Wiley & Sons.

Ghalib, A. M., & Hryciw, R. D. (1999). Soil particle size distribution by mosaic imaging and watershed analysis. *Journal of Computing in Civil Engineering*, *13*(2), 80-87.

Gonzalez, G. P., & Moo-Young, H. K. (2004). Transportation applications of recycled concrete aggregate. *FHWA State of the Practice National Review*.

Greenbook (2009). Construction Materials, Section 200-Rock Materials. In *Greenbook* Standard Specifications for Public Works Construction.

Gupta, S., Singh, A., & Ranaivoson, A. (2004). Moisture Retention Characteristics of Base and Sub-base Materials. Report No. MN/RC-2005-06. Minnesota Department of Transportation, St. Paul, MN.

Hardin, B. O. (1985). Crushing of soil particles. *Journal of geotechnical engineering*, *111*(10), 1177-1192.

Harman, T., Bukowski, J. R., Moutier, F., Huber, G., & McGennis, R. (2002). History and future challenges of gyratory compaction: 1939 to 2001. *Transportation research record*, *1789*(1), 200-207.

Hillel, D. (1980). *Fundamental of soil physics*. Academic Press, Inc., San Diego, CA.

Hiller, J. E., Deshpande, Y. S., Qin, Y., Shorkey, C. J., & Peterson, K. (2011). *Efficient use of recycled concrete in transportation infrastructure* (No. RC-1544). Michigan Technological University.

Hoppe, E. J., Lane, D. S., Fitch, G. M., & Shetty, S. (2015). Feasibility of reclaimed asphalt pavement (RAP) use as road base and subbase material (No. VCTIR 15-R6).

Hryciw, R. D., & Ohm, H.-S. (2012). "Feasibility of digital imaging to characterize earth materials." *Research Report No. RC1557*, Michigan Department of Transportation, Lansing, MI.

Hryciw, R. D., Zheng, J., & Shetler, K. (2016). Particle roundness and sphericity from images of assemblies by chart estimates and computer methods. *Journal of Geotechnical and Geoenvironmental Engineering*, *142*(9), 04016038.

Hussain, M., & Dash, S. K. (2010). "Influence of lime on plasticity behaviour of soils." *Proc., Indian Geotechnical Conference,* Guntur, India, 537–540.

Jayakody, S., Gallage, C., & Kumar, A. (2012). Assessment of recycled concrete aggregate for road base and sub-base. In *Proceedings of the Second International Conference on Geotechnique, Construction Materials and Environment* (pp. 575-579). The GEOMATE International Society.

Kazmee, H., Mishra, D., & Tutumluer, E. (2015). Sustainable alternatives in low volume road base course applications evaluated through accelerated pavement testing. In *IFCEE 2015* (pp. 409-418).

Kazmee, H., Tutumluer, E., & Beshears, S. (2016). Pavement working platforms constructed with large-size unconventional aggregates. *Transportation Research Record: Journal of the Transportation Research Board*, (2578), 1-11.

Kim, W., Labuz, J., & Dai, S. (2007). Resilient modulus of base course containing recycled asphalt pavement. *Transportation Research Record: Journal of the Transportation Research Board*, (2005), 27-35.

Kim, Y., Suh, H. S., & Yun, T. S. (2019). Reliability and applicability of the Krumbein-Sloss chart for estimating geomechanical properties in sands. *Engineering geology*, *248*, 117-123.

Krumbein, W. C., & Sloss, L. L. (1951). *Stratigraphy and sedimentation* (Vol. 71, No. 5, p. 401). LWW.

Kumara, G. H. A., Hayano, K., & Ogiwara, K. (2012). Image analysis techniques on evaluation of particle size distribution of gravel. *Int. J. Geomate*, *3*(1), 290-297.

Lee, J., Edil, T., Tinjum, J., & Benson, C. (2010). Quantitative assessment of environmental and economic benefits of recycled materials in highway construction. *Transportation Research Record: Journal of the Transportation Research Board*, (2158), 138-142.

Li, C., Ashlock, J. C., White, D. J., Jahren, C. T., & Cetin, B. (2017). Gyratory abrasion with 2D image analysis test method for evaluation of mechanical degradation and changes in morphology and shear strength of compacted granular materials. *Construction and Building Materials*, *152*, 547-557.

Li, C., White, D. J., & Vennapusa, P. (2015). Moisture-density-strength-energy relationships for gyratory compacted geomaterials. *Geotechnical Testing Journal*, *38*(4), 461-473.

Likos, W. J., & Lu, N. (2003). Automated humidity system for measuring total suction characteristics of clay. *Geotechnical Testing Journal*, *26*(2), 179-190.

Likos, W. J., Lu, N., & Godt, J. W. (2013). Hysteresis and uncertainty in soil water-retention curve parameters. *Journal of Geotechnical and Geoenvironmental Engineering*, *140*(4), 04013050.

LRRB (2016). Recycled Materials in Unbound Aggregate Base Layers in Minnesota. Transportation Research Synthesis (TRS 1604). Local Road Research Board, Minnesota Department of Transportation.

MnDOT (2017). *MnROAD safer, smarter, sustainable pavements through innovative research*. MnDOT, St. Paul, MN.

MnDOT (2018). Standard Specifications for Construction (2018 Edition). Minnesota Department of Transportation, St. Paul, MN.

NCHRP (2004). "Guide for Mechanistic-Empirical Design of pavement structures: part 2 – Design Inputs." *ARA, Inc.*, ERES Consultants Division, Champaign, IL.

Nokkaew, K., Tinjum, J. M., & Benson, C. H. (2012). Hydraulic properties of recycled asphalt pavement and recycled concrete aggregate. In *GeoCongress 2012: State of the Art and Practice in Geotechnical Engineering* (pp. 1476-1485).

Ober, J.A., 2018. *Mineral Commodity Summaries 2018*. U.S. Department of the Interior, U.S. Geological Survey, Reston, VA.

Ohm, H. S., & Hryciw, R. D. (2013). Translucent segregation table test for sand and gravel particle size distribution. *Geotechnical Testing Journal*, *36*(4), 592-605.

Okafor, F. O. (2010). Performance of recycled asphalt pavement as coarse aggregate in concrete. *Leonardo Electronic Journal of Practices and Technologies*, *17*(9), 47-58.

Rahardjo, H., Vilayvong, K., & Leong, E. C. (2010). Water characteristic curves of recycled materials. *Geotechnical Testing Journal*, *34*(1), 89-96.

Schuettpelz, C. C., Fratta, D., & Edil, T. B. (2010). Mechanistic corrections for determining the resilient modulus of base course materials based on elastic wave measurements. *Journal of geotechnical and geoenvironmental engineering*, *136*(8), 1086-1094.

Snyder, M., Smith, K. D., Vandenbossche, J. M., & Wade, M. J. (1994). Physical and Mechanical Properties of Recycled PCC Aggregate Concrete. *Interim Report–Task A, DTFH61-93C-00133, US Department of Transportation, Federal Highway Administration*.

Sposito, G. (1981). *The Thermodynamics of Soil Solutions*, Oxford University Press.

Tan, D., Hill, K., & Khazanovich L. (2014). Quantifying Moisture Effects in DCP and LWD Tests Using Unsaturated Mechanics. Report No. MN/RC 2014-13. Minnesota Department of Transportation.

Tanyu, B. F., Benson, C. H., Edil, T. B., & Kim, W. H. (2004). Equivalency of crushed rock and three industrial by-products used for working platforms during pavement construction. *Transportation Research Record*, *1874*(1), 59-69.

Thakur, J. K., & Han, J. (2015). Recent development of recycled asphalt pavement (RAP) bases treated for roadway applications. *Transportation Infrastructure Geotechnology*, *2*(2), 68-86.

Tutumluer, E. (2013). Practices for Unbound Aggregate Pavement Layers: A Synthesis of Highway Practice. *Transportation Research Board of the National Academies, Washington, DC, Rep. NCHRP Synthesis*, *445*.

Vallejo, L. E., Lobo-Guerrero, S., & Hammer, K. (2006). Degradation of a granular base under a flexible pavement: DEM simulation. *International Journal of geomechanics*, *6*(6), 435-439.

Van Genuchten, M. T. (1980). A closed-form equation for predicting the hydraulic conductivity of unsaturated soils. *Soil science society of America journal*, *44*(5), 892-898.

West, R. (2010). Reclaimed asphalt pavement management: best practices. *Auburn, AL: National Center for Asphalt Technology, NCAT Draft Report*.

Westover, T. M., Labuz, J. F., & Guzina, B. B. (2007). Resilient Modulus Development of Aggregate Base and Subbase Containing Recycled Bituminous and Concrete for 2002 Design Guide and Mn/Pave Pavement Design. Report No. MN/RC-2007-25. Minnesota Department of Transportation, St. Paul, MN.

White, D. J., & Vennapusa, P. (2014). Rapid in situ measurement of hydraulic conductivity for granular pavement foundations. In *Geo-Congress 2014: Geo-characterization and Modeling for Sustainability* (pp. 3005-3014).

Zeghal, M. (2009). The impact of grain crushing on road performance. *Geotechnical and Geological Engineering*, *27*(4), 549.

Zheng, J., & Hryciw, R. D. (2014). Soil particle size characterization by stereophotography. In *Geo-Congress 2014: Geo-characterization and Modeling for Sustainability* (pp. 64-73).

Zheng, J., & Hryciw, R. D. (2015). Traditional soil particle sphericity, roundness and surface roughness by computational geometry. *Géotechnique*, *65*(6), 494-506.

Zheng, J., & Hryciw, R. D. (2016). Segmentation of contacting soil particles in images by modified watershed analysis. *Computers and Geotechnics*, *73*, 142-152.

Zheng, J., & Hryciw, R. D. (2017). Soil particle size and shape distributions by stereophotography and image analysis. *Geotechnical Testing Journal*, *40*(2), 317-328.